AN ANALYSIS OF π^0 MESONS PRODUCED IN MINIMUM BIAS 515 GeV/c π^- NUCLEAR COLLISIONS

A Dissertation APPROVED FOR THE
DEPARTMENT OF PHYSICS AND ASTRONOMY

BY

Phillip Gutierrez

George Kalbfleisch

Ronald Kantowski

Patrick Skubic

Bruce Mason

William Kuriger

Acknowledgments

First, I would like to thank my wife EKaterina Leondidovna Dickaya for her love and support through these graduate school years. I will always remember how you cared for me, and helped me to recover from the burn injuries that I received in the middle of my graduate school career. I also, want thank her son Philip for being the nice young man that he is.

I would like to thank my parents Richard and Kathleen Kuehler for raising me, and letting me pursue my own interests. I would like to thank my sisters Grethchen, Thresa, Charlotte, and Sandra for the life we had growing up. I would also like to thank my mother and father-in-law Nina Bogdateva and Leonid Dickey for their kindness and friendship during my stay in Norman. I would like to thank my grandmother Eunice Kuehler for giving me the means to do my undergraduate education. Thanks to Charles and Norma Kuehler for making my years in Stephenville, while attending Tarleton, enjoyable.

I would like to thank some of my classmates at the University of Oklahoma for their friendship. In particular would like to thank Mark and Jolene Wood for their help and friendship while on the BCD test beam. I would also like to thank them for their help during my hospitalization in Illinois after my burn injuries. I also thank Moustafa Bahran whose smiling face in the Lab, and all the controversy surrounding the 17 KeV neutrino made life interesting; Mark Lambrecht whose friendship during the first test beam is appreciated; and Eric Smith who kept the lab interesting, and proof read part of this thesis. I would like to thank Chuck Hembree and Bruce Mason for all those toe jamming, arm blowing, finger busting climbing trips around Oklahoma, and far off places in New Mexico and Colorado. I will never forget all the exercise and adrenaline rushes of fear. I would like to thank Doug Miller, Jim Buell, Ken Eack, Bryan Elza, Scott McCartney, and Wayne Trails for their friendship. The skiing trip to Breckenridge, and climbing experiences were the best. I would also like to thank Scott McCartney for friendship, and

observations, and proof reading the thesis.

The secretaries at OU have done an outstanding job at making OU an efficient place to work and study. Grettie Stimson was a good graduate secretary as well as a good friend and skiing partner. Linda Christie, Danette Miller, and Johnette Ellis were always very helpful, and friendly.

The people I grew up around had a large impact on my life that I will never forget, and will continue to enjoy. Edwin, Norman, and Pat Teltschik, I will always truly value your friendship. I would like to thank Michael Dunlap for his friendship over the years. My first exposure to how to solve problems was due to Romeo V. Gonzalez, my scouting leader. Being an electrical engineer, he helped me obtain my amateur license, my first exposure to electrical science, which paved the way for me to go into science; and, all the scouting camping trips that are a life remembered experience. Jimmy McCoy at Tarleton State University who first interested me in pursuing physics as a career. Both he and Paul Lawrence prepared me well for graduate school, and made Tarleton a good place to study. I also thank Dr. Jerry Darsey for giving me the opportunity to work with him in is investigation of polymer structure. During my schooling, I had many good instructors who are too numerous to mention, but their teaching has lead to a metamorphosis of my personality. The people from my undergraduate days that I will never forget: Greg Follis, Jim Gary, Frank Aarron, Scott Tumdigui, and Brian Watson. I would also like to thank my instructors at Bee County College for the beginnings of my college career.

Professionally, I would like to thank Phil Gutierrez for his guidance on this thesis, and on the BCD test beam. I would also like to thank George Randolf Kalbfleisch, for getting me into the OUHEP group. His level of scientific ability, mental quickness on his feet, and ability to analyze data sets a standard that I can only hope to approach. Also, I would like to acknowledge the hard work he has done to fund our research and support the student. I also would like

to thank George Ginther. His work ethic and prowess at analyzing data is a model for the experimental physicist which set another standard I can only hope to approach. I also want to thank him for making the beam and interaction trigger skims which were crucial for this work, and for his advise on signal analysis and normalization. Thanks to Marek Zelenski for his experience in data analysis. I would like to thank Paul Slattery for letting me join his experiment in my limited capacity. In graduate school Kim Milton taught classes that demonstrated clearly the mathematical and physical mind that a physicist must possess. He clearly demonstrated how measurement and theory are connected. Dave Kaplan, Ron Kantowski, Caren Marzban and Pat Skubic also provided intellectual stimulus ,and made the atmosphere at OUHEP a pleasant one. Thanks Caren for teaching me a little bit about neural nets, and letting me play around with those C++ codes.

Now I would to thank all the students(in no particular order) who worked very hard to make E706 a success: Lenney Apanasevich for his Monte Carlo work, and musical taste that kept culture alive at E706; Rob Roser for his Monte Carlo work; Nikos Varelas and Micheal Begel for their work on the energy scale; Lucy de Barbaro for her work on the ω, and for her smiling face, and the social awareness standards she set for us all; John Bacigallupi, for his work on the alignment and those long bike rides down the Illinois prairie paths; Steve Blusk, Paoti Chang, Jim Dunlea, and Woohyun Chung for their work on the tracking system; Lee Sorrell for his trigger work which resulted in an excellent trigger document, and for taking the initiative to organize E706 lunches and picnics; David Striley for his work on the Cherenkov detector, and his sense of humor; Vishnu Zutshi for his work on Monte Carlo corrections; Andre Maul for his work on the tracking system. Wieshek Dlugosz for his help with the cross-section code; George Osbourne for his work on FREDPED, and triggers; David Brown for interesting discussions; and Vijay Kapoor and Dane Skow for help with MCE706. I would like to acknowledge

Dan Ruggeiro for all his hard work on the processing farms, for his making E706 an environmentally aware place. His level of exercise and fitness is a level I can only hope to approach. And again I would like to thank George Ginther for his organization of E706.

Finally, I would like to thank Andy Feldt at OU, Chris Lirakis, and Jim Dunlea at E706 for their assistance with all the software involved in this analysis, and for teaching me few things about computers systems and software.

Contents

List of Figures

List of Tables

Chapter 1

INTRODUCTION

Experiment E706 is a second generation fixed target experiment designed to measure the direct photon cross section at high p_t (that is transverse momentum to the relativistically boosted p_z of the incident beam particles), and extract the gluon structure function of hadrons and mesons. The advantage of this process is that photons(γ) from the primary collision do not undergo the fragmentation that quarks undergo to produce mesons and baryons from the 2-2 QCD hard scatter, thus direct photons give the cleanest momentum probe of gluons in the hard scatter [1]. In this thesis the π^0 production differential cross section, in terms of p_t, from the collisions recorded in E706 is measured. This measurement was made at the low p_t ($.6\ GeV/c\ <\ p_t\ <\ 2.2\ GeV/c$) end of E706's capabilities. What is meant by the π^0 differential cross section is the probability of observing π^0s between p_t and $p_t + dp_t$ from a particle collision. In this thesis the differential cross section, as a function of p_t, for production of the π^0 from π^- mesons incident on the nuclear targets of copper(Cu), and beryllium (Be) targets is presented. This measurement will be useful for the extraction of the pion distribution function and the fragmentation function of partons into $\pi^0 s$.

During the 1990 experimental run a 515 GeV/c π^- beam was incident upon Cu and Be targets, and the E706 spectrometer recorded 12 $\frac{events}{pb}$ of data. In 1991 the beam was 800 GeV/c protons incident on H, Be, Cu targets. One reason for using different targets is that when one compares the cross sections of π^0's, π^-'s,

etc. between the different nuclear targets, one can cleanly deduce the nuclear, $\sigma = \sigma_0 A^\alpha$, dependence of the cross section. This is because the nuclear α dependence can be calculated as a ratio of two cross sections, thus canceling out systematics in the measurement of both cross sections.

Photons are produced copiously in hadron collisions from many sources such as $\pi^0 \rightarrow \gamma + \gamma$, $\eta^0 \rightarrow \gamma + \gamma$, $\omega \rightarrow \gamma + \gamma + \gamma$, and direct photons [1]. The direct photon to pion ratio ,$\frac{\gamma}{\pi}$, starts off at 1% at low p_t and should exceed 10% at large p_t. To have an enhancement of QCD 2-2 hard scattering events that produce direct photons, the experiment had 6 different trigger levels designed to select out QCD hard scatters that produce high p_t electromagnetic objects. There were also two minimum bias triggers and a di-muon trigger for a total of 9 trigger types. The two minimum bias triggers were used in this analysis since the π^0 cross section falls steeply in increasing p_t and the minimum bias triggers had no minimum p_t requirement. They were how ever scaled back or pre-scaled. That is that most of these triggers were rejected in favor of the higher p_t triggers, and thus this makes for a smaller sample of the data.

The experiment used a highly segmented electromagnetic liquid argon calorimeter (EMLAC) to identify individual photons, and reconstruct their positions and energies. Thus, π^0's, η's (which decay into two photons, γ s), and other mesons ($\omega \rightarrow 3\gamma$) cross sections maybe measured, and subtracted as direct photon background. The position resolution of the EMLAC allowed for the fast online determination of the p_t of electromagnetic events so that discriminating trigger logic could be designed.

Previous measurements of π^0 production have covered a variety of center of mass energies, and incident beam particles [2]. E706 provides the highest center of mass energy and highest p_t range data for pion beams to date. Also, since E706 used a variety of targets it can determine the nuclear A dependence of the cross sections of direct photons, π^0's, and other mesons over a wide range of p_t

1.1 Partons, QCD, Direct Photons, and π^0s

In this section I describe the physics that E706 was designed to measure. First, the parton model with which it is believed explains the fundamental constituents that make up nuclear matter will need to be introduced. Second, QCD (Quantum Chromodynamics) is the theory that is believed to describe the interactions between the fundamental constituents of matter will be discussed. Third, direct photon production, E706's primary goal, is one of simplest and cleanest QCD interactions (because it is free from a process called fragmentation to be defined latter). Direct Photon measurements can the used to extract the momentum distribution(structure function) of hadrons such as the proton. Then the more complicated QCD process of π^0 production is discussed, and it is this process that is directly relevant to the thesis. By measuring the cross-section of π^0 production, one can extract the parameterization of QCD that describes how quarks fragment into pions, the fragmentation function.

It was realized early on from experiment that protons and neutrons were not fundamental particles, but were made up of yet smaller constituents. These constituents were labeled partons by Feynman, Bjorken, and others [3]. In the seventies, deep inelastic scattering (DIS) experiments of electrons off of proton targets (liquid hydrogen) at SLAC [4] revealed this to be the case. This is analogous to Rutherford scattering when it was determined that the atom itself was composed of a hard scattering center surrounded by a cloud of electrons. Further analysis of this data revealed that the observed DIS scattering cross section could be explained by hard point-like partons, which were then to be concluded to be in bound states of the three quarks of the quark model that Murray Gell-Mann had proposed in 1964 to explain the zoo of mesons and baryons being discovered in the 50's and 60's [3]. These three quarks are called the valence quarks of the proton, and they are two up quarks and a down quark (neutrons are two downs and a up). The table

below shows the quarks with which the hadrons are constructed. The hadrons are broken into two groups: the baryons which are 3 quark combinations (protons, neutrons, Δs, etc.), and mesons which are quark anti-quark combinations (π^0s, ηs etc.). Quarks also have their anti-matter partners which have the same mass, but opposite charge as its matter partner. These are denoted with an over bar over the quark symbol. Example: the anti-matter u quark is $\overline{u}$. Up and down quarks make up ordinary matter, such as protons ($p = |uud>$), neutrons ($n = |ddu>$). The pions are represented as: $\pi^- = |\overline{u}d>$, $\pi^+ = |u\overline{d}>$, and the π^0 which can be written as a linear combination of the u and d quark as $\pi^0 = \frac{1}{\sqrt{2}}|u\overline{u}> + \frac{1}{\sqrt{2}}|d\overline{d}>$. What this means physically is the following: If one could imagine a beam of π^0s streaming by and one were to randomly pick out π^0s, half would be $u\overline{u}$ combinations and the other half $d\overline{d}$ combinations.

Although the results of DIS experiments revealed hard scattering constituents in the proton, these constituents only account for 50% [[3] pp 275-276] of the momentum of the proton. So then, it is conjectured that rest of the partons that are carrying the other 50% of the momentum are the 8 bi-colored gluons of the strong force that holds the quarks together in their bound state to form the hadrons. The gluon is a massless gauge boson that mediates the strong force between quarks. This is analogous to electrodynamics where the photon mediates the electric force which holds charged particles together. Color is the analog of electric charge,

Quark Flavor	Electric Charge (e)	Mass Estimate (GeV/c^2)
d (down)	-1/3	0.0099±0.0011
u (up)	+2/3	0.0056±0.0011
s (strange)	-1/3	0.199±0.033
c (charm)	+2/3	1.35±0.05
b (bottom)	-1/3	~ 5
t (top)	+2/3	174±10

Table 1.1: Physical properties of quarks. See David Griffiths, Introduction to Elementary Particles.

which is mediated by the photon, but more complicated in the sense that there 3 colors where as there is only one electric charge. The three colors are labeled as red, blue, and green, and these also have anti-color partners. Color is a necessary quantity in the quark model to save Fermi statistics in the hadrons (that is no two identical particles in a bound state can have the same quantum numbers). In the case of the $\Delta^{++}(uuu)$, if the three u quarks were identical then Fermi statistics would be violated. Assigning a new quantum number of color remedies this. The current theory for the strong force that holds quarks together, which is mediated by the 8 bi-colored gluons, is Quantum Chromodynamics or QCD. The gluons are bi-colored in the fact that when there is an interaction between two quarks, the gluon can change the color of the quarks by carrying away one unit of color and one unit of anti-color. For example, a red u quark can change into a blue u quark by radiating a gluon with $r\bar{b}$ bi-color. Writing out all possibilities of color/anti-color combinations leads to 9 gluon types, but the 9^{th} is white (i.e. colorless) so it is omitted from the group. The fact that gluons can be of different bi-color combinations means that they can couple (interact) to each other (unlike the photon in electrodynamics). QCD is not well understood. Quarks have never been seen free, and DIS only gives indirect proof of their existence in the fact that the results can be explained in the context of the quark model.

In the bound state of the proton, the quarks all carry some momentum fraction of the proton, as do the gluons which are radiated and adsorbed by the quarks. This momentum fraction is denoted as x, which is called Bjorken x, and its range is $0 \leq x \leq 1$.. There is also a quark sea at low x which contributes to the structure of the proton. The quark sea is composed of low momentum quark/anti-quark pairs such as $u\overline{u}, s\overline{s}$, etc. These low x quark pairs are the result of gluons that radiate into a virtual $q\overline{q}$ pair which hence annihilate back into gluons to be absorbed by the valence uud quarks. In QCD the structure of the hadron is described by parton distribution functions and structure functions. A parton distribution

function, $G_i(x)$, describes the probability of finding the i^{th} parton (be it quark or gluon) with momentum fraction x and $x + dx$ within the hadron. The parton distributions must be determined from experiment. Since the dynamics of the strong force interaction are not understood, the distribution cannot be calculated from theory in analogy to the hydrogen atom problem in non-relativistic quantum mechanics where wave functions (hence probability amplitudes) are calculable.

Deep inelastic scattering experiments of both electron and neutrino beams are able to measure the distribution functions (or structure functions) of the quarks, but the gluon structure function is a higher order effect (since electrons which interact only through electro-weak forces do not directly couple with gluons) in these experiments; therefore, the gluon structure functions are not as easily or as accurately determined as by direct photon measurements. Direct photons are the result of the primary collision of two partons, and not the result of decays by other exotic hadrons produced in the collision such as π^0s and ηs. Direct photons are produced by the QCD process shown in figure 1.1, thus one can measure the gluon structure function in a more direct fashion. The Compton diagram is a quark-gluon interaction where the quark then radiates the momentum transferred by the gluon as a direct photon. The annihilation diagram is a quark, q, annihilating with an anti-matter quark, $\overline{q}$. One possibility for this process is the radiation of a photon and a gluon carrying away the momentum of the $q\overline{q}$ pair, thus by conservation of momentum the gluon momentum may be determined. There are higher order diagrams, but the amplitudes decrease with higher orders of α_s, α while the complexity of the calculation increases.

The reason that direct photons make a good probe to the gluon structure function is that the photon couples to the quark which couples to the gluon field in the hadron-hadron collision as shown in figure 1.1[1]. The next advantage to direct photons is that the QCD coupling constant α_s appears only once (in the lowest order cases) in the equation that describes the collision that results from

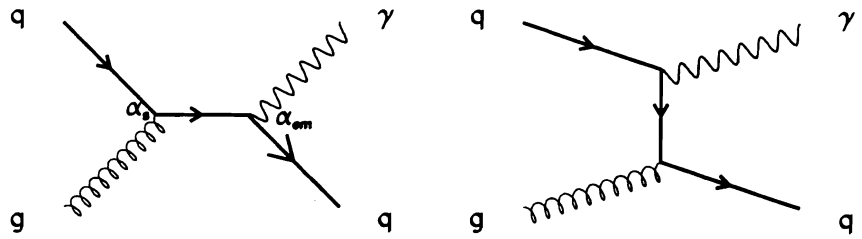

Compton Diagrams

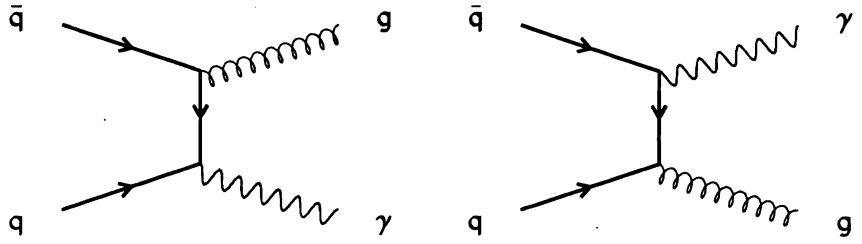

Annihilation Diagrams

Figure 1.1: The QCD level 2-2 hard scattering point diagram for direct photon production. The Compton diagram is quark-gluon scattering which is analogous to electron photon scattering. The annihilation diagram is where a quark and some anti-quark annihilate into a gluon and photon. Other possibilities include two gluons or two photons being emitted. Since the gluon is coupled to these in first order, the photon can be used to determine the momentum of the gluon.

applying Feynman QCD rules to the diagrams in 1.1. Finally, as the photon comes away from the collision it is colorless, so it will not undergo any complicated fragmentation and produce exotic hadrons; thus, its momentum comes directly from the interaction. If another quark or gluon were produced in the final state then it would undergo fragmentation and come out dressed up as a baryon or meson (in this thesis it is the π^0 meson that is of interest), and thus not be as clean for structure function analysis.

The coupling constant is a function that gives the strength of the force of the mediator (i.e. gluon or photon) to the particle that it couples to. In the non-quantum static electric case this is simply the charge e with the force between two particles being $\propto e^2$ (each particle has a vertex where the virtual photon is being exchanged between them. For a complete explanation of how Feynman rules are applied to scattering processes, that is where the coupling constants and propagators come into play, see reference [5]) For the strong force in QCD the coupling constant to first order is

$$\alpha_s(Q^2) = \frac{12\pi}{(33 - n_f)\ln(\frac{Q^2}{\Lambda^2})} \tag{1.1}$$

Q is the momentum transfer that occurs in the parton-parton collision.

What is meant by first order here is the fact that the perturbation series used to calculate the interaction between a quark pair is just taken out to the least power in α_s. As one goes to higher orders in α_s the function changes because the theory must be renormalized to take care of infinities that result from virtual particle loops (the higher order radiative corrections) that run over all momentum. These infinities are adsorbed in a renormalization of α_s, hence it "runs" in Q^2. Here only first order is discussed. For hard scattering (high Q^2) α_s is small allowing one to do QCD perturbatively; thus, one can calculate the scattering cross sections of fig. 1.1. Here Λ sets the scale for QCD, and it is related to the renormalization point of QCD. The scale factor Λ is not precisely known from theory and, neither is Q^2 since we cannot have a beam of free quarks and gluons; therefore, one does

not know *a priori* what the momentum of the partons involved in the collision were. We only know the four momenta ($P = (Energy, \vec{p}) = [E, p_x, p_y, p_z]$) of the incoming hadrons and the outgoing baryons, mesons, leptons, and photons; thus, Q^2 must be parameterized in terms of the four momenta of the incoming hadrons. This can be as simple as the four momenta of the hadrons divided by a factor of two or four; or, more complicated with the principle of minimum sensitivity (PMS) where the Q^2 of each parton is varied to match the data. The n_f is the number of generations of quarks which is three (up and down, strange and charm, and top and bottom).

Ideally, one would like to have a beam of free quarks incident on a target of protons, but this is not possible due to the fact that quarks are never free, and all naturally occurring objects are colorless, this is asymptotic freedom. That is if you had a quark pair (a meson say) and tried to rip it apart, the force between the quarks would increase until it broke by producing another quark/anti-quark pair out of the vacuum; thus, creating two quark pairs(two other mesons). Since a free quark beam is unavailable, the experimenter uses other hadrons (such as protons) and mesons(such as π^-) to provide the quarks and gluons as momentum probes of the nucleon. Of course, this complicates the issue because now the momentum of the quarks and gluons inside their bound state is ambiguous. This leads to the idea of structure functions where the constituents' momentum are given by probability distributions in terms of the momentum fractions of the constituents. It is these distribution functions for quarks and gluons that physics experiments are designed to measure, and in particular E706 goal is to determine the structure function of gluons within the nucleon via direct photons. Then once the distributions are determined, these distributions can be put into calculations and averaged over x to get physically measured averaged quantities such as scattering cross sections.

For an incident beam, A (π^-, p), on a nuclear target, B (p,n), we have the

following reaction for direct photon production. See figure 1.2

$$A + B \longrightarrow \gamma + X \tag{1.2}$$

X is simply the rest of the collision products that are ignored for the time being. The relativistically invariant cross section for this process is given by

$$E\frac{d^3\sigma}{dp^3} = \sum_{a,b} \int dx_a dx_b G_{a/A}(x_a, Q^2) G_{b/B}(x_b, Q^2) \frac{\hat{s}}{\pi} \frac{d\sigma}{d\hat{t}}(ab \to \gamma d)\delta(\hat{s} + \hat{t} + \hat{u}) \tag{1.3}$$

the $d\hat{t}$ represents the point cross section of the collision (figure 1.1 at the parton level). This is calculated by applying QCD Feynman rules to the graphs of figure 1.1. The Gs are the parton distribution functions. Since for each collision we do not know which partons were involved in the hard scatter, we sum over all possible partons in each hadron (in E706 , G_A is for the target nucleon, the G_b the π^-). Then, since these partons can carry any x over the range $0 \leq x \leq 1$; the G s must be averaged(assuming here the G s are normalized) by integrating over x.

Going back to the point cross section, $\frac{d\sigma}{d\hat{t}}$, The $\hat{t}$, $\hat{s}$, and $\hat{u}$ are the usual Mandlestam variables, and the $\hat{}$ refers to the fact that variables represent quantities evaluated at the parton level. The δ function conserves four momentum. Written in terms of the parton four momentum, these variables are defined to be:

$$\hat{s} = (p_a + p_b)^2 \tag{1.4}$$

$$\hat{t} = (p_a - p_\gamma)^2 \tag{1.5}$$

$$\hat{u} = (p_a - p_b)^2 \tag{1.6}$$

The point cross sections evaluated for the direct photon diagrams of figure 1.1 are:

$$\frac{d\sigma}{d\hat{t}}(qg \to q\gamma) = -\frac{\pi\alpha_{em}\alpha_s}{2\hat{s}^2} e_q^2 \frac{\hat{u}^2 + \hat{s}^2}{\hat{s}\hat{u}} \tag{1.7}$$

$$\frac{d\sigma}{d\hat{t}}(q\overline{q} \to q\gamma) = -\frac{8\pi\alpha_{em}\alpha_s}{9\hat{s}^2} e_q^2 \frac{\hat{u}^2 + \hat{t}^2}{\hat{t}\hat{u}} \tag{1.8}$$

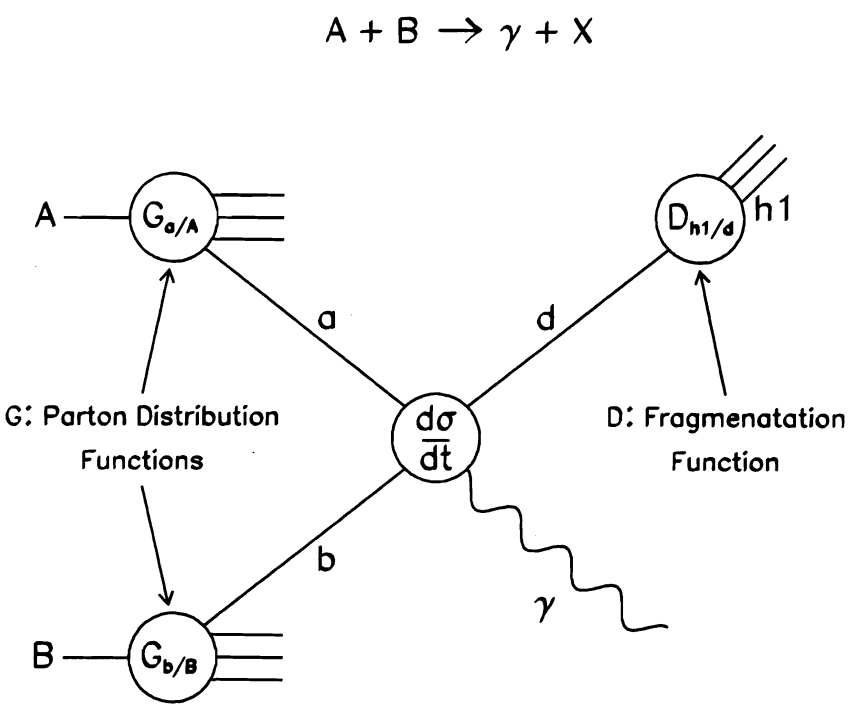

Figure 1.2: The hadron-hadron interaction diagram. The A and B are the interacting hadrons. In our case A would be a π^-, and the B would be nucleon of the target which could be a proton or a neutron. The a and b are the interacting partons, which the functions G gives the probability of their being found within their respective hadrons. The d is the out going parton (quark or gluon) which then undergoes fragmentation, described by D. The γ is the direct photon which does not undergo fragmentation, hence it is a clean probe of the momentum of the point cross section, $\frac{d\sigma}{dt}$, for direct photon production shown in figure 1.1

Now the Gs are the parton distribution functions which express the probability of finding a given parton a within hadron A within a momentum fraction of x and $x + dx$. The relation between parton distribution G_i, and the structure function F_i is $F_i = xG_i$. Since all partons are free to interact, one sums over all possible partons; and, since they can interact with any momentum fraction, then one must integrate and average over all momentum fractions. If parton a is a quark and parton b is a gluon, then the quark structure function being known from deep inelastic scattering, the gluon structure function can then be deduced from the direct photon cross section measurement. The above equation shows mathematically why direct photons are useful as gluon probes in the fact that there is no final state fragmentation function to complicate the analysis.

1.2 π^0 Production

The π^0 decays into a two γ pair with a branching ratio fraction of 98.8% [3]of the time, so π^0's are one of the largest sources of background to the direct photon signal [1]. Therefore, it is of greatest importance to be able to measure the π^0 cross section, and compare it to the direct photon cross section. By measuring the π^0 cross section one can extract the fragmentation functions that describe how partons hadronize into π^0s.

E706 had six different triggers. Most were designed to trigger only on interesting high p_t (hard scatters) events, and the cross section for these has been calculated elsewhere [13, 8]. In this thesis the minimum bias (interaction trigger) was used to look at the low p_t (.6-2.2 GeV) end of the π^0 cross section. The reaction for π^0 production when hadron A collides with hadron B can be written

$$A + B \rightarrow \pi^0 + X \tag{1.9}$$

Where X is the sum of everything else produced in the collision (direct photons, Kaons, etc.) The cross section for this process is a bit more complicated than for

direct photons, because pions have to be produced by a process called fragmentation. That is when a collision occurs and a quark or gluon is emitted at the parton level, then it must hadronize by pulling virtual parton pairs out of the vacuum to become the colorless, bound states of hadrons that we record in the lab. The cross section for π^0 can be expressed as

$$E\frac{d^3\sigma}{d^3p} = \sum_{a,b,c,d}\int dx_a dx_b dz_c G_{a/A}(x_a,Q^2)G_{b/B}(x_b,Q^2)D_{c/\pi^0}(z_c,Q^2) \times \frac{\hat{s}}{z_c^2\pi}\frac{d\sigma}{d\hat{t}}(ab\rightarrow cd)\delta(\hat{s}+\hat{t}+\hat{u}) \qquad (1.10)$$

Figure 1.3 schematically shows this process. The a, b are the colliding partons, and the c is the parton (which maybe a u, $\overline{u}$,d, or $\overline{d}$ quark) that will hadronize with another parton to form a π^0 coming out of the collision. The d is the other parton that hadronizes with other partons to form the awayside jets. The Function D is the fragmentation function that gives the probability of finding a π^0 with momentum fraction z and $z+dz$ from fragmentation of parton c. The fragmentation function cannot be determined theoretically, so it is measured from experiment. It can be determined from the π^0 cross section if the Gs are determined experimentally elsewhere from DIS for the quarks, and Direct photons for the gluon distribution functions.

In principle, if QCD were thoroughly understood, we would not need structure functions or fragmentation functions. The processes described above would all be directly calculable; but this is not the case today, and structure functions parameterize away our ignorance of QCD. Thus, the measurement of the π^0 cross section over a wide range of p_t is needed to calculate the fragmentation function and/or the structure functions.

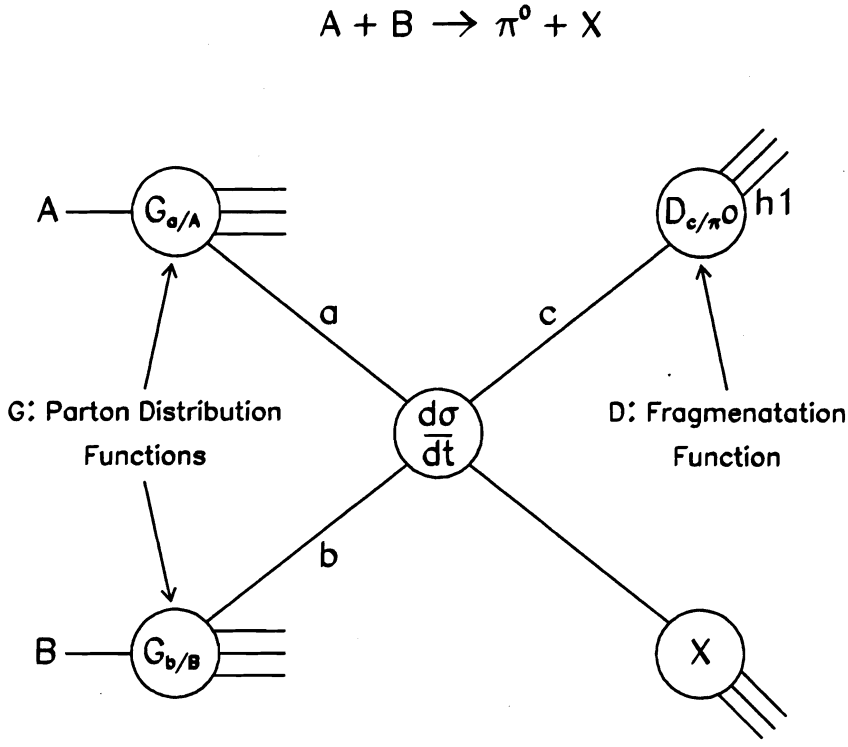

Figure 1.3: The hadron level diagram for π^0 production.

1.2.1 Nuclear Dependence

By measuring the π^0 cross section off of different nuclear targets the A dependence of the cross section, σ, can be deduced. A cross section parameterized in terms σ per nucleon (A = number of nucleons) can be written as

$$\sigma_{A/nucleon} = \sigma_0 A^{\alpha-1} \tag{1.11}$$

By taking the ratio of the cross sections calculated on two targets Cu and Be one gets

$$\alpha = 1 + \frac{ln(\frac{\sigma_{Cu}}{\sigma_{Be}})}{ln(\frac{A_{Cu}}{A_{Be}})} \tag{1.12}$$

Independent of σ_0. To the experimentalist, this can be measured by counting π^0's produced off of the Cu target, and Be target and taking a ratio with a few Z coordinate dependent corrections. This method is free from systematics in normalization and reconstruction efficiency since these cancel out in the ratio. The exact method will be discussed in the analysis chapter (chapter 4).

For π^0 with $p_t << 1.0\,GeV/c$ the A dependence is $\propto A^{\frac{2}{3}}$. This can be explained by nuclear shadowing, that is the scattering is taking place of a nuclear disk of cross sectional area $A^{\frac{2}{3}}$. For p_t $1.0\,GeV/c$ cross section scales as $A^{.9}$,and for values of $p_t > 2.0\,GeV/c$ α exceeds unity to ≈ 1.1. Ideally, α should be unity for high p_t, but, due to rescattering within the nucleus after a collision, α exceeds unity. E706 has measured the values for α from $.6\ GeV/c\ < p_t\ < 9\ GeV/c$ with high statistics so that nuclear effects in hadron-hadron collision can be carefully studied and modeled. At low p_t the A dependence is quite dramatic, as this thesis will demonstrate.

Chapter 2

E706 SPECTROMETER

E706 was a fixed target experiment conceived in the late seventies, and built during the eighties at Fermi National Accelerator Laboratory(Fermilab or FNAL) in Batavia, Illinois. In 1988, E706 saw its first beam. This analysis came from the physics run which occurred in 1990-1991.

Figure 2.1 shows a diagram of the spectrometer. Fermilab provides the beam that enters the spectrometer at the point along the line shown in figure 2.1. The beam direction defines positive z. The spectrometer consists of various kinds of particle identification, tracking, and energy measuring detector elements whose hits were recorded as data; and ultimately, in the end, reconstructed as four vectors (E, p_x, p_y, p_z) for particles produced from collisions within the targets in the spectrometer. These four vectors are then used in a physics analysis of the collisions offline (offline means after the data has been collected). In the sections that follow, I will describe the following components of the spectrometer: beamline, hadron shield, veto wall, silicon microstrip detectors (SSDs), targets, analysis magnet, downstream tracking system of proportional multiwire chambers and straws, and the energy measuring calorimeters. Finally, the data acquisition system used to extract data from the spectrometer's various detectors will be discussed.

The coordinate system used in the spectrometer is a right-handed one where the origin is near the targets, and z runs in the positive sense with beam. The y coordinate is in the vertical direction and x is horizontal.

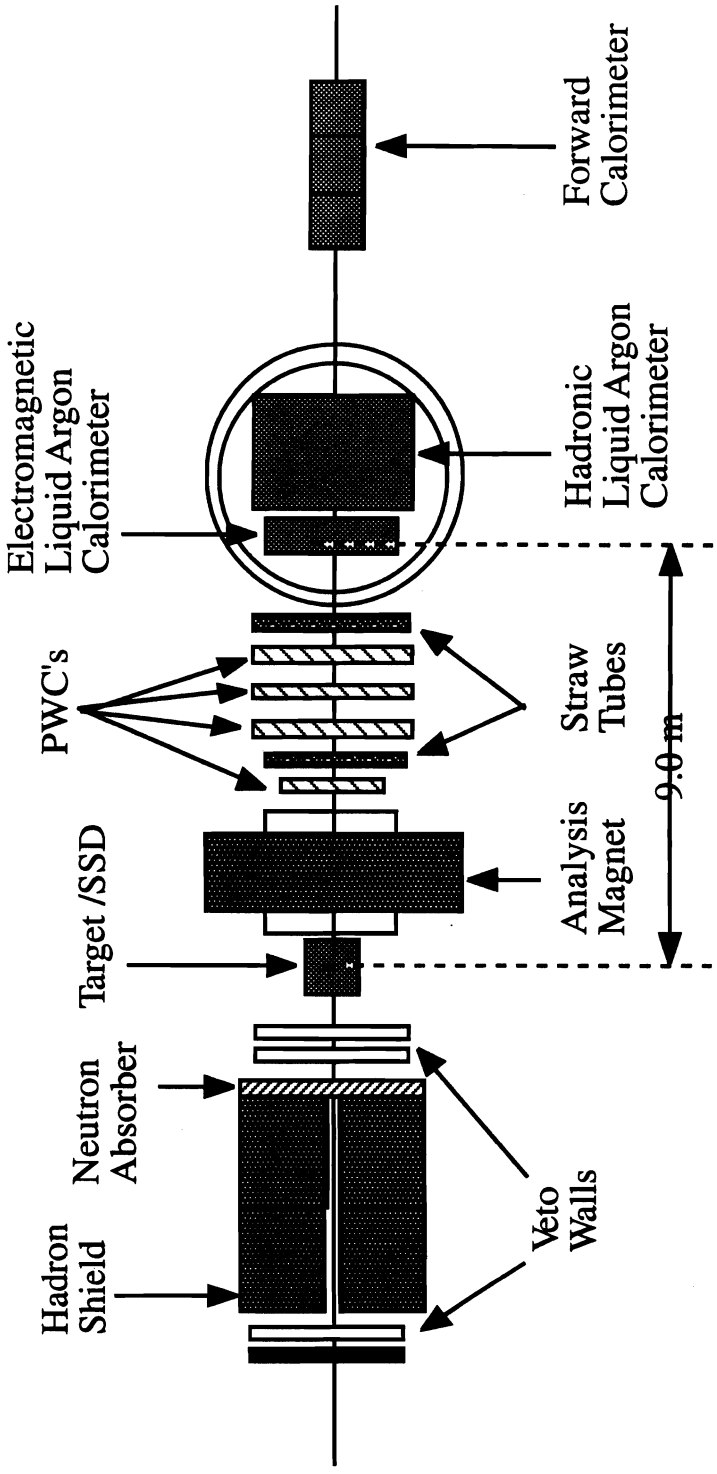

Figure 2.1: The E706 spectrometer. The beam enters along the line and from the bottom of the figure.

2.1 Experimental Beam

Fermilab supplies the beam for experimental use in the spectrometer. At FNAL the beam starts off as puffs of hydrogen gas which are ionized by adding an extra electron to the hydrogen. These negative hydrogen ions are then accelerated by a Crockcroft-Walton accelerator to 750,000 eV (750 KeV, eV = one electron volt = 1.6×10^{-19} coulombs $\times$ 1 volt., is the potential energy an electron experiences in a 1 volt potential). The negative ion beam is then injected into a linear accelerator which accelerates the beam to an energy of 400 MeV. The linac is 500 feet in length, and consists of a series of radio frequency (RF) cavities that act as wave guides through which an electromagnetic wave is sent to accelerate the ions. The geometry of the linear accelerator consist of a copper tube. In this tube there are several plates spaced at intervals related to the acceleration of the beam. These plates form the RF cavities. These plates have holes in the middle through which the ions pass. An ion entering the linear accelerator will experience an electric potential from the plate directly in front of it causing a force to pull the ion forward. As the particle approaches the plate the force decreases, and as it passes the center of the hole the force is zero. After it passes the hole the polarity on the plate changes, and the particle is now being pushed by the plate, and the next plate in front of is also now pulling on it. The voltage (hence, the electric field) on the plates goes as $\sin(\omega t + \phi)$, ω is the RF wave frequency. Thus, the ion continuously gets boosted as it passes through each of the RF cavities.

After the ion beam leaves the linac, the beam of negatively charged hydrogen atoms passes through a carbon foil that strips off the electrons. The bare protons are then injected in a booster synchrotron ring that is 500 feet in diameter. Here the protons are bunched into buckets and accelerated to 400 MeV. Dipole magnets in the ring keep the particles bent ($\vec{F} = e(\vec{v} \times \vec{B})$) in a circular orbit in the ring while they are being accelerated by RF field in the ring ($\vec{F} = e\vec{E}$) . Quadrupole magnets

keep the beam focused. The beam can be thought of as a light ray with magnets as lenses: dipole magnets are prisms that bend light, and the quadrupoles are focusing convex lenses or defocusing concave lenses. If a quadrupole focuses (convex) in one view, say x, it tends to defocus (concave lens) in the other view, y. Quadrupoles occur in pairs to compensate for this effect. As the beam is accelerated, the current in these magnets must be increased to provide more bending force for the faster moving protons.

The protons are then injected into the five mile in circumference main ring, which operates just like the booster ring (just much larger in circumference), and accelerated. The main ring is 20 feet underground in a tunnel that is ten feet in diameter. The main ring consist of 1000 conventional copper coil magnets. These magnets are quadrupoles and dipoles. The quadrupoles keep the beam focused, and the dipoles keep the beam bent into a circular orbit through the ring. The current in these magnets is ramped up to provide more bending and focusing force on the protons as they are being accelerated. In the main ring the protons are accelerated to 150 GeV.

Finally, the beam of protons is injected into the ring of superconducting magnets called the Tevatron (called that since it accelerates protons to about 1 TeV in energy), and accelerated to a final energy of 800 GeV. The Tevatron is in the same tunnel as the main ring, and its superconducting magnets form a ring placed underneath the main ring. The superconducting magnets provide higher magnetic field strengths, thus allowing for a larger acceleration of the protons. Also, the superconductors save energy since the superconducting wire used to coil the magnets has no resistance in its superconducting state. After final acceleration, the beam extracted from the Tevatron, and divided up and steered into the three fixed target areas: meson (where E706 is), proton, and neutrino. The meson beam line is then split further between other experiments and test beams, but the most of the intensity is directed toward E706.

Particle Id	beam
π^-	97.0%
K^-(Kaon)	2.9%
$\overline{p}$(anti-proton)	.1%

Table 2.1: beam content.[ref. G. Alverson et al., *Phys. Rev.* D48 (1993), 5]

The acceleration process operates on a 58 second cycle using the first 35 seconds to accelerate the primary protons to 800 GeV, and the next 23 seconds during which the beam is extracted out of the main accelerator ring, and steered down a vacuum beam pipe to the E706 spectrometer. Within each spill the beam particles are contained in RF buckets whose temporal frequency is related to the RF cavities of the accelerator (running frequency of the accelerator is 53 MHz). Each bucket is about 20 nanoseconds in duration, and has a beam occupancy that obeys Poisson statistics.

During the course of the 90-91 run the spectrometer saw four different beam types. For primary proton data the spectrometer of the 1991 run saw 800 GeV protons out of the Tevatron directly. For the pion data of 1990, a primary Be target was placed one-quarter of a mile upstream of the spectrometer in the main meson lab The target was 1.14 interaction length of Be in which the secondary pions were produced. The 515 GeV/c π^- secondaries were produced with a yield of 3×10^7 per 10^{12} primary protons. A magnetic spectrometer swept particles of different momenta and charges away from the beam line headed to E706. However, different particle species with different masses, but same charge and momentum would not be swept away so they must be dealt with by other means. In this thesis only negative 515 GeV pion data that was collected in 1990 is used.

Beam contamination of the π^- beam with other particles produced in the upstream Be target is listed in table 2.1. For particle identification a 42 meter long Cherenkov counter could be used [6]. It was located 98 meters upstream of our spectrometer. When a relativistic particle enters a medium where the index of re-

fraction is less than unity and the speed of the particle is greater than the speed of light in that medium, it will emit electromagnetic radiation much like an airplane that breaks the sound barrier emits a shock wave of sound in air. This radiation forms cones of radiation whose vertices are on the trajectory the particle has taken. This is Cherenkov radiation. At the opposite end of the cylindrical radiator from where the particle has entered, the rings of radiation, where the cones of radiation intersect the end of the cylinder, can be detected by phototubes. The angle that this radiation makes with the trajectory of particle is calculable. Cherenkov radiation goes as $cos(\theta) = \frac{1}{\beta n}$ where, β is the velocity of the particle ($\frac{v}{c}$), and n is the index of refraction of the helium gas medium. So, for a beam of identical momentum particles, but of different masses, particle species can be identified through differences in β. Rings of the phototubes were positioned in such a way to as to be sensitive the angle of Cherenkov radiation from major beam particle contaminants so they could be easily tagged. In the offline analysis, tagged events can be cut on, thus giving a cleaner sample of π^- interacting on the nuclear targets of Cu and Be. The tagging was not used in this analysis.

Another important source of contamination of the beam in the spectrometer were halo beam particles. These come from scatters in the initial upstream targets, and the decays of beam particles. To rid the experiment of these unwanted hadrons (μ^-,K^-,$\overline{p}$, etc) 900 tons of steel 5 m long in the z direction was installed to absorb hadrons. As the hadrons are being stopped in the shield they are producing neutrons from collisions with nuclei of atoms in the shield. To stop these neutrons a tank filled with water was installed behind the hadron shield.

Beam halo muons (μ^-) that come from the decays of π^- in the beam are another large source of contamination. Muons will penetrate the hadron shield and water tank, and if they strike the electromagnetic calorimeter (EMLAC), they can fake a high p_t trigger (see trigger section). To guard against this, a veto wall of scintillator that shadowed the triggering octants of the EMLAC was installed to veto these

fake events in the offline analysis.

Beam halo particles close to the beam and not cleaned up by the veto wall cleaned up by installing a beam halo counter to veto triggers caused by these particles. This counter was round in shape, with a hole the diameter of the beam in the middle of the counter. Thus, the beam could pass through and not fire the counters, but a particle traveling parallel to the beam would fire the counter. Thus, if these two counters fired in coincidence, then it can be assumed that this was a beam halo particle, and the trigger fired by it vetoed.

2.2 Targets

After the primary beam was accelerated, extracted, strikes the primary target producing the secondary beam, and is filtered, it enters the E706 spectrometer, and may interact (about 10% of the beam interacts and the rest goes right through the spectrometer) with the spectrometer targets producing interesting physics events. During the 1990 run Cu and Be targets were used. The thickness of the targets differ, but in terms of radiation length (a radiation length is the distance a particle travels to loose e^{-1} of its energy through electromagnetic radiation) they are the same. refer to 2.2 for the thickness and positions of the targets. By using two different target materials, cross sections for different materials can be measured, and nuclear **A** dependencies can easily be determined by taking ratios of particle productions off of each target, independent of beam normalization and reconstruction efficiencies. In figure 2.2 the target configurations are shown along with the silicon microstrip detectors. The silicon microstrip detectors record charged tracks that result from a beam particle collision in the targets. These silicon stripe detectors will be discussed later in the chapter. For the 1990 run the targets were offset off of beam axis in the x direction by 1.12 cm [7], so corrections for beam normalization had to understood (see figure 2.3) because most of the incident beam missed the target, but fired the beam hodoscopes counting incident beam. (This was true

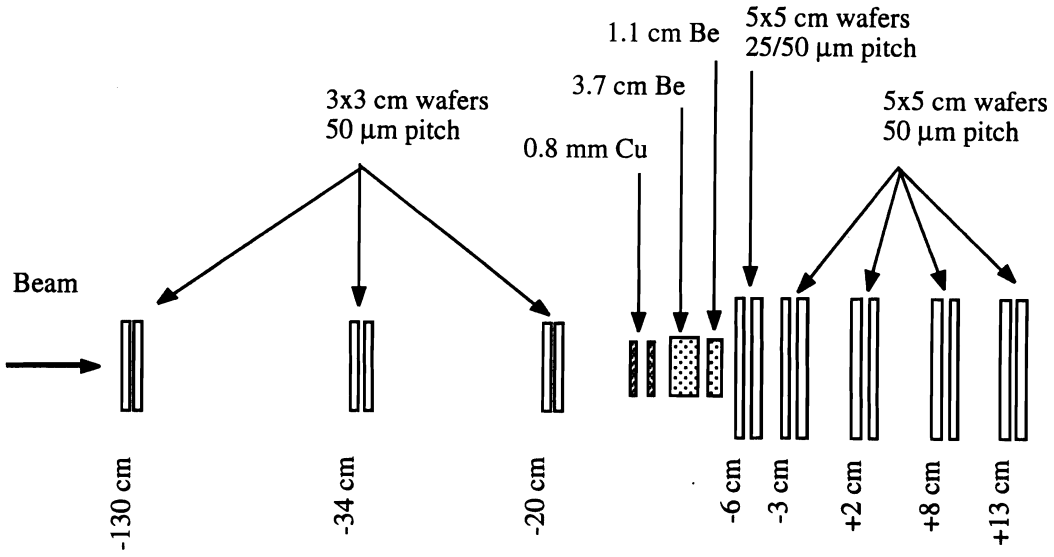

Figure 2.2: The 1990 targets of Cu and Be pieces with silicon microstrip detectors. The three planes before the targets track beam particle entering the spectrometer to interact in the targets, and the planes after the targets track charged particles that are produced in collisions.

only for the **INTERACTION** and **BEAM** triggered data since the **BH VETO** was not installed in these definitions. For the high p_t trigger The BH counter reduced this effect by vetoing beam that missed the target, and the correction to the normalization is much less than what was used here [8]) Figure 2.4 shows a histogram of v_z (v_z is the reconstructed vertex position of the interaction in the coordinate z.) vertices reconstructed over all events that occurred in the interaction trigger. In this plot one can see the beam adsorption that occurs by noticing that each successive target has slightly fewer entries (this effect is corrected for in the analysis by the ABS discussed in the analysis chapter). There are also vertices caused by material in the spectrometer other than the targets.

2.3 Triggers

Once a collision has occurred in the targets producing particles, the spectrometer must then fire a trigger to tell the data acquisition to read out the detector elements

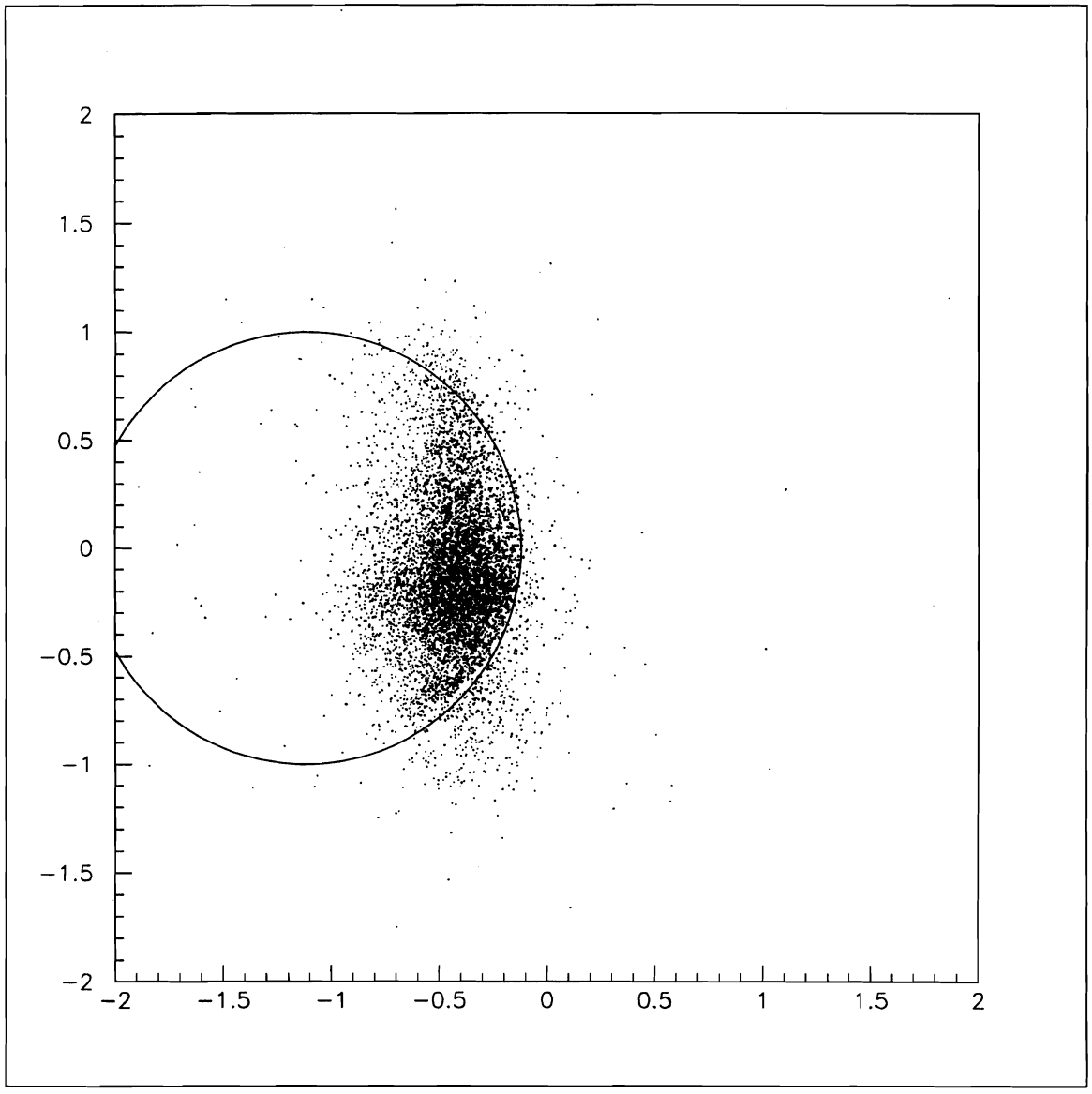

Figure 2.3: Vertex position in y (vy) versus vertex position in x (vx) showing target misalignment with the beam axis and beam hodoscope axis at 0,0. The circle shows the profile of the Be target.

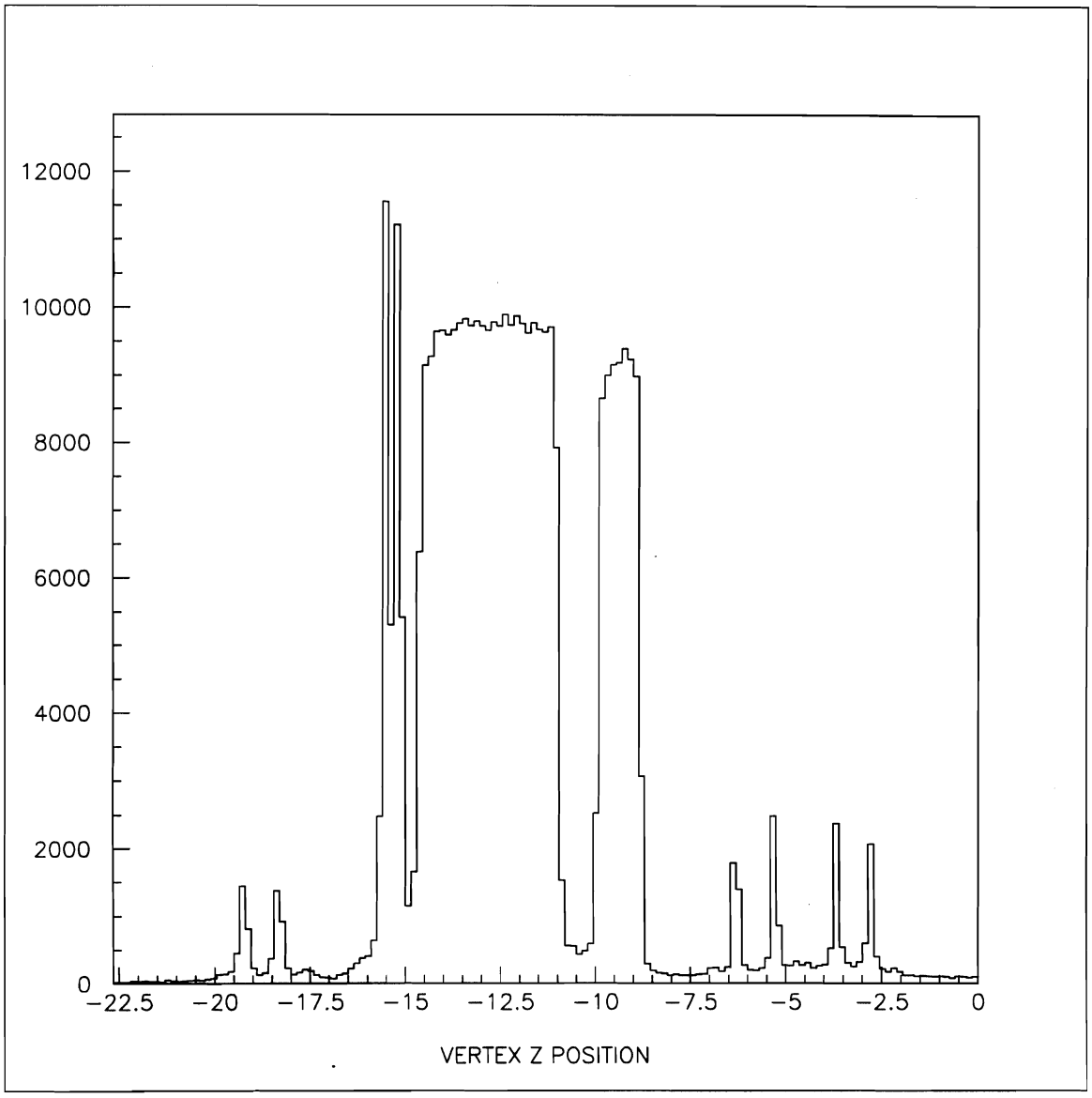

Figure 2.4: A vertex distribution in z across the targets. The targets are clearly defined. The background is due to beam interaction with material other than that of targets, such as the Rohacell target holders.

for a data event. The trigger consisted of three stages

- Beam and Interaction trigger
- pretrigger
- final trigger

The first stage of the trigger is the beam trigger. That is the beam must have fired the beam hodoscope to define a beam particle. Minimum bias beam triggers were read out using only beam events. This trigger was scaled back or "pre-scaled" since every event is beam event, and most of these events have low p_t. Next, the interaction counter would have fired if there was an interaction. Interaction minimum bias data was triggered if the beam hodoscope and the interaction fired, pre-scaled as to not dominate the trigger rate. From these two trigger definitions, then information from the liquid argon calorimeter is used to trigger to form the higher level triggers. The pre-trigger was used to form the higher level trigger decisions. The pretrigger tells the data acquisition (DA) to latch all the information deemed interesting by the DA hardware, then a full trigger is issued, and a full read out by the DA occurs where hits and signals are written to tape as raw data. During this time the spectrometer is dead, and cannot record any more data. The pretrigger cut down on this dead time by quickly rejecting uninteresting events that do not pass online cuts (such as low p_t events), and turning the spectrometer back on to wait for a more interesting event. There were triggers read out using only the pretrigger definition, but these were also prescaled.

In E706 there were 9 kinds of triggers set to pick out and discriminate certain physics events of interest. There were two minimum bias triggers, six EMLAC triggers, and a di-muon trigger used by E672.

Later offline, the hits and pulse heights of various read out elements are reconstructed into energy and tracks, which are then further processed into four vectors

of momentum and energy for use in data analysis. This is discussed in the event reconstruction chapter.

2.3.1 Beam and Interaction Triggers

As a beam particle entered the spectrometer it passed through 3 sets of beam hodoscopes that consisted of 12 scintillating fingers of strip widths ranging in width of 1 mm to 5mm to give spatial resolution to identify multiple beam particles. This counter forms the basis of the beam trigger. The definition of a beam trigger is

$$BEAM = (beamhodoscope) \bullet BEAM\,GATE \bullet RF\,CLOCK \bullet CMPRDY \quad (2.1)$$

For a **BEAM** logical signal to have been generated, the beam hodoscopes must fire in coincidence with a signal from the accelerator **BEAM GATE** which, when true, states that valid beam is coming into the spectrometer. This was in coincidence with the **RF CLOCK** which puts the trigger in coincidence with an RF bucket that contained a beam particle. **CMPRDY** was the logical signal generated by the Data Acquisition(DA) computer, and it will be true if the computer was ready and waiting for an event, or false if it was busy doing something else and so the spectrometer was "dead".

A higher definition of the beam trigger was **BEAM1**. This definition required that there be one, and only one hit finger in the beam hodoscope. This insured events were singly occupied.

The beam definition formed the basis for higher level triggers. If a higher level trigger was not met this could be read out as a trigger. Events were read out with this definition only, but prescaled by 15^6 so that the read out system would not be saturated by events not interesting to direct photon production. Beam triggers are useful to do cross-checking with other trigger definitions. As a result of this

configuration, one can study events that are not biased by higher trigger logic (i.e. minimum bias). Ninety percent of the events triggered by this definition did not have any interaction.

The next level of minimum bias trigger was the interaction trigger. After the target, and before and after the magnet, there were placed four interaction counters. These scintillating counters were labeled SE1 and SW1 (7.6 $\times$ 15.2 cm) which were located before the magnets, and SE2 and SW2 (10.2 $\times$ 20.4 cm) after the magnet. These scintillators shadowed the calorimeter and were instrumented by photo multiplier tubes. These counters each had a hole in the middle aligned with the beam axis. The hole let the non interacting beam pass through. If an interaction occurred, then particles produced in the collision would pass through both sets of scintillators causing them to fire in coincidence. So, if there was a coincident hit in both sets of paddles, then the beginning of an interaction trigger could be formed.

A scintillator that was circular, but with a hole cut out of middle that had the dimensions of the incoming beam, was used as a beam halo counter (**BH**). The purpose of this counter was to test if the interaction trigger was fired by a beam halo particle as discussed in the beam section. It vetoed the interaction trigger if it did fire. This veto was only active in the high p_t trigger definitions of an interaction. In the minimum bias interaction, **INT**, trigger this veto was not present.

Since the rate at which triggers could be accepted was about 1 MHz, a clean signal (**CLEAN**) was generated if no interactions were produced ± 3 buckets (± 60 ns). This gives a clean event with no pileup from other interactions occurring too close together in time. The **CLEAN** signal was achieved by sending the interaction signals to a delay unit and then "ORing" them together.

An interaction trigger strobe can logically be written as

$$LIVE\ INT = BEAM \bullet INTERACTION \bullet CLEAN_{INT} \bullet \qquad (2.2)$$

This was used as the interaction definition in conjunction with other logic to form higher level triggers. Triggers were read out with this definition as the minimum bias interaction trigger, but accepted at only a rate (pre scaled) of 15^5 triggers. This was done so that low p_t events would not dominate the data taking rate. This trigger was used to study the low p_t end of the π^0 scale of the cross section. This trigger was used in this thesis.

2.3.2 Higher Level Triggers

The definitions of beam (**BEAM1**) and interaction (**INT**) triggers form the basis of the higher level p_t discriminating triggers with the exception that they also included the beam hole, BH, veto. These triggers were based on how much energy was deposited in the EMLAC (to be discussed later in the chapter). In order to minimize the dead time introduced by a LAC trigger decision, a pretrigger was formed.

To form a p_t discriminating trigger, energy information from the EMLAC was used in order to make an online trigger decision. In the LAC there were concentric rings of active strips of 0.5 cm in width as shown in figure 2.8. These strips collected the charge ionized (the amount of ionized charge is proportional to the energy) in the liquid argon gap between the strip and the lead sheet by showering particles. The strips of the same i^{th} index are wired ORed together to form a r channel (The front 1/3 section of the EMLAC channels are ganged together, and the back 2/3 are ganged together and it is the front 1/3 used to determine a trigger.) When a photon strikes the EMLAC a shower builds up and part of its energy is sampled by the r strips. The energy of the photon that initiated the shower is quickly estimated by the LACAMPs fast out (see EMLAC read out sections) for each EMLAC channel r_i. For each r_i channel the energy is e_i. The distance of the shower from the z axis is taken as the centroid of the r_i stripe. Thus, the p_t for a triggering octant in the LAC can be estimated as

$$p_t = 2\sum_i e_i \sin(\theta_i) \approx 2\sum_i e_i r_i/900. \quad (2.3)$$

For a photon $E = |\vec{p}|$, and θ is the angle the photon makes with z. The 900. cm is approximate distance from the targets to the face of the LAC, thus estimating the point of interaction to within a few cm, and r_i is distance of the i^{th} r channel from the z axis. The factor of two is because only every other read out board in the LAC is r view board. The other interleaved boards are boards that have radial strips that give the ϕ position of the shower. The energy collected in the ϕ view was not used in the trigger boards. Further, it is assumed that half the total energy of an electromagnetic shower is integrated in each view. The equation 2.3 is taken over contiguous 8 strip sections. A threshold of $1.7/;GeV/c$ on p_t was used to determine whether or not this trigger would fire. So, for a given octant pretrigger to fire, the following criteria had to be met in coincidence:

- **LIVE INT** signal (there was a clean interaction)
- A total p_t deposit within the innermost 128 R strips or outer most 128 R strips of $p_t > 1.7GeV/c$.
- There was no p_t within the preceding 200 ns of greater than $1.5GeV/c$.
- No incident muon as identified by the veto walls upstream of the spectrometer.
- The absence of a power supply noise spike strobed by SCRKILL (this reduces the accidental rate of triggering on a noise spike).

The final pretrigger was generated by the logical OR of all the octant pretriggers. If the criteria listed above was met, then a pretrigger signal was issued. This signal was sent to the BATs (BEFORE and AFTER timers) (in crate 20 of the DA trigger hardware) to initiate a BEFORE and AFTER time sequence so that

subsequent LAC triggers could not be issued. Also, a **LOAD** strobe was sent so that the forward calorimeter (FCAL), proportional wire chambers (PWCs), and the silicon microstrip detectors (SSDs) could be latched for read out by the DA.

Now that a pretrigger was issued, a higher level trigger could be evaluated to determine the type of high p_t event that occurred. Three types of octant triggers were defined: global p_t, a 1/2 global p_t, and a local p_t signal. The 1/2 global trigger is based on the total amount of p_t deposited in the inner 128 strips or in the outer 128 strips of the octant. The local p_t signal corresponds to the sum of sixteen contiguous r channel strips. This is about 8 cm in width which corresponds to the width of one photon shower. Thus, the experiment could quickly estimate the amount of p_t deposited by one photon. The local p_t signal was used to determine if a global p_t was generated by multiple low p_t photons whose sum of p_t is high.

Using the three definitions of p_t signals, and two different levels of trigger threshold discrimination, it is possible to generate 6 LAC triggers whose definitions follow:

- LOCAL GLOBAL HI = (LOCAL LOW) $\times$ (GLOBAL HI)
- LOCAL GLOBAL LOW=(LOCAL LOW) $\times$ (GLOBAL LO)
- SINGLE LOCAL HI = LOCAL HI
- SINGLE LOCAL LOW = LOCAL LOW
- LOCAL 1/2 GLOBAL HI = (LOCAL LOW) $\times$ (1/2 GLOBAL HI)
- TWO GAMMA = $\sum_{\alpha\beta}$ (LOCAL LOW)$_\alpha$ $\times$ (LOCAL LOW)$_\beta$, where β is any of the three corresponding awayside octants to α

If one of these triggers fired, a trigger interrupt was issued to the DA to do a full read out of the spectrometer data latched by the pretrigger. If none of these definitions fired, then the pretrigger was cleared, and the read out electronics for

Trigger	Fraction of Data	Prescale Factor	Threshold
Single Local Hi	40%	1	3.5 GeV
Single Local Lo	18%	40	3. GeV
Local Global Hi	35%	1	3. GeV
Local Global Lo	20%	40	2.5 GeV
Two Gamma	20%	1	2.8 GeV
Interaction	3.1%	15^5	0
Beam	2%	15^6	none
Prescaled Pre	7%	15^5	none

Table 2.2: Triggers.

the PWCs, SSDs, FCAL, and LAC were reset. If a trigger did not fire then an pretrigger event may be read out, but this did not always occur since it was scaled back. If no trigger was accepted a delay of 20 μs followed before another potential trigger was accepted to allow the DA electronics to settle down. The amount of data acquired from each trigger is shown in table 2.2

There was also a di-muon trigger, E672, whose logic was calculated with their detector(their detector was directly behind E706), and a signal was sent to the E706 DA. Table 2.2 lists trigger type, and amount of data taken.

2.4 Tracking System

E706 had a charge tracking system that consisted of the following detector elements: silicon microstrip detectors (SSDs), proportional wire chambers (PWCs), and Straw Tube Drift Chambers (STRAWs). In this section the tracking system is discussed.

A beam particle comes in and interacts with the target causing multiple particles to be produced with a variety of energies and momenta. Most of the particles produced in the primary collision, the primary vertex position (vx, vy, vz) is where the collision occurred, can then further decay producing secondary vertices, and more particles(tracks) coming from the daughter products. These tracks will pass

through the interaction counters (as described in the interaction trigger section) and fire them, indicating that an interaction has occurred. The p_t of the event will be collected from the calorimeter, and will be evaluated to determine the trigger type. If it was a high level LAC trigger it will be read out. If it was not, then it may or may not be read out, depending on the scalar count of triggers and scale factor for the interaction, pretrigger, or beam trigger. Now that a trigger was satisfied, data from various pieces of hardware that recorded particle track "hits" in their elements could be read out so that later these hits can be used to reconstruct tracks, and energies in the offline reconstruction. Tracks from the primary collision in the targets were reconstructed in the upstream tracking system of silicon microstrip detectors. After the charged particles passed through the bending magnet, their tracks were reconstructed by the PWCs and STRAWs of the downstream tracking system. Tracks from the two systems were linked in the interior of the magnet to determine the amount of bending that occurred to a charge track. The amount of bending determines the momentum, and the direction of bending determines the charge of the particle.

2.4.1 Silicon MicroStrip Detectors

There were 8 sets of silicon microstrip detectors (SSDs) x, y pairs, with each pair consisting of two planes of silicon whose charge collecting diode p strip implants are orthogonal to each other providing x, y information for the hit. The z position is easily deduced from the fact that we know where the plane was placed in z. There were 3 pairs of SSDs before the target to define the beam particle track that caused the collision. These had an active region of 2.5 cm $\times$ 2.5 cm. The remaining 5 planes after the target recorded hits from the collision, and were used to reconstruct tracks of particles produced in the collision. The SSDs had an active area of 5 cm $\times$ 5 cm.

The SSDs are planes of silicon that consist of a n-type silicon substrate, with

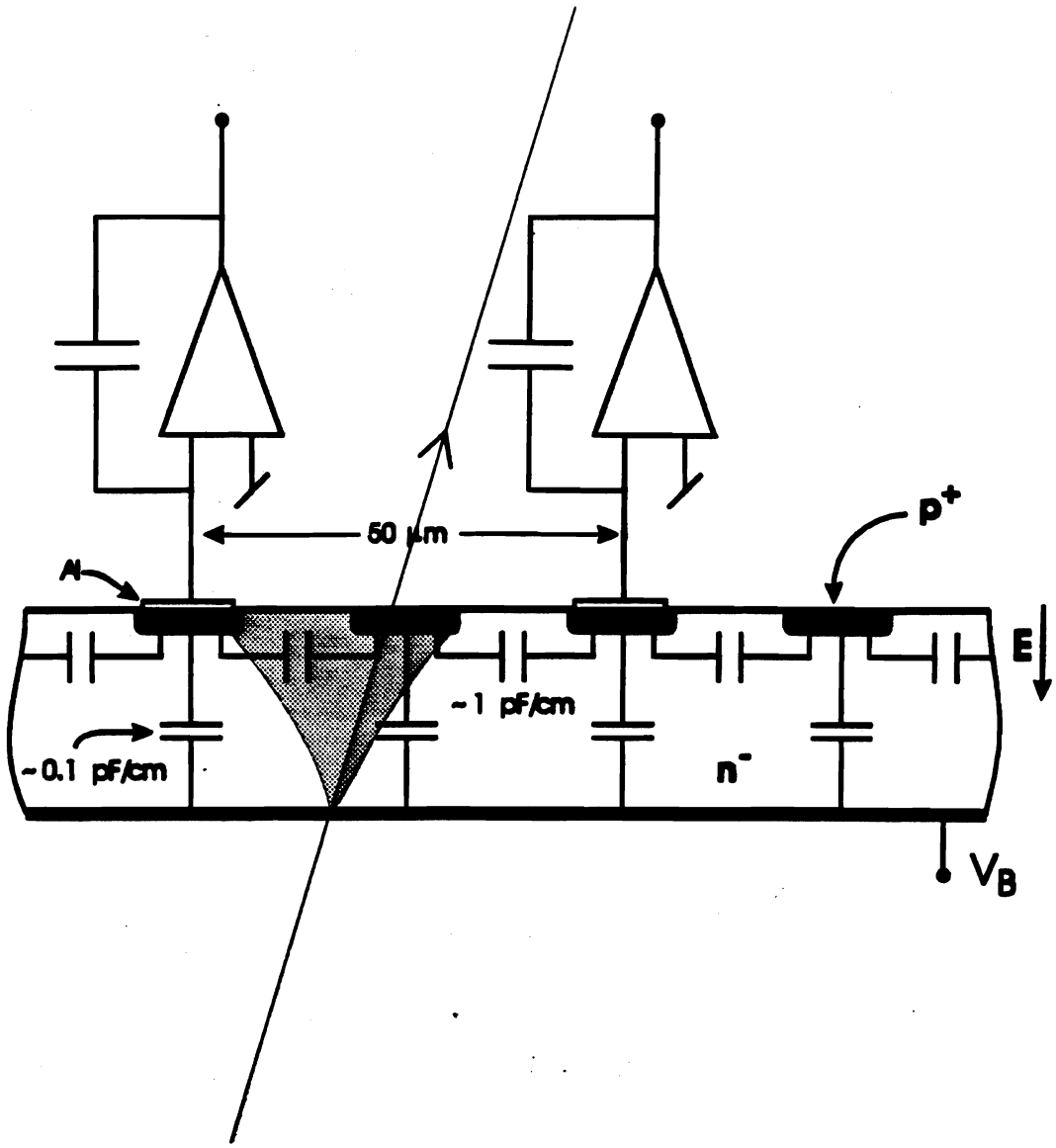

Figure 2.5: Slice of a SSD Plane. The bulk is n type silicon with p implants that form $p-n$ junctions. The back plane is aluminized and at $-V_{bias}$ volts. The charge sensitive amplifiers integrate charge collected on the p strips. The capacitors in the bulk silicon are not physical, but the component equivalent of how the junction behaves as a circuit. The shaded region represents the electrons diffusing to the surface through the silicon.

p type silicon implant strips that are $\approx$ 20 microns in width which run along the length of the device as depicted in figure 2.5. These form $p-n$ junction diodes with the n type substrate as shown in 2.5. The back plane of the n type conductor is metalized as well as the surface of each p strip. This allows a reverse bias voltage to be applied to the junction, and the collected charge read off the device. The p^+ strips are at 0 potential, and the aluminized back plane is at $-V_{bias}$, which is typically 40 volts (V_{bias} depends on the doping concentration and thickness of the Si). When a charged particle traverses through the Si, it creates electron-hole pairs in the depletion region as a result of coulombic collisions with the electrons. Being reversed biased, a depletion region of nearly the thickness of the device is created ($\approx$ 300 microns) and a strong electric field is present. This field carries the electrons, created by ionization, to the p strips where they are collected. The metalized strip is connected to a charge sensitive amplifier which integrates the current collected on the p strip, and stores the collected charge on a capacitor. The charge on the capacitor is then latched until the read out hardware queries the voltage on the capacitor.

Some of the charge integrated is due to leakage current (that is, the devices are not ideal $p-n$ junctions) and random noise fluctuations, thus setting up a baseline for defining a hit (which will be baseline plus charge created by an ionizing particle). The noise of each channel will have a Gaussian profile so that a hit can be defined as deposited charge in excess of 3 σ of the noise. Electronically, this is done by taking a sample before a hit and holding it on a capacitor; then sampling during a time when a hit is allowed to occur and storing it on signal capacitor. The charge on each capacitor is then differenced, and if the excess is above some set threshold, a hit on that channel can be declared. In all there were 8192 channels could be read out, but only hit channels were read out for speed of the data acquisition process.

Most channels will not have hits, and their integrated charge will just be that

of the noise. If there is a hit on a channel, then by knowing the strip numbers the an x, y estimate of the position can be interpolated. The read out pitch of most of the SSDs is 50 microns (the distance between the center of adjacent read out strips). If two or three neighboring channels are hit (a cluster), then an average is taken of the their positions to give an estimate of the position. The x, y resolution is around 14. (50 microns/$\sqrt{12}$) microns.

In the offline analysis, the hit information from the first three planes is used to do straight line fit to the incoming beam particle, and project it to a primary vertex position in the target. The hits in the SSDs after the targets were looped over, and straight line fits were applied to all combinations of hits using a least χ^2 criteria on the fits to determine which hits applied to which track. After this process a collection of fit tracks whose linear slopes and intercepts are now known. See chapter 3 for detail discussion of track reconstruction. These linear fits can then be projected back to a common intersection, and with the projection of the beam track, define a vertex (position of collision). Since the resolution in z is about 350 microns, an impact parameter of 100 microns [9] was used as a cut off in determining which tracks belonged to a vertex candidate. Tracks that did not come from the primary vertex were handled by a secondary vertex reconstruction code. To make it clear, the hit information in the SSDs is used to reconstruct the tracks from particles in the collision and find the vertex position. Refer to Chapter 3 for a more detailed discussion.

An important consideration for the SSDs was radiation damage. Since all of the beam passed through the SSDs, interactions in the SSDs occurred frequently, leading to radiation damage of the bulk silicon. Such damage consists of structural defects such as dislocations in the lattice of Si caused by beam particles knocking out atoms of Si from the lattice. Over time the dose of radiation builds up in the Si leading to a degradation in their performance. Most notably, the leakage currents from the reverse bias junctions go up, causing noises to go up. The diode is not as

good any more, and the signal pulse height goes down; thus, the ratio of signal to noise($\frac{S}{N}$) gets worse. As $\frac{S}{N}$ goes down, hits become lost in the noise; thus, detector efficiency goes down. For the π^- beam this was not much of a problem, but for the 800 GeV/c proton beam (higher radiation Q factor) it was a major problem such that towards the end of the run their performance was becoming noticeably degraded [10]

2.4.2 Analysis Magnet

After the SSDs, and before the upstream tracking system, there was a dipole magnet 2 meters downstream of the target. The magnet had a field such that it gave a momentum kick to a charged particle of 450 MeV/c in the x direction. This magnet served two purposes: first, the direction a particle is bent it gives the charge of the particle; secondly, the amount of bending this determines the momentum of the particle. This follows from the Lorentz force law, $\vec{F} = q(\vec{E} + \vec{v} \times \vec{B})$.

Tracks are independently reconstructed in the upstream tracking chambers, the SSDs, and the downstream tracking chambers then they are projected to the interior of the magnet, where they are linked up. From the linked tracks the entrance and exit angle of a track can be determined, and thus the amount of bend determined.

Mirror plates were installed, with square holes for the particles to pass through, at the beginning and at the end of the magnet to contain the field inside the magnet's volume. This is done so that the field would not have any influence on particles or any other detector elements outside of the magnetic volume. Also, a helium bag was placed inside the magnet to cut down on photon losses through pair conversion since He is less dense than air. That is photons might have a collision with a nucleus of an atom in an air molecule and undergo a conversion into an electron positron pair, and be lost.

2.4.3 Proportional Wire Chambers

Downstream of the magnet, there were four Proportional Wire Chambers (PWCs) with a total 13440 digital channels. Each module consisted of 4 planes of wires to form x, y, u, v views sandwiched between graphite coated mylar sheets that formed the cathodes (at 0 volts) as shown in figure 2.6 [11]. The active regions were 1.22 $\times$ 1.22 m^2, 2.03 $\times$ 2.03 m^2, 2.03 $\times$ 2.03 m^2, and 2.44 $\times$ 2.44 m^2. The wires are set to positive high voltage. The anode wires were 20 microns in diameter and were separated by .254 cm. The gas used in the chamber consisted of 79.7% argon, 18% isobutane, 1.1% isopropyl alcohol, 0.1% freon (called magic gas in the trade). When a high momentum charged particle passes through the gas and has a near collision with an atom of gas; an exchange of momentum high enough can occur to knock an electron free (usually just a few eV is required) and the gas becomes ionized. Under the influence of the electric field, the electrons will drift towards the anode. The electric field near the wire goes as $\propto \frac{1}{r}$, thus the intense field near the wire causes an avalanche. The diameter of the wire effects the avalanche because of the $\propto \frac{1}{r}$ dependence of the $\vec{E}$ field. An avalanche is where original drift electron generates additional electron-ion pairs which, in turn, generate even more electron-ion pairs multiplying the signal by orders of magnitude. The other gasses in the argon mixture cause a saturation of the generation of current in avalanche effect. This make the chamber highly efficient for a track of any energy. When the charge is being collected on the anode it is differentiated, and for a rapidly rising signal this will give a large derivative such that if it is above a preset threshold, signals a hit. Only the hit channels are read out as a digital logic.

In the chamber there are four planes of wires set to high voltage sandwiched between graphite coated mylar sheets at 0 volts. The first two planes of wires are orthogonal x, y pairs. The next two planes are an orthogonal set of u, v view that are rotated by 37 deg relative to the x, y view as shown in figure 2.6. The purpose of this is that if there are many hits on the PWC, then with only an x, y view it

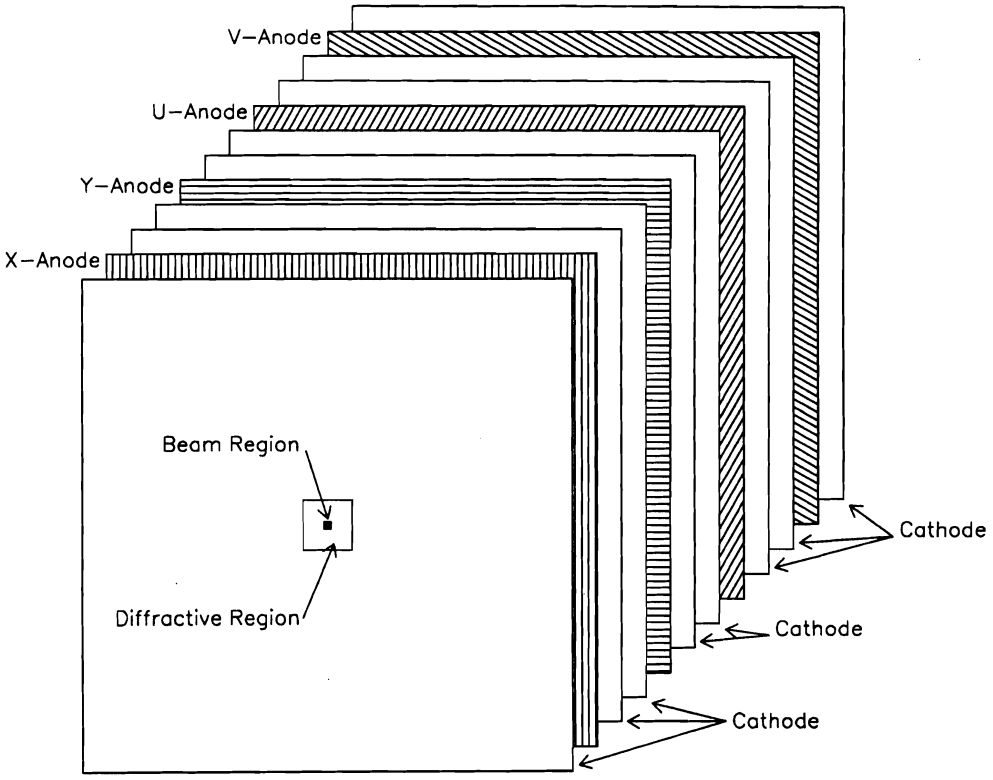

Figure 2.6: The construction of a PWC module.

will be difficult to match an x hit to its corresponding y hit to form the correct x, y pair unambiguously. By correlating hits in the u, v planes with hits in the x, y planes, x and y hits may be correlated unambiguously. See chapter 3 on track reconstruction. The resolution in x, y was 500 microns.

On the cathode, in the center a square region which was isolated from the rest of the outer region of the chamber. This was done because most of the beam does not interact and goes straight through the experiment, thus the beam intensity would make the voltages on the PWCs sag if the center region was not deadened.

2.4.4 Straw Tube Chambers

After the first and last module of PWCs, there were placed the straw tube proportional chamber (STRAWS) as shown in figure 2.1. The physics of how a STRAW works is similar to a PWC, but the geometry is different. The straw tubes are cylinders with wires at high voltage running down the middle of the tube. The straw tube walls were tubes of mylar aluminized on its interior at 0 volts. The diameters were 10.4 mm in the upstream module and 16.3 mm for the downstream module. Each module contains four planes of straws arranged in bundles such that when a hit occurs; and, a radius from the wire is measured, it can be discerned on which side of the wire it occurred. See figure 2.7 for an illustration of how this works. There were four modules used in the experiment. Two modules in the first set and two modules in the second set. The location of the sets is shown in figure 2.1. Set one is most upstream and set two is the down stream set. Within each set, one module the tubes were vertical for measurement of positions in x, and in the other the tubes were horizontal for measurements of y position.

When a charged track passes through the chamber, it ionizes the gas (the gas is similar to what is in the PWCs) in each tube into electron ion pairs. The electric field in each tube runs from the wire to the wall in the radial direction, thus the electrons are swept toward the anode wire. The electric field in the tube provides

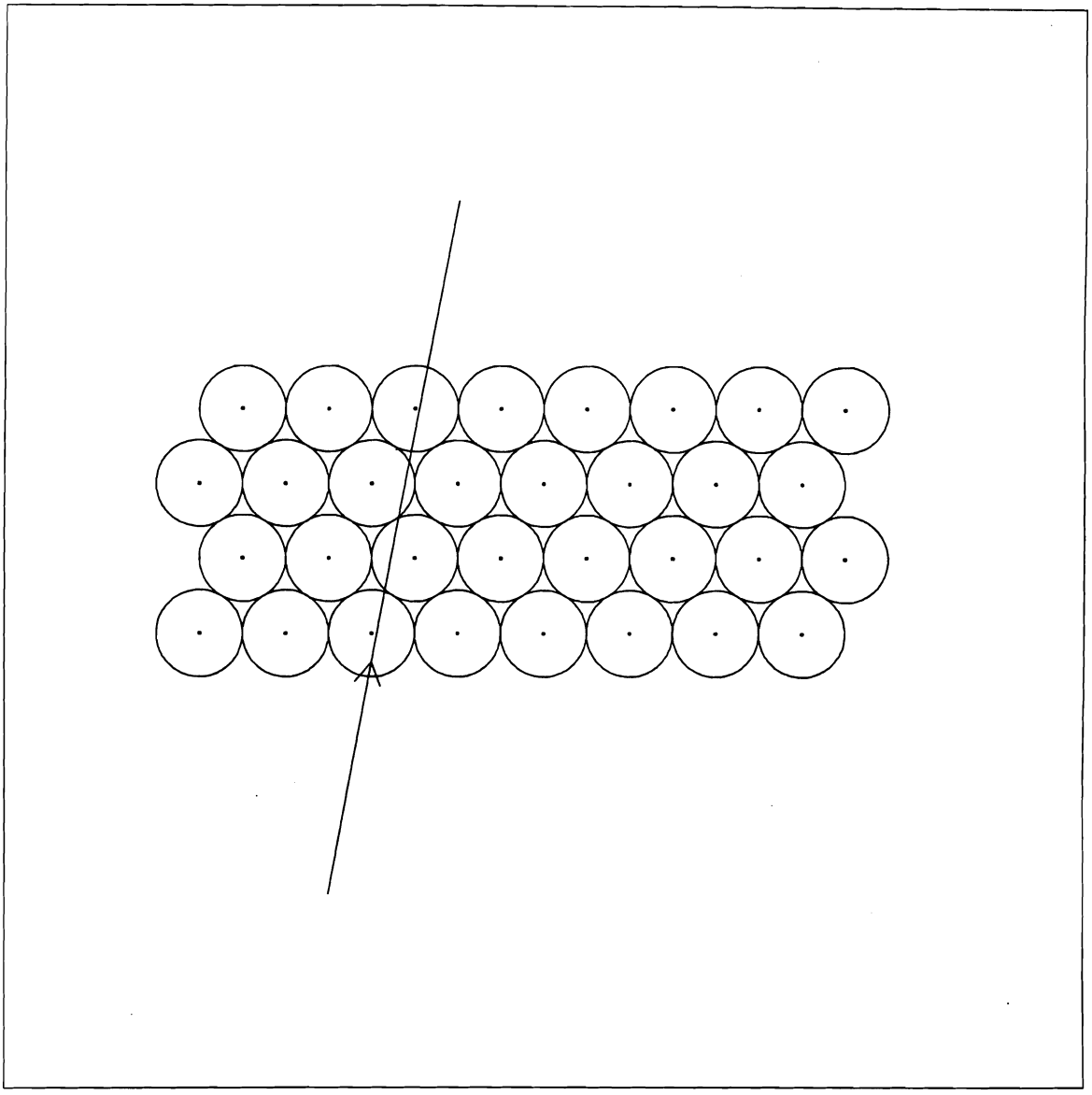

Figure 2.7: STRAW module. A charged particle track ionizes the gas in each tube, thus the r position from the wire can be measured by measuring the time it takes for the ions to drift to the sense wire. The stagger in the planes removes left right ambiguities

acceleration for the so $r \propto t^2$ where r is the radial distance from the wire. The radial distance from the wire anode is measured by using time-to -digital converters (TDCs) to measure the drift time from the ionization point to the anode. From this time in the tube the r position can be measured. By looking at the r positions in each plane the lab coordinates of the track can be deduced.

The resolution of the straw chambers is 250 microns compared to the 500 microns of the PWCs, thus the straw chambers help improve the momentum determination of charged tracks.

2.5 Liquid Argon Calorimeter

The "star" of the E706 fixed target experiment was the Liquid Argon Calorimeter (LAC). The LAC was designed to be a highly segmented sampling calorimeter used to measure the energies and positions of photons, electrons, and hadrons. The LAC consisted of two parts: The electromagnetic section (EMLAC), followed by the hadron calorimeter (HLAC). Photons and electrons start showering sooner than hadrons, so the first 30 radiation lengths (radiation length is when a particle transverses a distance such that it looses 1/e of its energy) is the EMLAC, and the rest of the back section is the hadron calorimeter. The construction of the HLAC is different from the EMLAC, but since it was not used in this analysis it will not be discussed (see [12] for a discussion of the HLAC)

2.5.1 The Electromagnetic Calorimeter

See figure 2.8 for a physical picture of the LAC. The LAC was positioned 9 meters downstream of the target. The EMLAC consisted of cells made from R and ϕ boards that form a cylinder 3 meters in diameter, and 71 cm in depth with a 40 cm hole in diameter. The hole in the middle prevented the beam from overloading the detector causing the bias voltage to sag. Since most of the beam does not interact it passed through this hole. If there were dense material in this region,

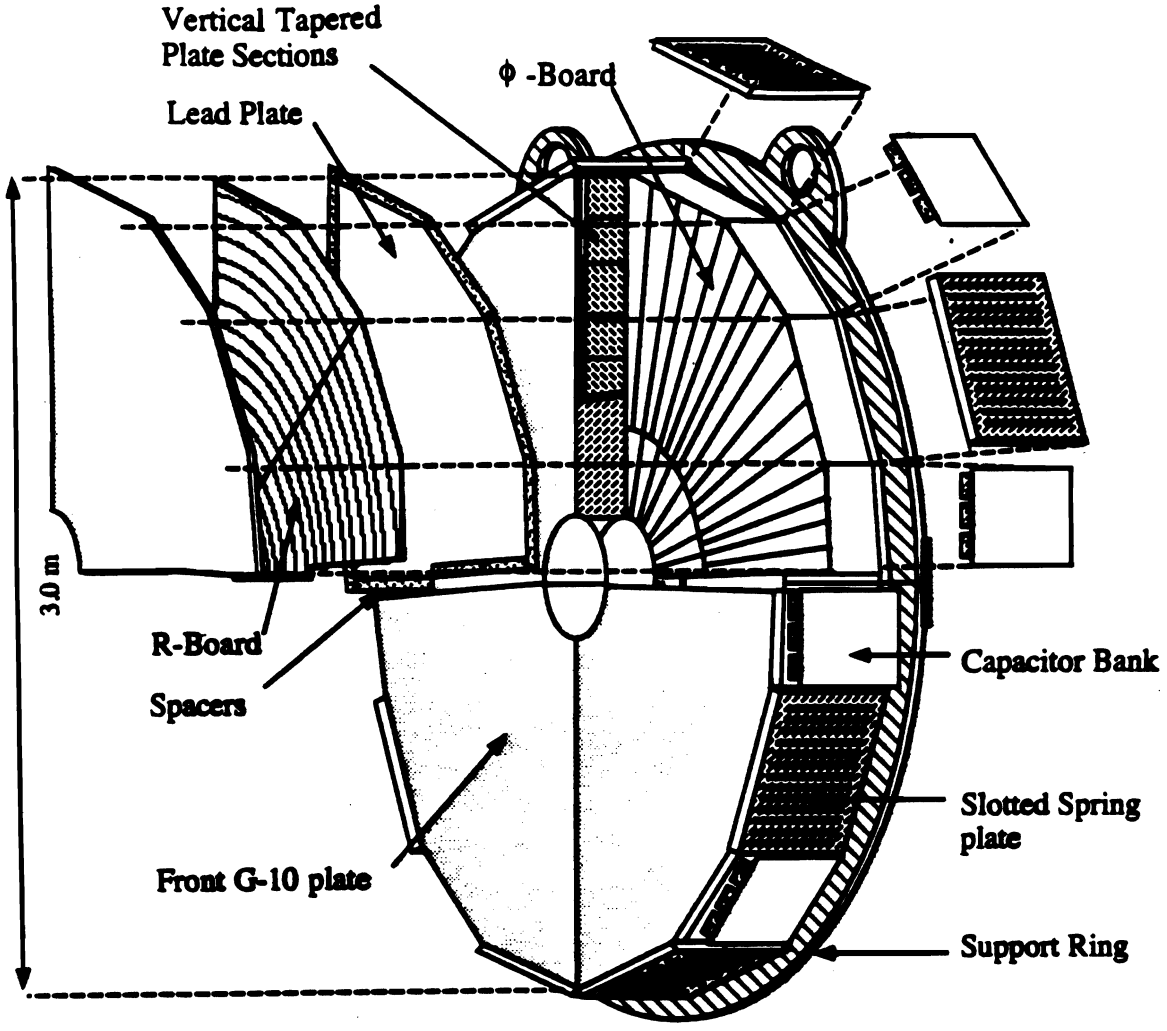

Figure 2.8: The construction of the EMLAC. Shown are the Radial and ϕ boards used to collect the charge of an electromagnetic shower, and provide positions of the photon hits. The concentric rings that form the r boards are used in the definition of high p_t triggers. The lead plates act as an absorber creating the electromagnetic shower that ionizes the liquid argon gaps between the G-10 radial and ϕ boards. High voltage between the lead plates and G10 boards creates an electric field which will cause the electrons created by the ionization of liquid argon to be collected at the G10 boards

the beam could then interact with the material and spray particles all throughout the LAC. The acceptance of the LAC for a track originating in the target region had a polar angle $1.3\,\mathrm{deg} < \theta < 10\,\mathrm{deg}$ over $0 < \phi < 2\pi$. In a variable called rapidity (Y) (which is discussed in the analysis chapter 4), this corresponds to an acceptance of $-1.0 < Y_{cm} < 1.0$ in the center in the center of mass frame (However due to efficiency of the EMLAC, the range in rapidity is $-0.75 \leq Y_{cm} \leq 0.75$.) The forward calorimeter, made from scintillating plastic, covers the small angles that the LAC misses due to the hole (see spectrometer figure 2.1.)

The EMLAC consisted of 4 mechanically independent sections or quadrants. Each quadrant consisted of 66 layers, each layer being 0.8573 cm thick. Each layer consisted of a 0.2 cm thick lead sheet, followed by a 0.25 cm argon gap as the ionizing material, followed by a G-10 copper clad anode board with either a r view or ϕ view etched on it, followed by another 0.25 cm liquid argon gap. Energy loss, ΔE, through a material by a relativistic particle can be characterized by $\Delta E = \Delta x/x_0$. The constant x_0 is what is called the radiation length, and Δx is the distance traversed through the material. So, for the 66 layers the total distance in terms of radiation length is

$$x = (\frac{.2}{.56} + \frac{.5}{14.} + \frac{.16}{19.4}) \times 66 = 26.47\text{radiation lengths} \qquad (2.4)$$

Where the first term is the thickness of lead divided by its radiation length, the second term is for the two gaps of argon, and the last term is the G-10 board. Adding in material in front of the LAC, the total number of radiation lengths is ≈ 30. At 30 radiation lengths virtually every photon and electron will shower, and its total energy will be deposited in the EMLAC. The lead plates were a mixture of 98.6% lead, 0.07% calcium, and 1.3% tin. The Ca and Sn were added to stiffen the lead so that it would not buckle under its own weight.

Lead is very dense, thus making it an ideal absorber. Photons that hit the lead sheets will form electromagnetic showers within a reasonable depth in the EMLAC. An electromagnetic shower is started by the pair conversion of a photon into an

e^+e^- pair through an interaction with a lead nucleus. The e^+/e^- pairs ionize the liquid argon. The e^- and e^+ from the initial pair will bremsstrahlung high energy photons. (Bremsstrahlung radiation is produced when charged particles are being stopped in material through electromagnetic scattering off of the nuclei of a material, and in German it literally means "braking radiation".) Photons that result from the bremsstrahlung radiation will pair produce again. These pairs will also ionize the argon, and they will also generate bremsstrahlung photons which will produce more pairs to ionize the argon and more photons to create more pairs. Thus an electromagnetic shower builds up in the EMLAC. Most of the energy is lost in the lead of each layer that acts as absorber to build up the shower. Part of the energy is lost by ionizing the liquid argon ($\approx$ 20% of the total energy of the shower). A voltage is applied between the G-10 board and the lead (at high voltage) across the argon gap so that the electrons created by ionization of the liquid argon can be collected, and their charge integrated on LAC amplifiers (LACAMPS). This method is called sampling calorimetry since only part of the energy is actually measured. Thus, the calorimeter must be calibrated against something known to set the energy scale, and in E706's case it was the π^0 and zero mass electron pairs that come from the pair conversion of photons in the material upstream of the LAC. (see ref. [13] for a detailed discussion of the energy scale).

A radial (r), and azimuthal (ϕ) cylindrical coordinate system was chosen as the natural geometry to read out the EMLAC. The cells of the calorimeter were filled with alternating r and ϕ boards. The radial coordinates are given by copper cladded G-10 boards with concentric rings of 256 (numbered 0 to 255) strips etched on the surface. The concentric r strips are arranged in such a way that they focus on the targets as shown in figure 2.9. To achieve this the width of each strip goes as

$$w_i = \frac{0.5466}{900.0}(900.0 + 1.56(1 - i))\ cm \text{ for i}^{th} \text{ radial board} \qquad (2.5)$$

The radial distance from the z axis to the center of the r strip is

$$r_i = w(i) \times (21.59 + 0.5466)\ cm\ \mathrm{j}^{th}\ \text{strip on i}^{\text{th}}\ \text{radial board} \qquad (2.6)$$

Each r board for a quadrant was electrically divided (a small gap in the copper concentric ring strip) into two sections splitting the EMLAC into octants.

The azimuthal boards were electrically split into an inner region containing 96 radial copper strips, and an outer region containing 192 radial strips. The inner/outer split at 40 cm was designed to improve the spatial resolution in ϕ by reducing the strip width by a factor of two. The inner, and outer parts are read out separately. This was done so that the inner strips would not be so small as to make it hard to instrument, and at large radii the strips would still be too large for good resolution in ϕ. For ϕ :

$$innerphi : \phi_i = \pi(i - \frac{1}{2})/192 \text{ radians } 1 \leq i \leq 96 \text{ i=strip number} \qquad (2.7)$$

$$outerphi : \phi_i = \pi(i - \frac{1}{2})/384 \text{ radians } 1 \leq i \leq 192 \qquad (2.8)$$

The EMLAC read out was further divided into two longitudinal sections along z, called the front section which was 22 layers deep ($\approx$ 10 radiation lengths), and the back section which was 44 layers deep ($\approx$ 20 radiation lengths). For the front section, each r_i concentric ring strip in an octant is wire ORed together to form a r_{fi} EMLAC channel for the front section. Each octant is wired out along its quadrant boundary. Similarly, for the back section the r_{bi} channels are formed by wire ORs of concentric strips of the same i$^{\text{th}}$ index. For a given inner radial i$^{\text{th}}$ strip the ϕ boards in the front section are wired ORed along the 40 cm hole in the middle of the LAC. For a given outer radial i$^{\text{th}}$ strip the ϕ boards in the front section are wired ORed along the outer radius of the LAC. The ϕ view is treated in the same way in the back section. The summed signals for the different regions of the EMLAC were then cabled away to the Faraday room above the LAC where they were connected to amplifiers (LACAMPS) to be used in generating LAC triggers, and being latched for read out. There were a total of 6272 channels

to read out of LAC for a data event. Each quadrant, front and back section, of the LAC can be thought of as four views: left and right r (octants), and inner and outer ϕ.

Splitting the EMLAC read out in front and back sections was done so that the ratio of the energy collected in the front section could be compared to the total energy measured in both front and back. This defines the ratio "efront over etotal", $\frac{E_{front}}{E_{total}}$. This is used to discriminate against hadrons that may start showering in the back section. Without this feature, one could not distinguish if a shower came from a photon (or electron) or a hadron starting to shower in the back of the LAC. More importantly, by dividing the LAC into a front and a back section, if two photons land close together on the face of the LAC, then the reconstruction software can split them apart easily since in the front section they will be separated before the showers coalesce in the back section. Without this division, the showers would coalesce and be impossible to separate in the offline analysis.

The r strips focusing in on the targets is another important feature of the EMLAC. The reasoning behind this design is what is defined as directionality, ϵ. Neutral photons that are produced in the targets will hit the LAC at some angle θ. The photon and subsequent shower will pass though the same r_i strip index through each layer of r boards. Thus, its shower will be focused in r, and centered on a few r EMLAC channels. Also, if a particle such as a stray muon were traveling parallel to the beam axis, it would intersect different indexed r strips and would have a non-zero directionality. Directionality can be used as a variable in offline analysis to cut fake photons caused by muons. Refer to figure 2.9.

2.5.2 LAC Cryostat

In the previous section the engineering and physics principles of the LAC were discussed. Now the engineering of how the LAC was actually supported externally, and the liquid argon provided is discussed.

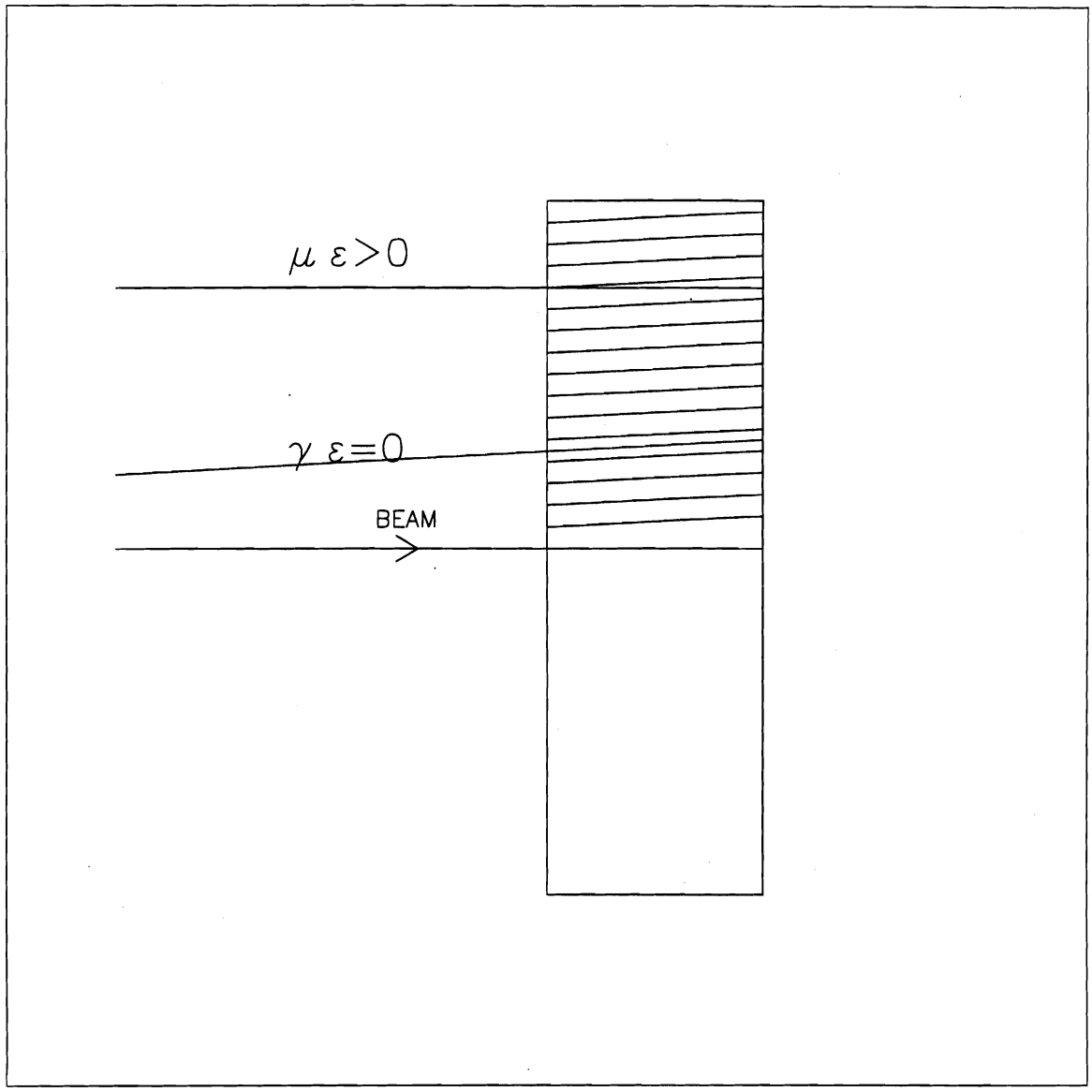

Figure 2.9: In this figure it is seen how the r boards focus on the target 9 m upstream. A photon coming from the target will be in focus and have directionality of ϵ=0. A beam halo muon will have $\epsilon > 0$, and thus be cut out and not be mistaken as a γ.

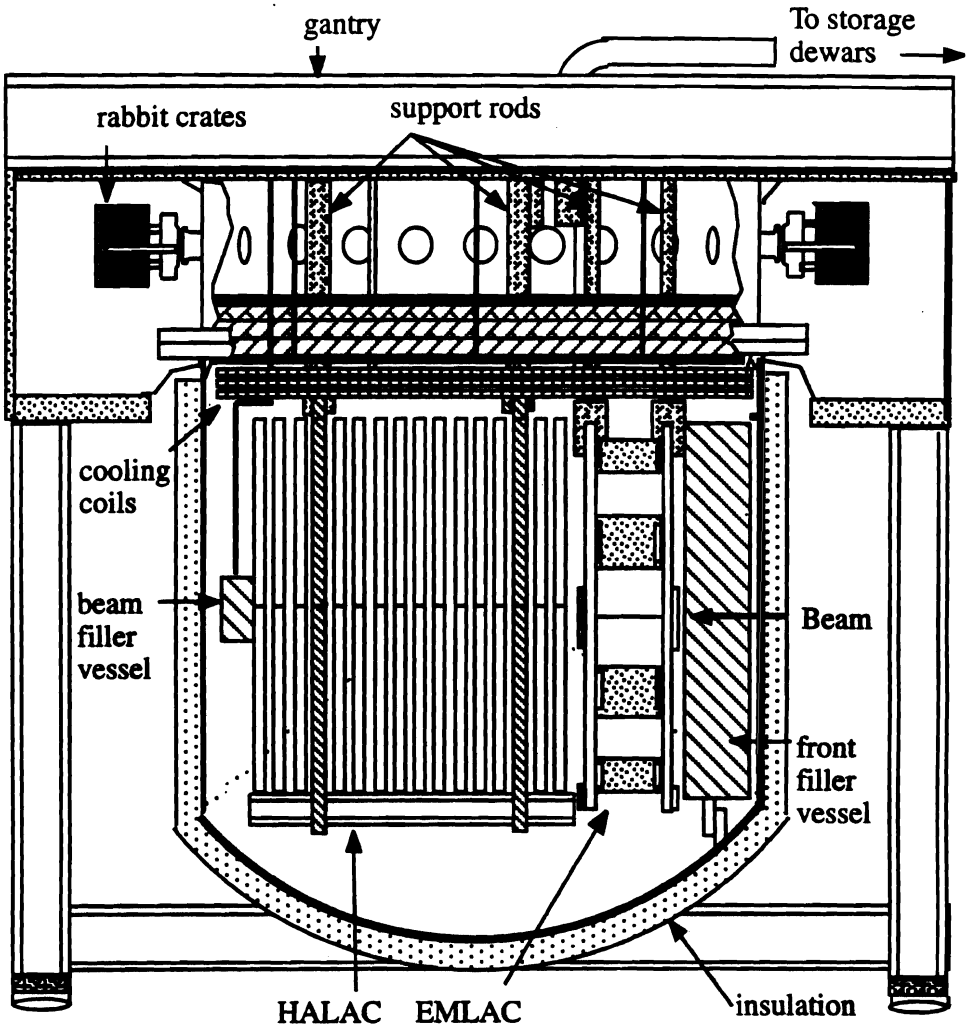

Figure 2.10: The LAC gantry that supports the lead plates, and anode boards that are immersed in liquid argon and sealed inside a cylindrical cryostat that connects to the upper portion of the LAC.

The LAC (both EMLAC and HLAC) was suspended in a large stainless steel cylindrical cryostat, supported by a steel I beam gantry as shown in figure 2.5.2. The gantry hung from a set of rails such that it could be moved in the x direction transverse to the beam. This was done so that in a low intensity test beam, with the magnetic field turned off in the tracking system, the LAC could be incrementally swept across the beam for calibration purposes. The top half or "cap" of the cryostat was built from mild stainless steel 17 feet in diameter and 6 feet tall. Eight steel rods passed through hermetic holes in the cap and were fastened to the rigid gantry. These eight rods held the LAC inside its cryostat. There were 30 access ports for high voltage cables, signal cables, and temperature monitoring devices to be passed to and from the LAC sealed up inside the cryostat. The lower half was made from stainless steel 17 feet in diameter, 21 feet tall, and 1.6 cm thick wall. The bottom was rounded. At the point where the beam ($\approx$ 10% interacts with the targets so 90% goes through) hits the cryostat the thickness of the wall was reduced to 1.6 mm in an area of 5 cm, decreasing the probability of the beam interacting with the cryostat wall that could cause particles to scatter all through the LAC. The whole thing was then wrapped in fiberglass and polyurethane foam insulation.

Ideally, the photon showers should start in LAC, but because of the material that made up the walls of the cryostat, photons and electrons could start showering before they hit the lead sheets of the LAC inside the cryostat. Since the cryostat is a cylinder with its axis vertical, and the LAC is a cylinder with its axis horizontal, then there is a gap between the face of the LAC and the cryostat as shown in figure 2.5.2. Photons could start showering in this gap if it were filled with liquid argon. To reduce the probability of this happening, the space between the front of the LAC and cryostat was filled with a filler material of Rohacell foam to exclude liquid argon from the gap. Rohacell has a high radiation length($\approx 500cm$ and a density of $0.07gm/cm^3$) so showers will most likely not start forming here, but

wait until the photons hit the dense lead sheets that make up the high voltage cathodes of the LAC cells. To exclude liquid argon from the 40 X 70 cm cylindrical hole in the EMLAC, the hole was filled with a cylindrical excluder vessel of $\approx$ 40 cm diameter 71 cm long, and had 3.2 mm thick walls. The excluder vessel was filled with pressurized helium gas because : a)helium is inert and not dense, b) the pressure kept the thin wall cylinder from collapsing under the weight of the liquid argon. This would allow the beam that did not interact to pass through the calorimeter with the minimal amount of scattering, and thus creating excess noise in the calorimeter. The front end of this vessel facing the beam was 1.6 mm thick.

As mentioned in preceding paragraphs, there were thirty port holes for cables to pass through the cryostat. These cables carried the analog signal from the LAC channels and the bias voltages for the LAC lead sheets. The crates where the DA modules were operated from, and the high voltage power supplies were attached directly to the cryostat cap. The whole cap was surrounded by grounded galvanized sheet metal walls to make a Faraday room. This would keep out stray electromagnetic contamination from the outside world that would introduce extra noise in the read out electronics. The stainless steel cryostat of LAC shielded it from outside interference. Cables and other electronics act as antennas for electromagnetic radiation; therefore, by shielding the cables, and the room where connections are made reduces this added noise source. Signals passed to the outside world were done so optically to avoid noise and ground loops. Transformers isolated power lines.

The liquid argon was kept cold inside the cryostat by passing liquid nitrogen through refrigeration coils just above the surface of the liquid argon. There was about 17,000 gallons of liquid argon in the cryostat. The temperature was maintained by controlling the flow of liquid nitrogen. The heat dissipation of the cooling system is 30 KW. Argon purity in the LAC must be maintained in order for the calorimeter to keep a good response. Contaminants like liquid oxygen have a high

electron affinity, and thus affect the amount of signal collected. Argon purity was an important consideration when building the LAC. Materials had be chosen which would not contaminate liquid argon.

Since the Hadron calorimeter was not of use in this analysis it will not be discussed. The Forward calorimeter gives coverage at small angles in θ corresponding to a large rapidity Y, but was not used in this analysis either so it will not be discussed.

2.6 Data Acquisition

In this section the method used to extract analog signals from detector elements, digitize them, concatenate the hits from all detectors into a single event, and finally record the event into a data stream for future analysis will be discussed. This process is referred to as data acquisition (DA).

The DA code was designed to do the following 5 tasks.

- Amplifier readout and digitization
- Data buffering
- Data transfer to VAX
- LAC calibration
- Monitoring the spectrometer

These functions were designed to use the accelerator cycle to do the readout efficiently. During the 23 second beam spill, data was continuously read out and placed in the buffer; while during the 23 seconds during a spill and the 35 seconds after the spill the slower VAX could record the events.

Figure 2.11 shows a block diagram for the DA system. The host VAX ran a program called VAXONLINE [14] that ran as the master DA code. It consisted of 4 major processes that were menu driven:

- RUN CONTROL
- EVENT BUILDER
- OUTPUT MANAGER
- BUFFER MANAGER

The RUN CONTROL let the user control the DA process by letting the user download code to various individual DA controllers and start or stop the DA process. The EVENT BUILDER concatenated data from different detector elements together to form an event. The OUTPUT MANAGER wrote the events out to a data stream. When writing events out, two tape drives were utilized in such a way that events were alternately written to one tape drive or the other. I/O to tape is one of the slowest parts of the process so this method sped the writing of events to tape such that all the events in the buffer were written to tape before the next spill began. The BUFFER MANAGER would sample events from the event pool so that raw events may be looked at online to check if the spectrometer was operating smoothly, and if not, then the problem was investigated and fixed.

Events were written out into data streams called runs which contained anywhere from 10k events to a maximum of 65535 events. During normal accelerator operations, a run was started every two hours. Each run was contained on two 8 mm tape cartridges due to the dual tape drive writing of events from the event pool as mentioned above. Usually, every eight hours the DA was shut down and all crate modules cleared and DA programs uploaded again to their respective DA micro processors. This avoided inefficiencies in timing errors that might accumulate between the different micro processors reading out different elements of the spectrometer.

The central computer was a μVAX running the VAXONLINE software described above. Slave components to this system as shown in figure 2.11 consisted of the following:

- FASTBUS. Readout system for LAC and STRAWS.
- PDP-11 NEU. This minicomputer controlled CAMAC crate processors which read out SSD's, PWCs, and the Trigger.
- PDP-11 ROCH. This reads out FCAL

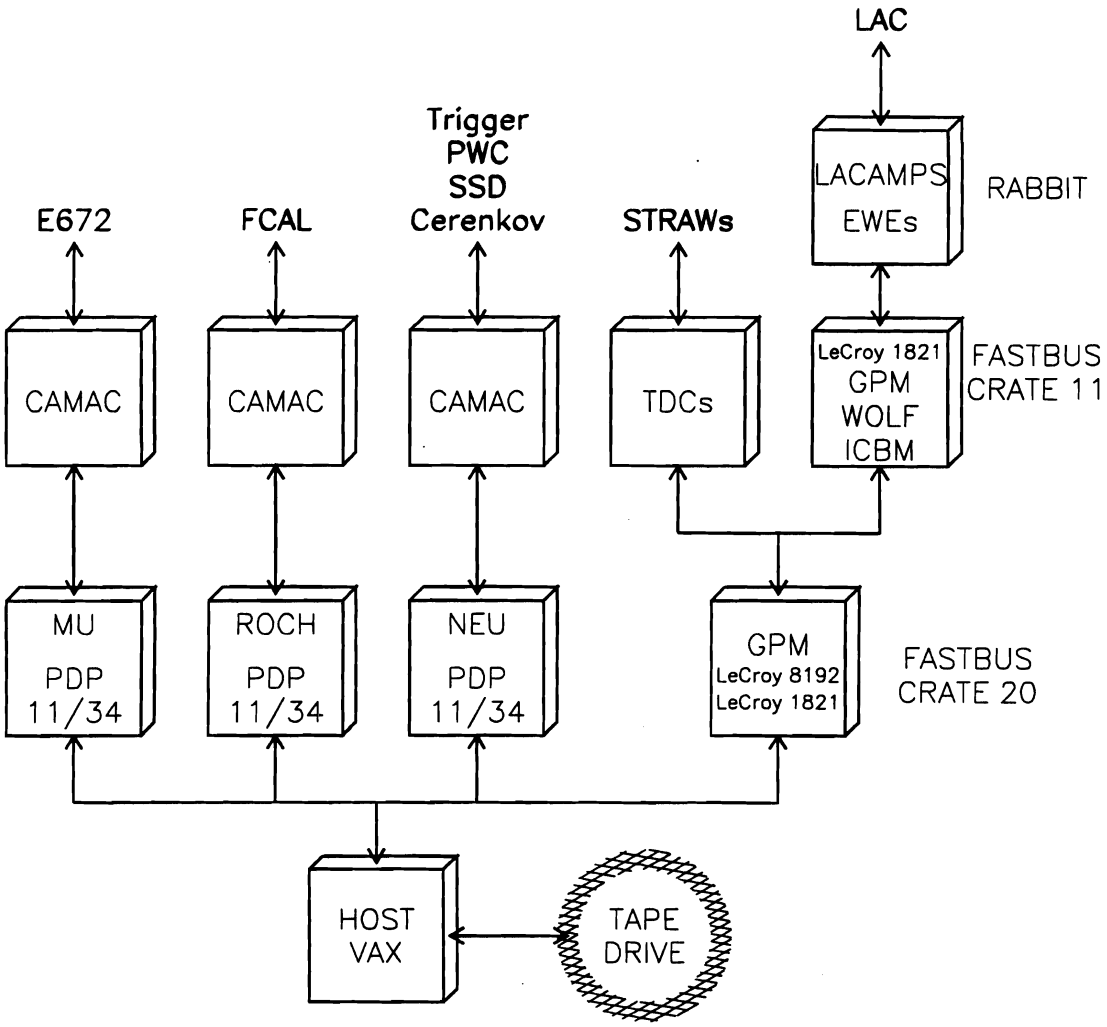

Figure 2.11: A flow chart of the E706 DA system.

- PDP-11 MU. This read out the E672 muon chambers.

2.7 LAC Readout

In this thesis the LAC was a major component so the read out of the LAC will be described.

The major components of the LAC DA were

- RABBIT system. RABBIT (Redundant Analog Bus Based Information Transfer) was the protocol used to interface the DA with the LAC. The following boards inserted in the RABBIT crate did this task.
  - LACAMPS. Amplified and integrated charge collected in LAC channels.
  - EWEs . Digitized the LAC data
  - BAT cards. Triggered the LACAMPS
- FASTBUS CRATE 11 Controlled the DA process in the RABBITS crates. The Following modules inserted in crate 11 were responsible for this task.
  - LeCroy 8121 FASTBUS crate controller
  - Struck GPM (General Purpose Master). Controlled the ICBMs, and data flow from the RABBIT crates, and CRATE 20.
  - WOLF. Interface between EWE(RABBIT) and ICBM (FASTBUS)
  - ICBM. Intelligent Control and Buffer Manager. A digital signal processor (DSP) for FASTBUS. ICBMs readout the LACAMPS.
- FASTBUS CRATE 20. Crate 20 buffered data and concatenated STRAW and LAC data.
  - LeCroy 8121 FASTBUS crate controller
  - GPM. Handled the data flow into crate 20 and built events to be transferred to the host VAX

– LeCroy 1892 Memory Module. Data was buffered here.

RABBIT System

The RABBIT system was the interface between the LAC and the DA. The RABBIT crate (Redundant Analog Bus Based Information Transfer) protocol is one where the back plane of the crate has two redundant busses for analog and digital data (such as pulse height and channel number data for a hit). There were 28 such crates in the Faraday room above the LAC (see figure 2.5.2) The following modules inserted into the slots of the RABBITS crates were responsible for collecting data from the LAC channels.

- LACAMP cards. These cards had charge sensitive amplifiers which integrated charge on sample and hold capacitors for the R and ϕ channels of the LAC. The integrated charge could then be latched on the capacitor, and its voltage digitized as data. Each card had 16 channels of amplifiers in addition to 8 channels of Time-to-Voltage Converters (TVC). The TVC information provided time of gamma hits so that offline it could be decided if gammas belonged to a given event or not if the timing was in coincidence with a given event.

- EWE Module. There were two EWEs in each RABBIT crate. Under control of the ICBMs in crate 11, the EWEs digitized the data presented on the backplane of the RABBIT crate as the ICBMs in crate 11 strobed the LACAMPS data onto the backplane. The ICBMs in crate 11 would then read the digitized data into their own memory, and then strobe another LAC channel until all channels were read out.

- BAT card. When there was a trigger, the GPM in crate 11 sent a signal to the Before and After timing module in each RABBIT crate. These modules

sent a signal to the LACAMPS to latch the data collected on the sample and hold capacitors.

CRATE 11

The modules in FASTBUS CRATE 11 controlled the DA boards in the RABBIT crates.

- The LeCroy 1821 is the FASTBUS crate controller that had its own sequencer that executed microcode to control the other modules in the FASTBUS crate. The microcode was downloaded to it via VAXONLINE running on the VAX, and once running, the 1821 was an independent free running data acquisition processor.

- GPM. The Struck GPM (General Purpose Master) is a FASTBUS board that has a Motorola 68000 microprocessor with 32 Kb of cache. Programs written for it could be written in C or assembler, and downloaded to it via VAXONLINE. This module was controlled by signals generated in the 1821, and it actually controlled the other LAC DA boards such at the ICBMs, and issued commands to modules in the RABBIT crates. This module handled all of the decision making and error handling for the LAC DA.

- WOLF. The purpose of the WOLF card was such that signals from the two different protocols of RABBIT and FASTBUS could be passed to each other.

- ICBM. The ICBM (Intelligent Control and Buffer Manager) was a board designed at E706 using the Motorola DSP56001 Digital Signal processor (DSP) around a FASTBUS protocol. Fourteen ICBMs read out the 28 RABBIT crates, and one ICBM reads out the TVC information. Each ICBM was responsible for 640 channels of LAC data. The ICBMs strobed the LACAMPS, and issued the commands to EWEs in the RABBIT crates to digitize a LAC

channel's data. The digitized data was then transferred into the ICBM's memory buffer.

CRATE 20

The purpose of crate 20 was to buffer the data in crate 11 until the slower host VAX and data transfer to tape was ready to accept more data. Data in crate 11 was transferred to crate 20 where the data was stored in the LeCroy 1892 memory modules. After crate 11 transferred its data to crate 20 it was free to acquire more data, while crate 20 processed the event and passed it on to the slower host VAX system. This parallelism provided a much higher throughput than if crate 11 were readout directly by the VAX.

The modules responsible for the crate 20's buffering role:

- LeCroy 1821. The host VAX communicated to the FASTBUS system via this card. When the VAX was ready to receive data it came bussed through this card to the VAX event pool.

- LeCroy 1892. The LeCroy 1892 is just a memory board addressed through the back plane with a first in/first out (FIFO) memory stack design. The 1892s were daisy chained together so that the memory could be addressed as if it were one long contiguous linear buffer. Each STRAW chamber had its own 1892. The GPM in crate 11 strobed data in these memory locations.

- GPM. The GPM in crate 20 managed the data flow coming in and out of crate 20. It concatenated the events from the STRAWs and LAC, and verified that event numbers matched. It attached a header to the event. Then when the host VAX was ready, transferred the event to it where the host VAX would then concatenated this subevent with the other detector element's subevents to form a complete event.

2.7.1 CAMAC

The SSDs, PWCs, and triggers had their DA modules designed around the CAMAC standard, and inserted in CAMAC crates. Each CAMAC crate had a Jorway crate controller that took its instructions from the DEC PDP 11/34 which was labeled as NEU. These DA boards have the same function as do the LAC DA boards, and that is collect data, latch the data, and buffer the data for transmission to the VAX.

2.7.2 Readout Example

If a beam particle interacted with the targets and scattered hard, it could produce high p_t objects. If these objects are electrons or photons they can deposit energy in the cells of the EMLAC as described in the spectrometer chapter. The LACAMP cards have a fast out signal that can be used to determine a trigger as described in the spectrometer chapter. If a trigger condition was met, then a signal was sent to the GPM in crate 11 and the three PDPs to initiate a readout. The GPM in crate 11 then generated a signal to all 15 ICBMs to initiate a read out of the LACAMPs. A given ICBM would strobe the LACAMPs that it was controlling, and the voltage on the sample and hold capacitor was digitized by the EWE in the RABBIT crate as instructed by the ICBM. Then the ICBM would strobe the digitized data in the EWE to a memory location into the ICBM itself. This process was repeated until all channels on all LACAMP boards were exhausted. After the readout, the ICBM would generate a done signal so that GPM on crate 11 could transfer the data from the ICBMs to the 1892s in crate 20. This transfer was started only after all ICBMs had generated a done signal that was "ANDED" together. After the trigger signal, but before the transfer of data to crate 20, the GPM issues a busy signal so that any incoming trigger will have to wait to be serviced.

The GPM in crate 20 polled the memory location in the 1892s looking for new incoming events. If a new event was there, it proceeded to concatenate the data

from the 8192 for the LAC DATA, and the 8192 from the STRAWs ,where the data from the STRAWS was placed, into a single subevent. Meanwhile, the CAMACs through the PDP NEU are building the subevents from the SSDs, PWCs, trigger, and E672. When the host VAX is ready it tells the FASTBUS 1821 controller to start transferring data from crate 20 to the host VAX for final event building. The 1821 shipped the data to the VAX via the 1821 personality card in 4 kb chunks onto the VAX event pool.

Chapter 3

EVENT RECONSTRUCTION

After the raw data is read out from the spectrometer and written to tape, it is then time to reconstruct the physics that happened in these events from the hits and energies recorded in the detectors various elements. This is event reconstruction. The output of event reconstruction is then written to a data summary tape (DST).

The reconstruction code takes raw data events from the detector, processes it, and turns it into useful physics variables (i.e. energies, positions, momenta) for each event. The processed events are written out on an event-by-event basis on to the DST stream. The DST events are then later read in by the user's analysis code, and physics analysis performed on them such as cross section calculations. The reconstructor also determines the value of certain quality variables (such as factors related to the quality of reconstructed values, trigger determination, etc.) so that the user can make quality cuts on the events. The trigger type is also read from the raw data, and written to the DST stream so that the user can select a sample to study. All the information available in the DST was written in a document called DST.DOC [15].

The off line FORTRAN 77 code that did the reconstruction was called MAGIC. During its development MAGIC evolved through ≈ 68 versions. To maintain this monster code, the code was modularized, and put together using the CERN code management system PATCHY [16]. In PATCHY one writes FORTRAN code in what are called card files with *.car extensions in the routine names. The advantage

of using PATCHY is that several groups may be developing different pieces of code for one large FORTRAN project so when it is time to compile the code, the CERN embedded command YPATCHY builds a single FORTRAN file from several *.car sources. PATCHY reads from an instruction file called a cradle that has a *.cra extension, and this cradle tells which *.car files are to be read in and written out into one large FORTRAN file. The FORTRAN file generated from the execution of PATCHY is then compiled and linked in the usual way. In the UNIX environment the utility *make*, updates the target FORTRAN file by checking the *.car files as dependencies for updating. If any one of *.car files is updated compared to the last created FORTRAN file, then YPATCHY is executed on the cradle that will build the FORTRAN code from the *.car files.

In the PATCHY system, a large chunk of code is called a PATCH, with subsequent routines labeled as DECKS. In FORTRAN one can handle common blocks that occur throughout the code with "include". PATCHY achieves this through use of what is call +SEQ,*. and +CDE,*. statements placed in the code at the car file level. At the top of the card file one can declare a set of variables, and their common blocks in +SEQ,NAME., where SEQ refers to the block as a sequence. An example of this is

```
+SEQ,ELOSS
   REAL ELOSS,THETA,PHI
   COMMON/ELOSS/ELOSS,THETA,PHI
```

Then, in any other routines where one wants to use these variables, one would type +CDE,ELOSS.. This is in place of an "include" file, and when PATCHY runs on the card files, it writes out the variables and common blocks defined in the SEQ into the FORTRAN output file. This has THE advantage that if one is using CDE from other sources, one can actually see what is defined in them by looking at the generated output FORTRAN code where they CDEs have been expanded into commons. PATCHY also has "if def" switches which makes maintaining code

on several different platforms easy. In the cradle one would put a command line

+USE,SUN.

So, in car files, if there is machine dependent code that is unique to a SUN©, for instance, but the same for other machines then, car file it would look like

```
+IF,SUN.
   OPEN(UNIT=11,FILE='SUN.OUT',STATUS='UNKNOWN')
+ELSE.
   OPEN(UNIT=11,FILE='ANYTHINGELSE.OUT',STATUS='OLD')
+SELF.
```

In this way, several parallel versions of code on different machines do not have to be maintained, instead just one set of car files. Then on each different machine one would specify the machine type in the cradle. For FORTRAN on UNIX systems this is analogous to maintaining code by taking advantage of the C language preprocessor or cpp.

Another facet of the software development was the usage of the ZEBRA memory management system from CERN [17]. The amount of data from each event will be different; thus, ZEBRA was used because it provides dynamic memory in FORTRAN. ZEBRA was used in the DA, MAGIC, and DST software. In ZEBRA, data is placed in memory banks referenced by pointers just as in the C language. In the memory banks, data is stored in a structure that is defined by the user. In using ZEBRA the user allocates memory using routines provided by ZEBRA (for C and Fortran users this would similar to a "malloc"). These banks are accessed through the FZIN and FZOUT FORTRAN routines provided by ZEBRA. The big advantage to ZEBRA is that it has the capability to write out the data banks in a compact binary exchange format to disk or tape. This binary exchange format is a machine independent structure such that the data can be read from any computer that has ZEBRA routines available to it.

In MAGIC, each different detector system had its own reconstructor that was

made to be independent of all other reconstructors. These were:

- DLREC, Discrete Logic Reconstructer. Trigger and Cherenkov information reconstructor.
- PLREC, Planes Logic Reconstructor. The digital hit information on PWCs, STRAWs, SSDs reconstructed to form charged particle tracks.
- EMREC, ElectroMagnetic shower Reconstructor. Reconstructed energies and positions of photons and electrons that hit the EMLAC.
- FCREC, Forward Calorimeter Reconstructor.
- HCREC, Hadronic Calorimeter Reconstructor. Reconstructs hits in the hadron section of the LAC.
- MUREC, This reconstructed Muons from the E762 tracking system.

Each of these reconstructors were maintained in their own card file, could be built independently, and run individually, or all together for total reconstruction of the data. In building the code, a card file called MAGIC provided the main program from which the rest of the reconstructors could be called if requested. Each reconstructor was built with PATCHY from its own makefile, and the generated FORTRAN code split into routines using fcasplit (another CERN product more powerful that just fsplit in that it simultaneously splits large files with a mix of FORTRAN, C, and assembler codes), compiled and archived away into the magic.a library. So when one wanted to build the reconstructor one would get a copy of the main routine magic and link it with the magic.a library. By maintaining the code in this fashion, if one reconstructor was changed it could be recompiled, and the new code generated objects would replace the contents of the old code in the library without recompiling all the other reconstructors. More importantly, by insisting that each reconstructor be independent of the other reconstructors, then

changes in one reconstructor would not have unknown consequences in another reconstructor. Also, in debugging it saves time if one is just interested in the output of one particular reconstructor, then time would not be wasted in reconstructors that were not of interest.

In running MAGIC there were two format free input files: the first one which specified the LOGICAL name of a switch and if it was turned on or not by a TRUE or FALSE statement; the second contained constants such as thresholds and cuts used in the different reconstructors. Each reconstructor and unpacker had its own switch. So if one were reconstructing raw data, one would switch on the unpacker and reconstructor that one was interested in with a TRUE statement, and the rest to FALSE. By default, they were all turned on for full blown reconstruction.

The unpacker prepared raw data for reconstruction by turning tracking hits into positions, and hits in the EMLAC channels into energies in those channels. If the input data was Monte Carlo data, then the unpacker was not used, and just the reconstructor was turned on. Monte Carlo data went through a Monte Carlo pre-processor first which incorporated detector effects into the simulated detector. This is discussed in more detail in the analysis chapter 4.

Constants for the different detector systems that changed on a run-by-run basis were handled by MAGIC itself. For instance, the alignment of the STRAW chambers changed on a run-by-run basis due to mechanical instabilities; thus, the alignment constants had to be recalculated for every run. On the VAX there existed a set of files which contained these and many other constants for each run. When MAGIC was running, it first determined the run number of the events it would reconstruct from the header stamped on the raw data run by the DA software. Magic then formed a socket with the VAX, and retrieved the constants. On the host VAX a piece of code was running that completed the socket and interfaced the outside world with the run constants.

In doing the main reconstruction, millions of events had to be processed and

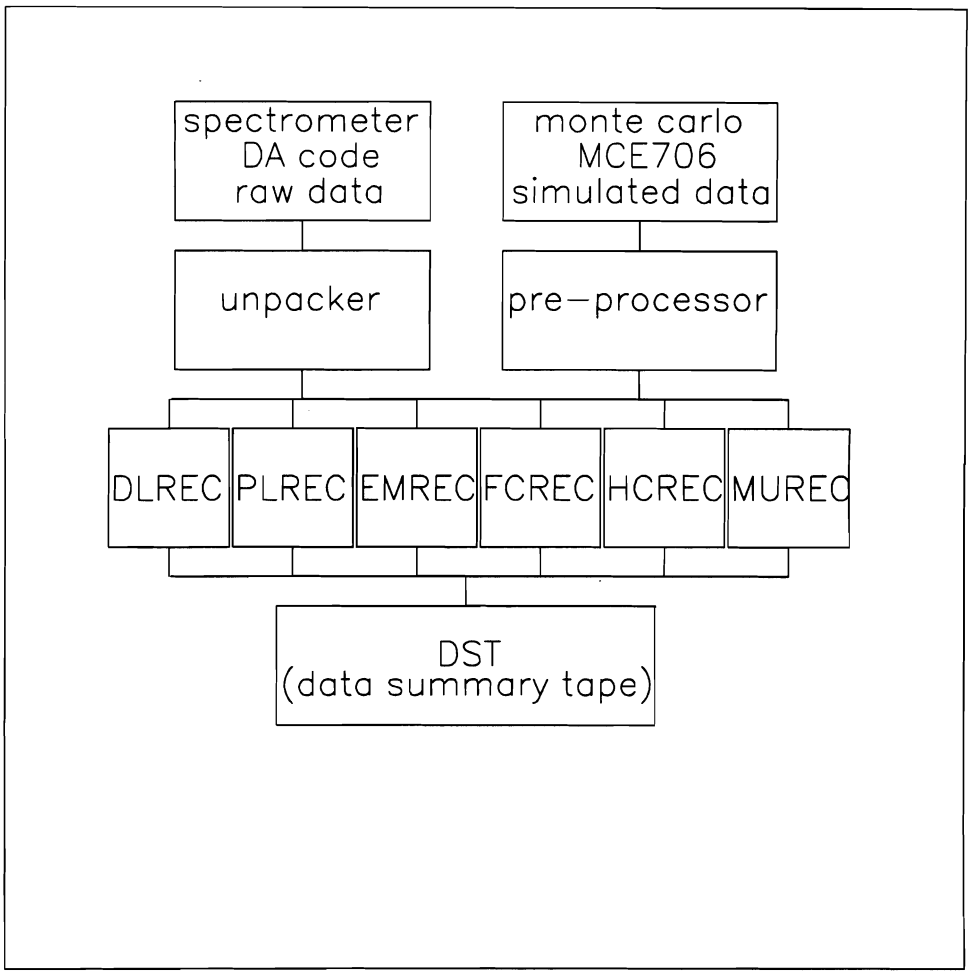

Figure 3.1: The flow chart of the MAGIC event reconstructor. This code reconstructs data by taking raw data hits, unpacks them into energies and positions, and then parses them out to the reconstructors to be fitted into useful physics variables. These variables are then written out to the DST stream. The Monte Carlo data goes through the preprocessor to incorporate detector effects (channels noises, inefficiencies etc.) in the data, and then parses the event out to the reconstructors.

turned into DSTs for the group's analysis effort. To do this in a timely fashion MAGIC was run on Silicon Graphics Indigo (SGI) farms. In the farm mode, one SGI handled I/O (input output), and 10 worker SGIs actually processed the events. This is a fast configuration because one node is totally dedicated to I/O, and 10 nodes totally dedicated to number crunching. The master I/O node distributed events to the worker nodes, and when a worker node completed it's event, the I/O node took the event and wrote it to tape and handed out another event read from a raw data tape to the worker node. In processing, E706 used three farms in this configuration. It took about a year of processing to process all of the 90-91 data.

To speed up the processing, months were spent studying various level of FORTRAN optimization. Each routine in magic ($\approx$ 700 routines, not counting calls to cernlib,ZEBRA, etc) was optimized to the point were it's accuracy would begin to be affected. The optimization was then stepped back for the fastest yet most accurate computing speed. To insure accuracy "lint" was run on magic to check for potential problems. The code was also compiled with the option "check bounds". Also, magic was originally developed on they VAX, so after it was ported over to the SGI, cross checks against the output on both systems were performed, the results were identical.

3.1 Tracking System Reconstruction

The charged-track reconstruction code is called PLREC for PLanes REConstructer. PLREC takes hits from the upstream and downstream tracking chambers (SSDs, PWCS and STRAWs), and reconstructs tracks from the hits detected in these chambers. It also finds the position of the vertex of the event. The vertex is where the beam particle interacted with a target nucleon creating exotic particles which leave tracks in the detector which point back to their origin of creation.

3.1.1 Downstream Tracking

Downstream of the magnet there were 4 proportional wire chambers (PWCs) that had 4 planes of wires per chamber for x, y, u, and v views. The x, y views are orthogonal to each other, and the u, v view are orthogonal to each other but rotated by 53 deg to the x, y plane as shown in figure 2.6. The z position is given by the location in z where the module was placed. When a charged track passes through a module it will ionize the gas in the neighborhood around the sense wires where the electric field will cause the charge to drift to the sense wire, and its charge integrated. Thus, a hit will be recorded, and by knowing the wire number one can get an estimate of the x, y position and the z position by knowing which module was hit. A track going through all modules will have 4 hits per view, or 16 hits total. For a track at a large angle of incidence, a single track will light up many wires forming a cluster. To get the position the mean position of the cluster is used.

To find a track, hits in the first and third PWC planes are used as seed planes, and the second and fourth planes were used as search planes. All possible combinations of tracks are formed from hits in the seed planes and are looped over in each view x, y, u, and v. When a track is proposed between two hits in the first and third planes, the track is projected through the other planes to see if any hits landed within $\pm$ 1 wire spacing of the projected track. If two hits on the projected planes were found than this track was tagged as a 4 hit candidate. If only one hit was found then the track was tagged as a 3 hit candidate. Three hit candidates are likely because: a) hit efficiency of a plane, and b) acceptance, a track may have a large enough angle to leave the detector before it crosses the last plane. Of course, if no hits in the search planes were found that matched the projected track, then this track is obviously not a real track. Redundancy of the planes insures against fakes. Then the whole process is repeated a second time this time using the second and fourth planes as seed planes, and planes one and three as the search planes.

This is done as to not miss any three hit tracks, and to do a cross check of the first pass. Least squares fits were then applied to all track candidates getting slopes, intercepts, and χ^2 (the measure of the quality of the fit). The tracks are now parameterized as $x(z)$, and $y(z)$.

The next step is to link up tracks in the x and y views to form three dimensional parametric space tracks. If one looks at hits in just x and tries to match them up with hits in y, then, in instances of many tracks, there will be an ambiguity in which x hits correspond to the correct y hits. This is where the u v views come into use. A three dimensional x, y, z space track is proposed by using the coordinates from x, y views and z from the position of the planes. This space track is then projected through to the rotated u v planes to see if it projects to within $\pm$ 1.5 wires of hits in these planes. If not, then it is not the correct space track. This process is repeated for all possible x, y view track combinations. The space tracks are double checked by repeating the procedure, except this time using all possible u, v view track combinations and projecting the tracks to the x, y plane for hits within $\pm$ 1.5 wire spacing.

During the first pass, accepted space tracks had to be of high quality which means only 16, 15, 14, and 13 hit space tracks were accepted. The 16, 15, and 14 hit tracks had to have a $\chi^2/DOF < 3$. Space tracks with 13 hits had to have a $\chi^2/DOF < 2$.

Having found all the high quality tracks, PLREC marked the hits that were used in forming these tracks, and then redid the procedure on the hits that were left trying to find wide angle tracks that escaped the last tracking chambers. If any hits were left after this procedure, they would with high certainty, be uncorrelated to any track and could be considered as noise hits.

The STRAW tubes were now used to refine space track parameters. Hits in the STRAW tubes were matched to space tracks, the tracks were refit with the extra points that the STRAW tubes provided. The STRAWs have a resolution

of 100 microns as compare to 1 millimeter of the PWCs so by redoing the fit with greater weight on the points by the STRAWs tubes the resolution on space tracks was improved from 1.25 mm to 500 microns. This substantially improves the momentum resolution of charged tracks.

The alignment of the tracking system was refined in the offline analysis by adjusting the alignment parameter of the downstream tracking system to get the best track resolution.

3.1.2 Upstream Tracking

Downstream of the target, and upstream of the magnet there were 5 modules of SSDs. Each module consisted of a x, y view plane of silicon for a total 10 planes. Refer to the figure 2.2 in the spectrometer chapter. The SSDs are used to perform the upstream tracking (before the magnet) and vertex finding.

Finding upstream tracks is done in a manner similar to that of the downstream tracking where tracks are found in each view, and then matched to find three dimensional space tracks. The process first looks for high quality four and five hit tracks in both views, and makes space tracks out of these. Then it projects these tracks to the middle of the magnet, and projects the downstream stream found earlier to the middle of the magnet and tries to link the upstream and downstream tracks taking into the account the bending done by the magnetic field in the x view. To call a track linked between the upstream and downstream view, the two tracks had to point to same spatial area within 3.3 σ, where sigma is the combined resolution of the tracking system. After the initial linking, the upstream SSDs were checked for any three hit tracks that would link with any downstream tracks.

3.1.3 Vertex Finding

Using the found x y view tracks, the vertex position of the interaction of the beam particle with target nucleon can now be found. (See figure 3.2 for an example of an

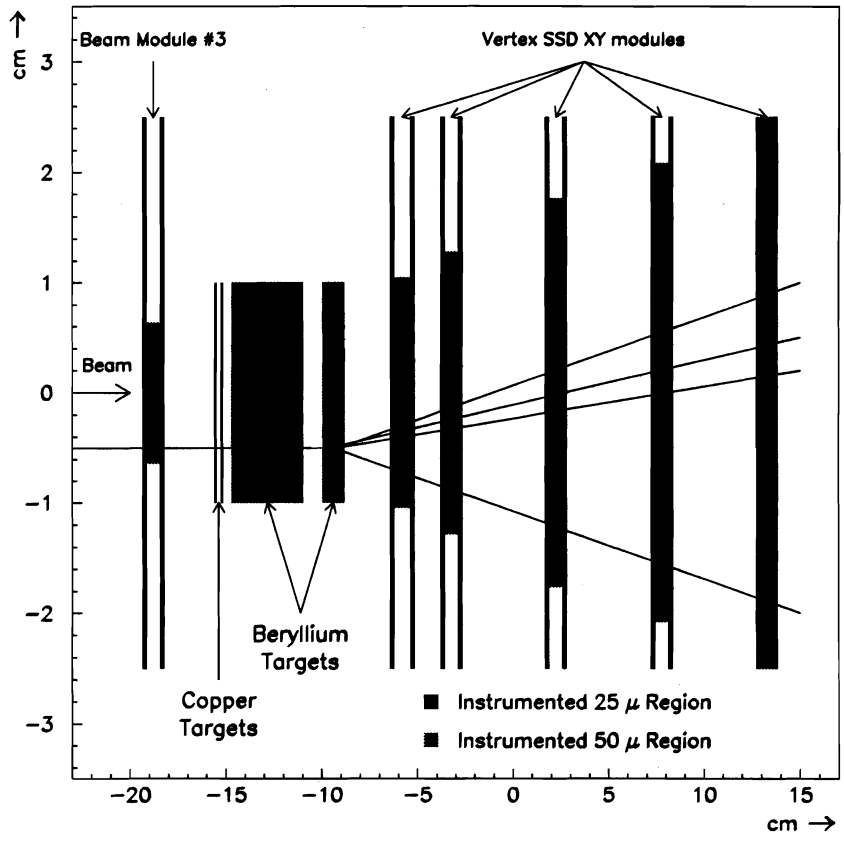

Figure 3.2: Hits in SSDs reconstructed as tracks.

event.) In each view the reconstructed tracks in the upstream SSDs should point to a common origin. To get a reliable vertex position at least three tracks in each view are required. If one just has two tracks with different slopes, then they will cross somewhere, but that does not mean that the intersection point is indeed a true vertex. In selecting tracks to find a vertex first the algorithm used four and five hit linked tracks. If not enough linked tracks were available, then four and five hit unlinked tracks were used. If still there were not enough tracks then no vertex was found.

To find a vertex the selected view tracks are projected in z back to where they all intersect. Of course they will not quite intersect because the tracking resolution will have lead to an imperfect determination of track parameters, so to get the best estimate of the true intersection point the algorithm minimizes the following defined χ^2:

$$\chi^2 = \sum_{i}^{numberoftracks} \frac{b_i^2}{\sigma_i^2} \tag{3.1}$$

Each view is handled separately and i runs over all tracks in a given view. The b_i is the impact parameter that i^{th} track has with the vertex position. (The impact parameter is the perpendicular distance of the track from the estimated vertex position.) The σ_i is the uncertainty in the projected i^{th} track. The vertex position in z is varied such that this quantity is minimized. After two independent z positions were found, one in each view, the z in one view was used to refit the z position found in the other view and vice a versa to see how well they agree. This was a cross check to make sure things were consistent. Finally, the final z position of the interaction point is now defined as vz, is taken as the weighted average of the z position in each view. The weight in each view being determined by the error in the proposed z position in each view. The vx, vy positions are obtained by putting the found vz back into the equations for the tracks in each view, and obtaining vx vy for their respective views.

Having found a vertex, tracks not used to form this primary vertex are then used

to find a possible second vertex. The secondary vertex may have come from either a secondary interaction, like a decay of a long lived particle from the primary vertex, or another beam particle causing another primary vertex (although this is a remote possibility due to the CLEAN INT trigger requirement in the trigger section). If a secondary vertex was found, then it was checked as to which vertex was further upstream. The most upstream vertex was always considered the primary vertex.

After the vertex was found, the linking of upstream and downstream tracks was redone with tracks originating from the vertex given more weight. After relinking, the charge and momentum of tracks could then be calculated and written out to ZEBRA data banks in the DST stream. The polarity of the charge(q assumed to be the charge of the electron) is deduced from the direction the particle was bent in the magnetic field. Momentum and the magnitude of the charge is determined from the amount of bending that occurred. This is determined from linked tracks in the upstream and downstream view. The bend angle is the difference in angle(θ_1). that the upstream track makes upon entering the magnet with the exit angle(θ_2) it makes upon leaving the magnet. This follows from the Lorentz force $\vec{F} = q\,\vec{v} \times \vec{B}$. The charge is calculated as:

$$q = \frac{\theta_1 - \theta_2}{|\theta_1 - \theta_2|} \times \frac{\vec{B}}{B} \tag{3.2}$$

This quantity is ± 1, and the term $\frac{B}{\vec{B}}$ is the polarity of the $\vec{B}$ field. Relationships for the momentum are as follows:

$$\sqrt{p_x^2 + p_z^2} = \frac{q|\vec{B}|L_o}{\sin(\theta_1) - \sin(\theta_2)} \tag{3.3}$$

$$p_x = p_z \tan(\theta_1) \tag{3.4}$$

$$p_y = p_z \tan(\theta_y) \tag{3.5}$$

The L_0 is the length in z of the magnetic field. The angle θ_y is the angle the track makes in the $y - z$ plane where no bending occurs. The angles θ_1 and θ_2 are the entrance and exit bending angles in the $x - z$ bending plane from the magnet as determined from linked upstream and downstream tracks.

3.1.4 Beam Tracking

There were three SSD modules with x, y planes upstream of the target used to find the track of the beam particle that caused the vertex. First, all three hit tracks in each view were found, then two hit tracks. The tracks in each view were projected into the target and the tracks coming closest to the vertex point were used, and formed space tracks for beam particles.

3.2 EMREC

The liquid Argon Calorimeter (LAC) was the primary tool used in this thesis since $\pi^0 s$ decay primarily electromagnetically into the two γ mode, and it was this mode that was studied. EMREC (Electromagnetic Calorimeter Reconstructor) took energy deposited in the electromagnetic section of the LAC (EMLAC), and reconstructed the energies(E), positions (r,ϕ), as well as the front to back ratio of energy, and other quality factors (such as directionality, χ^2 of shower shape fits, etc) used in the study of photons and electrons that showered in the EMLAC. See figure 3.3 for a picture of the hit distribution of gammas across the face of the LAC. The reconstructed energy distribution of photons is shown in 3.4

A simple description of EMREC follows: The LAC is a sampling calorimeter with alternating lead sheets, anode boards, and liquid argon that is 66 layers deep. The anodes are physically segmented and electrically connected in such a way that they form cells which can sample an electromagnetic shower caused by a photon or electron. These cells were then wire "ORed" to form EMLAC channels as described in the spectrometer chapter 2. These channels allow the energy collection to be localized so that individual photons can be identified and their positions extracted. The energy collected in these channels can be plotted as function of position (channel number) to give the shower shape. This shape is then fitted to a known function for shower shapes in the EMLAC. From this fit

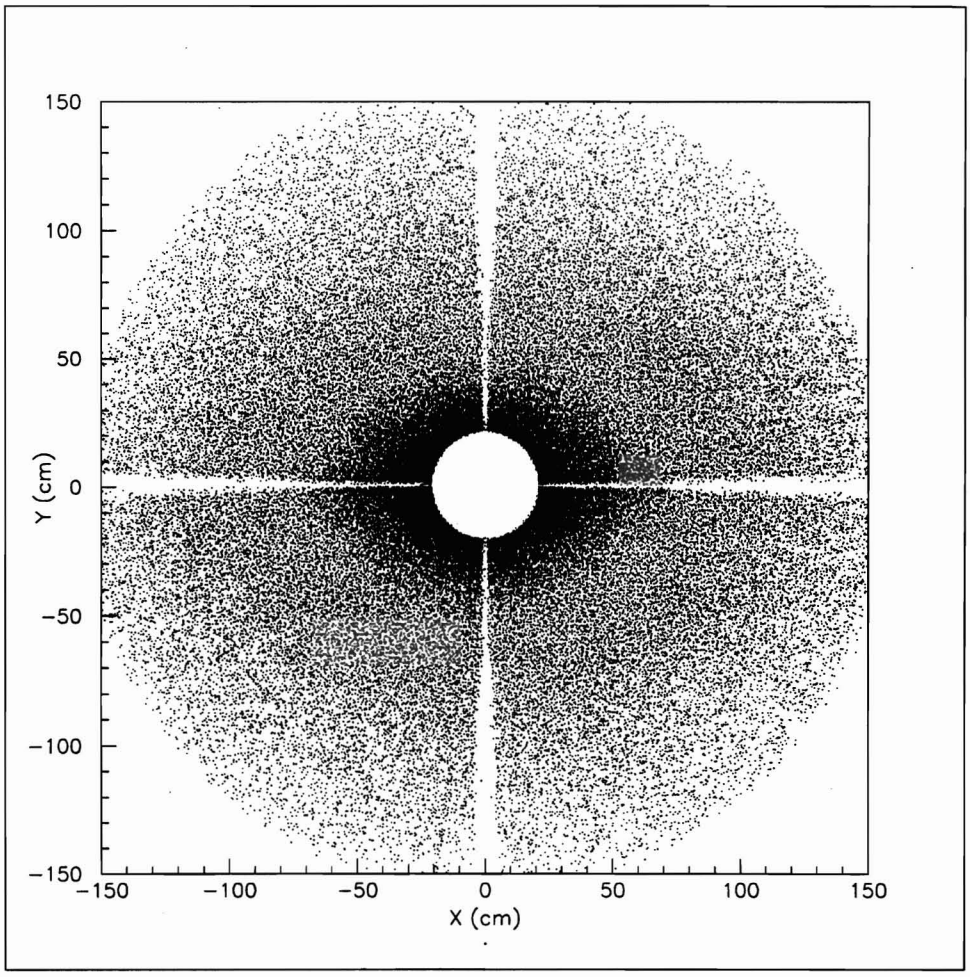

Figure 3.3: Reconstructed photon positions across the face of EMLAC. The dead quadrant boundaries show where the LAC is not instrumented. These regions are where the mechanical supports of the EMLAC quadrants are located and where connector strings carried out the charge collected on the R strips. The ϕ strips are read out on the inner and outer boundaries.

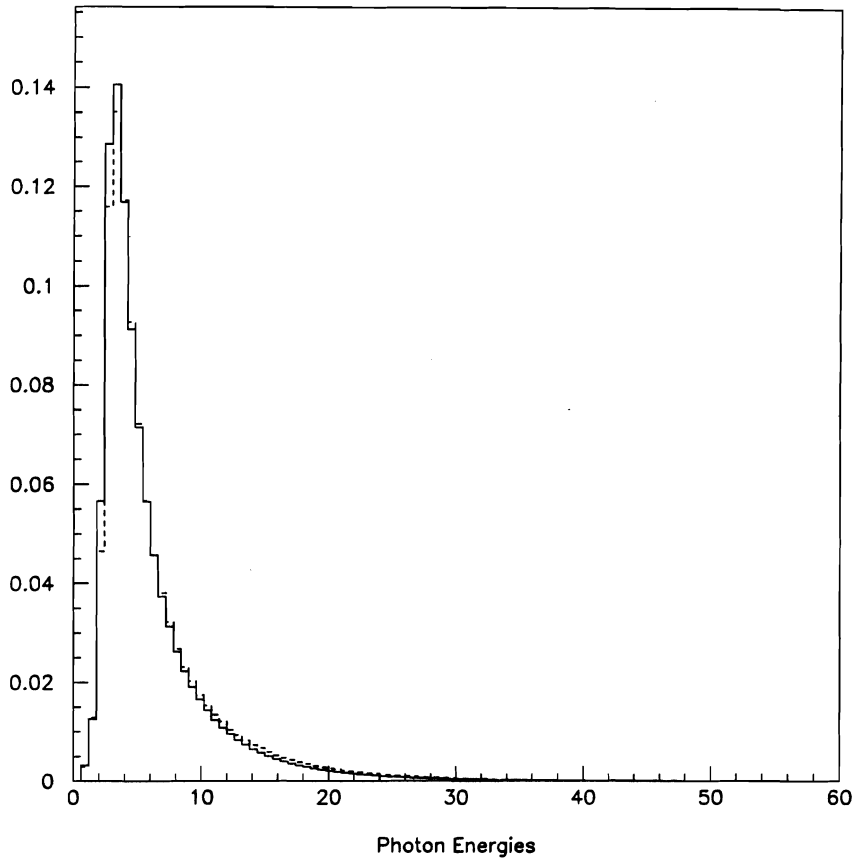

Figure 3.4: Reconstructed photon energies from the EMLAC. The superimposed curve is the Monte Carlo simulation. The two curves are area normalized to each other.

the energy and position of the photon are determined. The rest of the chapter is a more detailed description of the above process. Further discussion may also be found in [18].

3.2.1 Regions of the EMLAC

As mentioned earlier in the spectrometer chapter section on the LAC, the EMLAC consisted of a front and back section that were read out independently. This was done so that the ratio of energy deposited in the front, as compared to the total energy deposited in both front and back sections can be computed. This ratio is used to discriminate against hadrons that start to shower early in the EMLAC before they reach the Hadron LAC (HLAC). Hadrons have a low $\frac{E_{front}}{E_{total}}$ ratio since most their energy was deposited in the back section of the LAC. Refer to figure 3.5 for a plot of $\frac{E_{front}}{E_{total}}$. In this analysis a cut of $\frac{E_{front}}{E_{total}} > .2$was applied to the sample to cut down on the hadronic background (This cut is corrected for by Monte Carlo simulation as discussed in chapter 4). The events at one are either soft events that deposited all of their energy in front, or events that started showering early in LAC like in the cryostat or filler vessels.

The front and back sections were further divided into quadrants. Each quadrant was further divided into two sections called octants. Every other anode board had either r position read out strips that were physically concentric rings etched out on the board, or a ϕ position board that had radial strips etched out on the board as shown in figure 2.8. The radial r strips were concentric rings, but had gaps at quadrant boundaries. This is because quadrant support structures were located here, and the connector strings that carry away the charge collected in a EMLAC cell. These strips were electrically split at the center of each octant with one half being read out at one quadrant boundary, and the other half at its quadrant boundary. The ϕ boards were split between an inner and outer ϕ as discussed in the the spectrometer chapter. What this means from a software point of view is

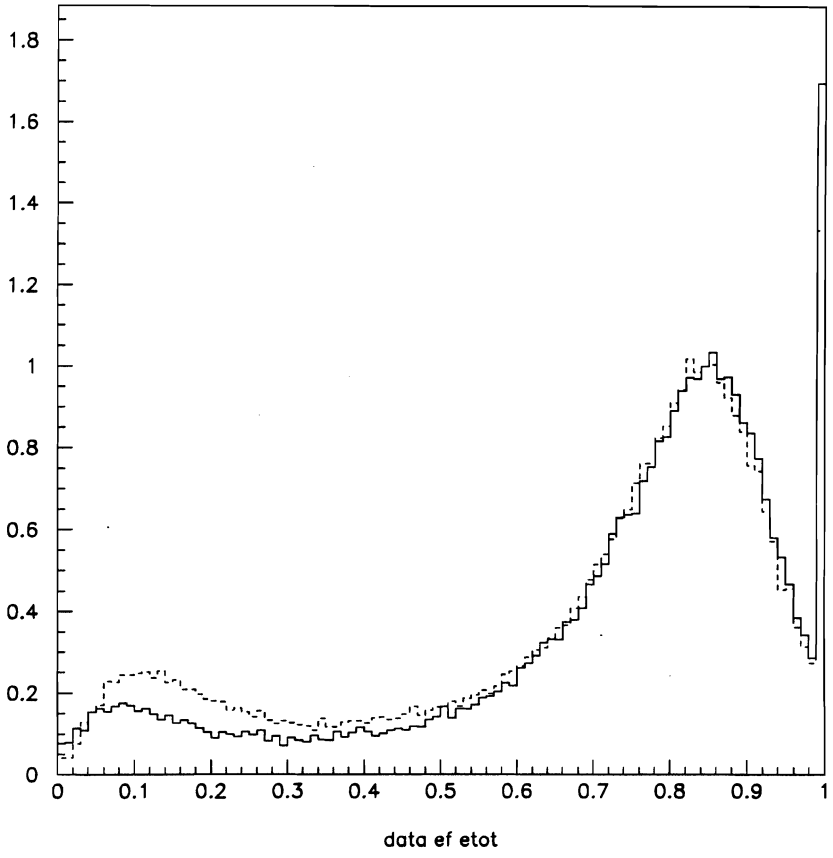

Figure 3.5: The ratio of energy deposited in the front of the LAC to the total Energy deposited in the LAC. The peak in at .8 is due to photons. The peak at .2 is due to hadrons. The peak at 1. is caused by soft photons.

that each quadrant, for the front and back sections, can be thought of as consisting of four views. A left, and right R view as created by the octant boundary, and inner an outer ϕ. Each of these views are at independently. Photons that land on boundaries are cut out in later analysis, because it is difficult to get a reliable energy fit from the partial showers that were collected.

3.3 Unpacking

The first task EMREC must do is to read in the raw data which is in the form of ADC counts which represents the integrated charge collected by the LACAMPS for each EMLAC channel. The energy on each channel i is calculated by:

$$E_i = A_{em} \times B_{em}(t) \times G_i \times (N_i - N_{0i}) \tag{3.6}$$

- A_{em} is the conversion factor of ADC counts to energy.
- $B_{em}(t)$ is the time dependent energy scale correction. The energy response of the LAC was found to depend on time.
- G_i is the gain correction in each channel due to the fact that each LACAMPs and LAC cells have intrinsically different gains.
- N_i is the number of ADC counts on the i^{th} channel.
- N_{0i} is the number of ADC counts estimated to be the pedestal the i^{th} channel.

A_{em} was determined from data. $B_{em}(t)$ was the scale correction to energy calculated by studying the mass of the π^0, as a function of time, and the position r, ϕ [13]. The G_i term is the correction for channel to channel variation calculated by looking at individual channels calculated during the calibration task of the DA. N_{0i} is the number of pedestal counts in a channel that was calculated by looking at the noise fluctuations in the LAC channel when no hits were present in the channel and getting the mean value of the noise. This was done by looking at

beam triggers for the entire run to get a good sample of noise on a cell. The N_i is simply the ADC counts read from the i^{th} channel for a given event.

After unpacking the raw data, but before the reconstruction, a EMREC routine FREDPED (after the author) was called to make final adjustments to the pedestal to correct for event by event variations in the pedestal.

3.3.1 Group and Peak Finding

After unpacking the next task is to find showers of a given event in the EMLAC. A group is a cluster of strips that contain energy from a shower. In searching for a group, the energies of strips in the front part of the calorimeter are added to their corresponding counterparts in the back. A group is defined as follows:

- There be at least 3 strips (2 for outer ϕ since the strips are larger there) with energies above 80 MeV. (95 for outer ϕ).
- The total group energy must be at least 600 MeV.
- The strip with the maximum energy must contain at least 300 MeV (350 for outer ϕ).

All possible combinations of adjacent LAC channels are looped over and searched to see if they match the criteria listed above. The size of the group was determined by how many strips could be added in the group before the next strip fell below threshold. If a group was found, then the group was stored in a ZEBRA data bank for later work.

Once all groups have been identified, then the search for peaks in a group is done. A peak is found by looking for changes in the slope of the energy profile. For groups with a single peak the process is easy. The group boundaries are defined by adjacent strips to the group going below threshold. These boundaries are defined as the valley strips. If the peak is singular, then there is a relatively smooth change in slopes to give a single peak. For overlapping showers there can be two or peaks

in one group. The peaks can separated by defining the valley as the strip with the lowest energy between the peaks. In some cases though the separation is more difficult because in the case of a low energy shower close to high energy shower, the low energy shower may just form a shoulder onto the shower shape of the high energy shower. Shoulders are found by looking at fluctuations in the logarithmic derivative of the shower shape. In this case the shoulder is checked to see if it is statistically significant compared to the expected shower shape of a single energetic shower (i.e. not a statistical fluctuation)

Once all peaks and valleys are found for the summed view, the front section is searched for peaks that were not found in the summed energy pass. This is done because the showers of low energy particles may totally be in the front section of the calorimeter, and by adding the back section strips in as in the summed view they may be lost in the noise from the summed view. If a peak candidate is found in the front view its significance is compared to a possible noise fluctuation using the formula :

$$\sigma^2 = (0.22)^2 + (0.16)^2 E + (0.01)^2 E^2 \tag{3.7}$$

The factor .22 is the base noise in the system. The 16% is the resolution of liquid argon and the $(0.16)^2 E$ is how this resolution changes as a function of E. Thus if the peak is $2.5 \times \sigma$, the peak is judged to be significant. The quadratic term is a small higher order correction.

After the groups and peaks are found in an event, fits are done to the groups to get the energies and positions of the photons. The shower shape can be parameterized as follows:

$$E(r_s) = P(r_s) E_{total} \tag{3.8}$$

The ordinate r_s is the distance from the centroid of the shower. $P(r_s)$ is the shower profile that expresses the fraction of E_{total} that is at distance r_s from the shower center. From Monte Carlo studies of single photon showers in the LAC, it was

determined that the shower shape could be parameterized as:

$$P_f(r_s) = \frac{1}{r_s}(f_1 e^{-f_2 r_s} + f_3 e^{-f_4 r_s} + f_5 e^{-f_6 r - s}) \tag{3.9}$$

for the front section for the EMLAC, and

$$P_b(r_s) = b_1 e^{-b_2 r_s} + b_3 e^{-b_4 r_s} + b_5 e^{-b_6 r_s} \tag{3.10}$$

for the back section of EMLAC. Both of these functions are normalized to unity and represent the expected fraction of energy deposited at r_s.

To do the fits, first the center of the shower must be estimated to calculate r_s. The first estimate is simply the centroid of the strip of the peak of the shower. This is then corrected by using an energy weighted averaging scheme of the neighboring strips to help interpolate where the true center of the shower is. Fits then will be performed to the shower shape. Once a fit with a minimal χ^2 is obtained, the center of the shower is varied to left and right of the proposed center to see if the χ^2 can be further minimized, and thus obtaining a better extrapolation of the centroid.

Energy fitting in the front section is considered first. To do the fit to the shower shape the following χ^2 is minimized.

$$\chi^2 = \sum_i \frac{1}{\sigma_i^2}(E_i - E_{fit} P_f(r_{s\,i}))^2 \tag{3.11}$$

The sum runs over all strips defined in the group. The factor E_i is the measured energy collected on the i^{th} strip. $P_f(r_{s\,i})$ is the expected fraction of energy deposition on the i^{th} strip and is equation 3.9. E_{fit} is the quantity that is sought, and it is this quantity that is varied to get the minimal χ^2. The σ_i^2 is the resolution for a given i^{th} strip for measuring E_i, and it is given by 3.7. Ideally, this sum should be around 1.0 taking into account normal statistical fluctuations.

To find the minimal χ^2, equation is 3.11 is minimized by taking its derivative respect to E_{fit} and setting it to zero.

$$2\sum_i \frac{1}{\sigma_i^2}(E_i - E_{fit} P_f(r_{s\,i}))P_f(r_{s\,i}) \;\; = 0 \tag{3.12}$$

so then E_{fit} is trivially obtained:

$$E_{fit} = \frac{\sum_i \frac{1}{\sigma_i^2} E_i P_f(r_{s\,i})}{\sum_i \frac{1}{\sigma_i^2} P_f(r_{s\,i})^2} \tag{3.13}$$

If the χ^2 was less than 5.0 the fit energy was deemed acceptable, and stored in the GAMMA banks as the energy for a photon candidate.

If the fit was not good the energy was taken as the sum of the E_i from each channel in the group plus a tail correction. The tail energy is estimated from the fits as:

$$E_{tail} = E_{fit}(1 - \sum_i P_f(r_{s\,i})) \tag{3.14}$$

This equation simply states that the energy left over from the total fit energy minus the fit energy from the group region is the energy in the tails. Then the energy for these photons is estimated to be the measured strip energies plus a tail correction or

$$E_{sum} = \sum_i E_i + E_{tail} \tag{3.15}$$

This quantity is then stored in the GAMMA banks as the energy for photons whose fit $\chi_{dof} > 5$.

For overlapping showers EMREC must resolve the multiple peaks, and estimate how much energy each shower contributes into the overlapping group. The function to be minimized is

$$\chi^2 = \sum_i (E_i - \sum_k E_{k\,fit} P_k(r_{s\,i}))^2 \tag{3.16}$$

Where the sum is over all i strips, and all k showers in i strips. Differentiating with respect to fit energies $E_{l\,fit}$ (l is a dummy index)

$$\sum_i (E_i - \sum_k E_{k\,fit} P_k(r_{s\,i}))\ \ \frac{\partial}{\partial E_{l\,fit}} \sum_k E_{k\,fit} P_k(r_{s\,i}) = 0 \tag{3.17}$$

$$\sum_i (E_i - \sum_k E_{k\,fit} P_k(r_{s\,i}))\ \ \sum_k P_k(r_{s\,i}) \delta(k-l) = 0 \tag{3.18}$$

$$\sum_i (E_i - \sum_k E_{k\,fit} P_k(r_{s\,i}))\ \ P_l(r_{s\,i}) = 0 \tag{3.19}$$

Rearranging equation 3.19

$$\sum_i \sum_k E_{k\,fit} P_k(r_{s\,i}) P_l(r_{s\,i}) = \sum_i E_i P_l(r_{s\,i}) \tag{3.20}$$

This can be written as a matrix transformation of a column vector E_{fit} into a column vector of the measured energy E with a square $k \times k$ (k= number of peaks found in group = number of overlapping showers) matrix doing the transformation:

$$S \times E_{fit} = V \tag{3.21}$$

$$S_{lk} = \sum_i P_l(r_{s\,i}) P_k(r_{s\,i}) \tag{3.22}$$

$$E_{k\,fit} = E_{k\,fit} \tag{3.23}$$

$$V_l = \sum_i P_l(r_{s\,i}) E_i \tag{3.24}$$

$$\tag{3.25}$$

To solve this equation EMREC inverts the S matrix, and finds the fit energies via

$$E_{k\,fit} = \sum_l S^{-1}_{kl} V_l \tag{3.26}$$

In the event that the matrix is not invertable, the peak with the lowest energy is dropped and splitting is reattempted.

If splitting is successful, EMREC procedes to refine the energies of the overlapping gamma showers. The goal is to completely separate the showers so that they are equivalently now single showers, and the fitting is redone to the single shower. To do this, the corrected pulse height on each channel i, for each shower k can be calculated as:

$$PH_{ik} = E_i - \sum_{j\,j \neq k} E_{j\,fit} P_j(r_{s\,i}) \tag{3.27}$$

Fits are then performed on these separated, equivalent single showers by the same procedure as is done on isolated showers. Thus positions and energies are now recalculated for these separated showers giving a new set of $E_{k\,fit}$ for each shower k, and refined positions for the shower.

Next to do the summed view energies, showers with peaks that match in positions in the front and back were fit according to

$$E(r_s) = .7 \times P_f + .3 \times P_b \tag{3.28}$$

where the front and back shower shapes are prescribed by equations 3.9 and 3.10. The fitting for the summed section is done in the same way described for the front section in the preceding paragraphs. Low energy showers would have their energy usually in the front section alone so they were not summed.

When a shower had peaks in the front and back section in the r view (this r is the radial coordinate in the LAC, and not the r from the center of the shower) the difference in r positions was calculated to determine the directionality of the photon. In the spectrometer chapter it was discussed how the strips in the calorimeter focused in on the target (see figure 2.9). So any particle traveling parallel to the z axis (like a muon) would hit different r strips in the front and back, thus having a non-zero directionality. Whereas particles coming from the target traveling at an angle with respect to z will cross the same strip numbers in front and having an essentially zero directionality. This is useful to cut out beam halo particles that do not originate from the target.

After the energies in the r and ϕ views have been found, then photons from the two views must correlated to define a single photon. The easiest matches were photons that were not on boundaries then photon were matched between the views by requiring that the front and back energies be within 3 sigma of each other. For photons that land on boundaries the process is harder. A complete discussion of the correlation process may be found in [8].

After the energies, positions, χ^2s, etc. of photons for a given event has been determined, they are written to the DST stream via ZEBRA in a compact binary exchange form. To analyze the physics in these events, the user invokes routines from the DST library that read in the events, and unpack the data into FORTRAN

arrays and variables which the user can then easily work with their own analysis code.

Chapter 4

ANALYSIS

The purpose of this analysis is to measure the inclusive low p_t π^0 cross section as a function of p_t (momentum transverse to the z axis). The differential cross section expresses the probability of finding a π^0 between p_t and $p_t + dp_t$ in a high energy collision. The data populates a p_t range of .6 $GeV/c \leq p_t \leq 2.25$ GeV/c, and over a rapidity(Y, is a quantity related to the amount of momentum in the longitudinal axis, and in the ultra relativistic can be shown to be related to the scattering angle) range of $-.75 \leq Y \leq .75$. To calculate a cross section, the yield of $\pi^0 s$ produced by the targets is measured, and then normalized to the beam that was incident on the target, and normalized by the phase space that was instrumented.

The data was collected during the 1990 fixed target run at fermilab in which a negative beam with 515 GeV/c momenta particles was incident on the spectrometer. This beam consisted of 97% π^- mesons. See table 2.1 for the 515 GeV/c beam content. The beam was incident on Cu and Be targets as shown in figure 2.2. As mentioned in the introduction chapter, the triggers used in this analysis were the beam trigger and the interaction trigger. The main goal of the experiment is the measurement of direct photons (photon = γ). The ratio $\frac{\gamma}{\pi^0}$ is enhanced at high p_t, thus the experiment implemented high p_t discriminating triggers so that the majority of the data taken would be of interest to study QCD 2-2 hard scattering and direct photons. These triggers are discussed in detail in chapter 2. The low p_t sample of data relied on the interaction, and beam triggers. These triggers were

scaled back (or prescaled as discussed in chapter 2) so as to not dominate the data taking rate with minimum bias events not of interest to hard QCD scattering events (as discussed in the introduction chapter). What this means, in the end, is that low p_t physics can be studied in this experiment, but with limited statistics. The threshold of the high p_t triggers was $\approx$ 2 GeV/c (the threshold changed on a time by time basis to accommodate a varying beam intensity.), and the minimum bias triggers had no minimum p_t requirement. In this thesis, an attempt is made to link the low p_t π^0 differential cross section from interaction data with the π^0 cross section from the high p_t triggers to get a complete cross section measurement from $.6\ GeV/c \leq p_t \leq 12.\ GeV/c$. The rest of this chapter will concentrate on how the data was analyzed, with cuts made, signal detected and defined, π^0's counted, and corrections made. When a π^0 (mass=.135 GeV/c^2) is produced in an interaction it has a mean lifetime of 8.4×10^{-17} seconds, and decays into the two γ mode 98.798% [Particle Data Group] of the time. It is this mode that is examined in this thesis.

4.1 Signal

If in a high energy collision (an event) a π^0 is produced among any of the reaction products, it will decay into two photons promptly. To reconstruct the π^0 one looks at photons detected in the LAC (liquid argon calorimeter). The four vectors of each photon are added together to get the four vector of the π^0. The invariant mass is then calculated from $mass^2 = E^2 - p^2$. This quantity would then be, in principle, ideally be around (the particle has a finite width due to $\Delta E \Delta t \sim h$ to $.1349764 \pm .0000006 GeV/c^2$[Particle Data Group] for the mass of the π^0. Experimentally however, the mass has a normal distribution due to the resolution of the detector which smears the measurements into a normal distribution. The mean of the mass peak may also be different depending upon the calibration (energy scale) of the calorimeter.

From data summary tapes (DST, as defined in chapter 3) the analysis code reads in an event, processes it, then drops it and reads in the next event until all events are processed. For a given event, the DST reconstructed variables for a given photon are ϕ, θ, energy (E), and vertex position of the collision vx, vy, vz are used to reconstruct the photon's four vector $P_4 = (E_\gamma, p_x, p_y, p_z)$. E is simply the reconstructed energy measured in the LAC. The angles θ and ϕ are calculated by using the reconstructed r and ϕ position on the face of the LAC, and the vertex position to form a vector from the interaction point, where the photon is assumed to have originated from, to the face of the LAC where the photon is detected as a shower. The components of $\vec{p}$ are easily calculated since for a photon E=$|\vec{p}|$, thus

$$E = E \tag{4.1}$$

$$p_x = E\sin(\theta)\cos(\phi) \tag{4.2}$$

$$p_y = E\sin(\theta)\sin(\phi) \tag{4.3}$$

$$p_z = E\cos(\theta) \tag{4.4}$$

All photons in a given event were looped over to generate all photon four vectors, $P^\mu = (E_\gamma, \vec{p_\gamma})$. Photon four vectors are then added in pairs to form possible π^0 four vectors. In a given event, photons detected in the LAC are produced from several sources including direct photons, photons from other particle decays such as the η, bremsstrahlung of charged particles, other π^0s and many other sources. It is not known *a priori* which photon comes from a given π^0, so all possible combinations of photon pairs must be formed and tried. Looping over all two photon combinations the π^0 four vector is calculated as, for photon pair i j as follows.

$$E_{\gamma\gamma} = E_{\gamma i} + E_{\gamma j} \tag{4.5}$$

$$p_{x\gamma\gamma} = p_{x\gamma i} + p_{x\gamma j} \tag{4.6}$$

$$p_{y\gamma\gamma} = p_{y\gamma i} + p_{y\gamma j} \tag{4.7}$$

$$p_{z\gamma\gamma} = p_{z\gamma i} + p_{z\gamma j} \tag{4.8}$$

The invariant mass for the pair i j is then calculated as

$$mass_{ij} = \sqrt{E_{\gamma\gamma}^2 - p_{\gamma\gamma}^2} \tag{4.9}$$

For each two gamma four vector formed the invariant mass is calculated, and histogrammed. The result for all two photon four vector combinations in an event summed over all events in the data sample is shown in histogram 4.1. The plot shows a smoothly varying background that is the result of combinations of two photon pairs that are the wrong combinations. The shape of the back ground is related to the phase space that is available to the two γ pairs in each p_t bin. The peak centered at .135 GeV/c^2 is the excess caused by combinations that come from the decay of π^0s. The width of the peak is due to the energy resolution of the LAC, which is $\sigma_i(E)^2 = .22^2 + .16^2E + 0.01^2E^2$, for determining the energy of the individual photons that form the two gamma pairs. Also, the resolution in determining ϕ and θ lead to inexact measurements of the photon four vector, thus leading to an inexact determination of the π^0 four vector. To calculate the cross section as a function of p_t, the mass plot shown in figure 4.1 must be broken down into p_t bins as shown in figures 4.2, 4.3, and 4.4. These histograms here have already been weighted on an event by event basis by corrections that are event dependent: conversion corrections, beam absorption, and the Lorentz invariant phase space factor $\frac{1}{\Delta Y\, p_t\, \Delta p_t}$. The meaning of these corrections are discussed latter in the chapter. The rest of the factors, which are constant, that go into the cross section are accounted for later (such as normalization, etc.). Interactions in copper are shown in 4.5.

To count the number of π^0s observed in a given p_t bin, the excess counts above the combinatorial background must be determined. This could done by fitting the background to a polynomial (fourth order in this case), and the peak to a Gaussian. Then the area under the Gaussian can be directly integrated, and divided by the mass bin width in the histogram to estimate the total number of π^0s under the background subtracted peak. However, in the case of the low p_t mass bins, the

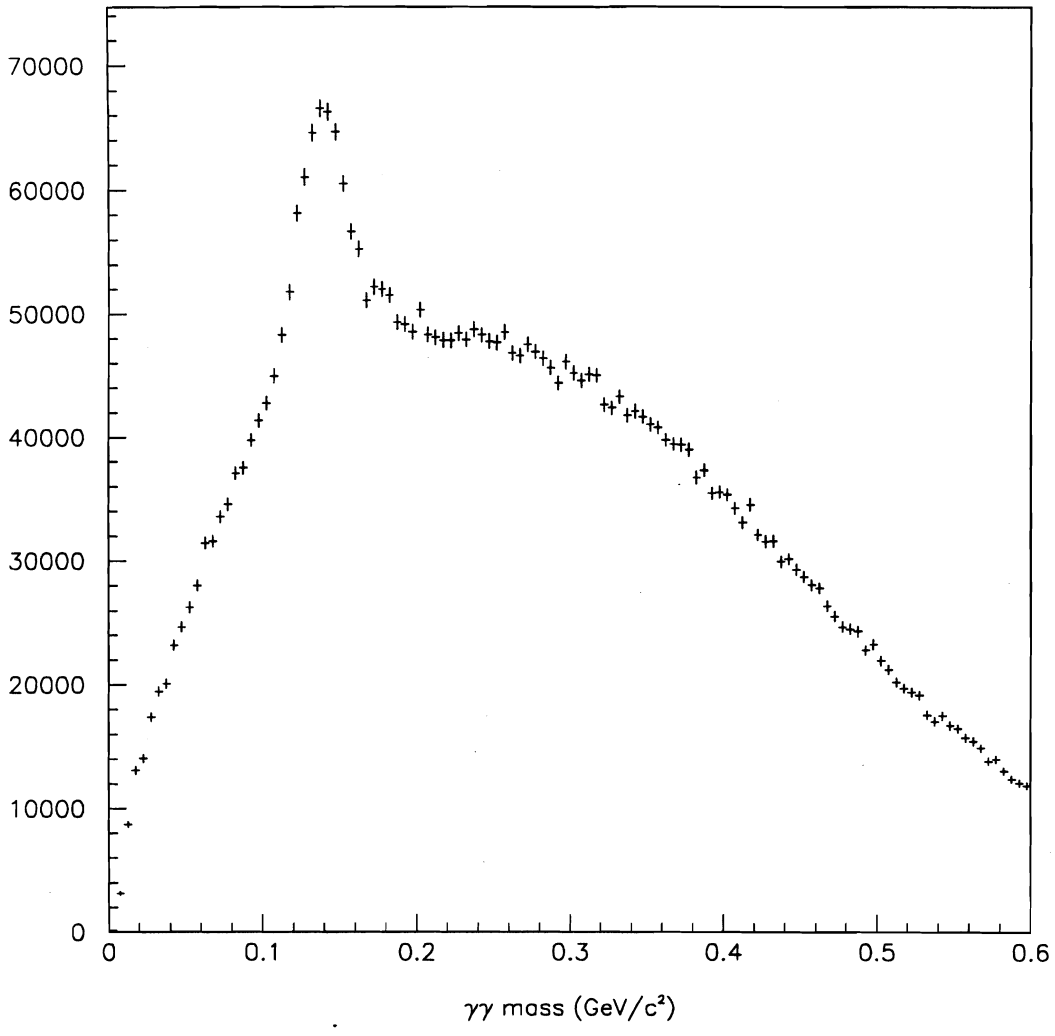

Figure 4.1: An invariant mass plot of all two gamma pairs in all events for the interaction trigger. The vertical axis is **Events**/($.005 GeV/c^2$), and the horizontal axis is in units of mass GeV/c^2.

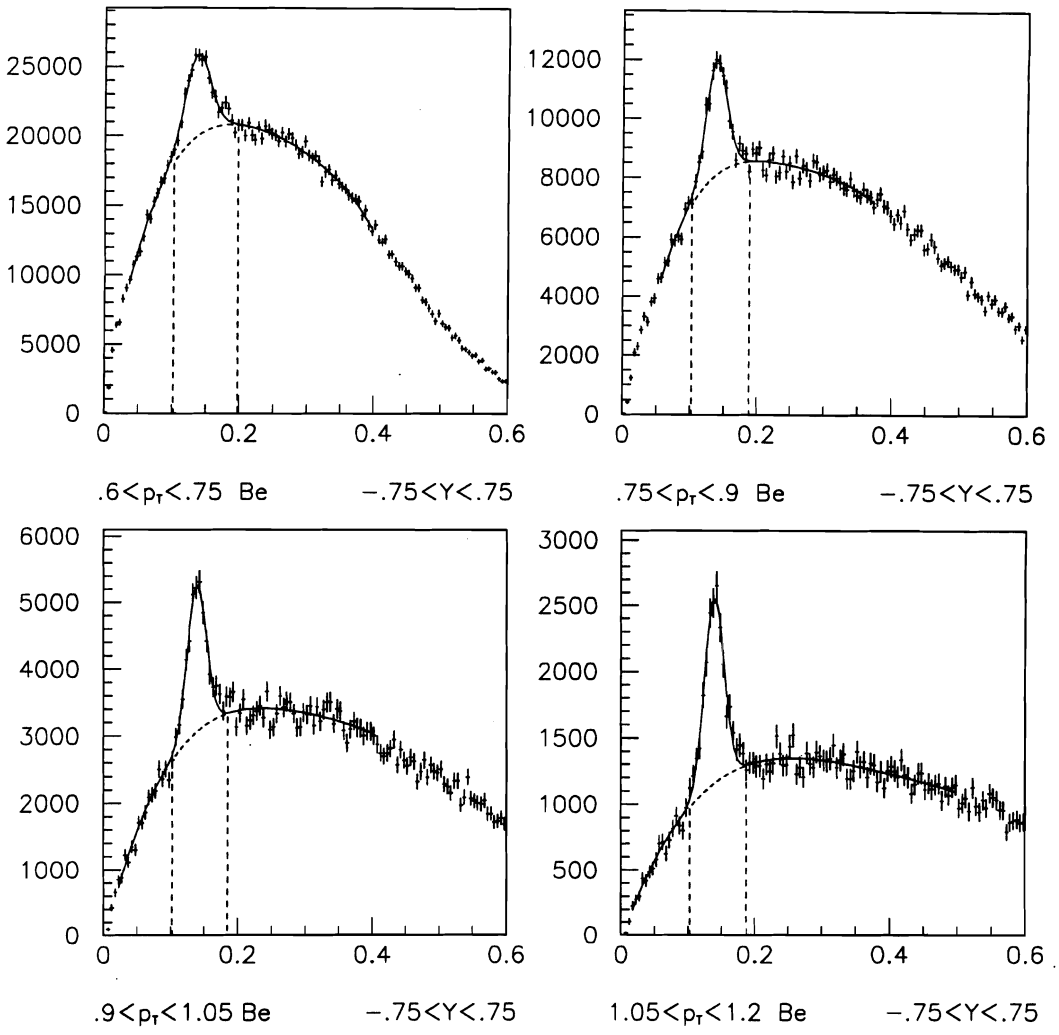

Figure 4.2: An invariant mass plot of all two gamma pairs in all events in the Be target for the interaction trigger broken into p_t bins of .15 GeV/c width. The entries in each bin are weighted for the conversion correction, the beam adsorption correction, and the phase space factor $\frac{1}{\Delta Y\ p_t\ \Delta p_t}$

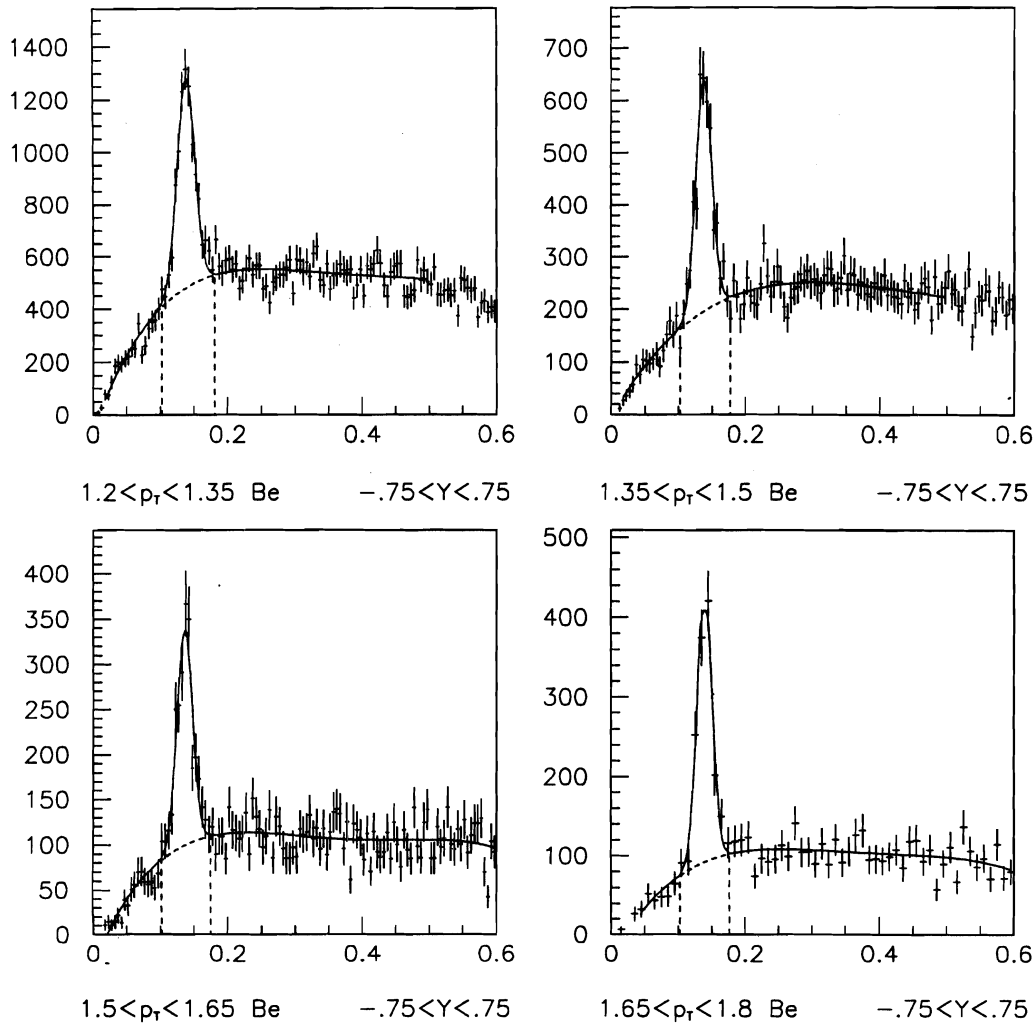

Figure 4.3: An invariant mass plot of all two gamma pairs in all events in Be target for the interaction trigger broken into p_t bins.

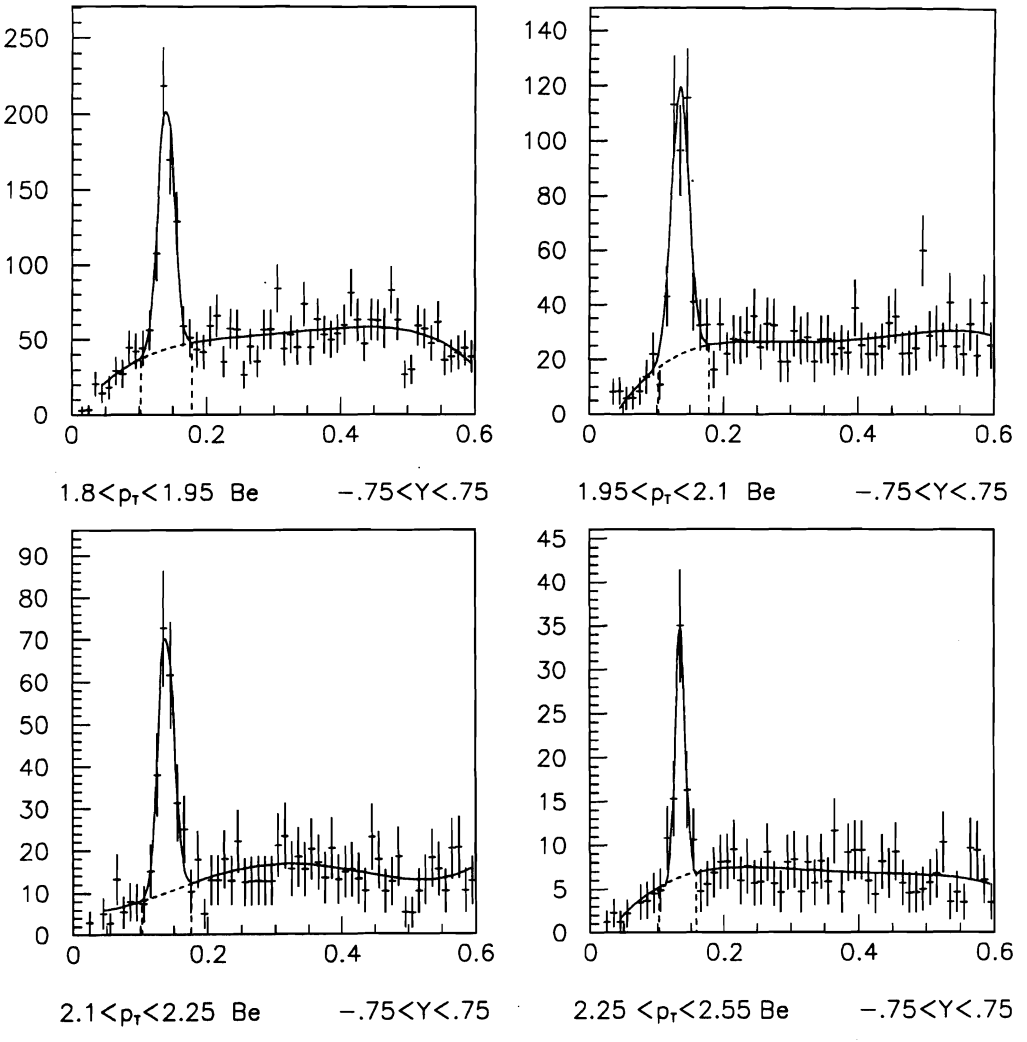

Figure 4.4: An invariant mass plot of all two gamma pairs in all events for the interaction trigger broken into p_t bins.

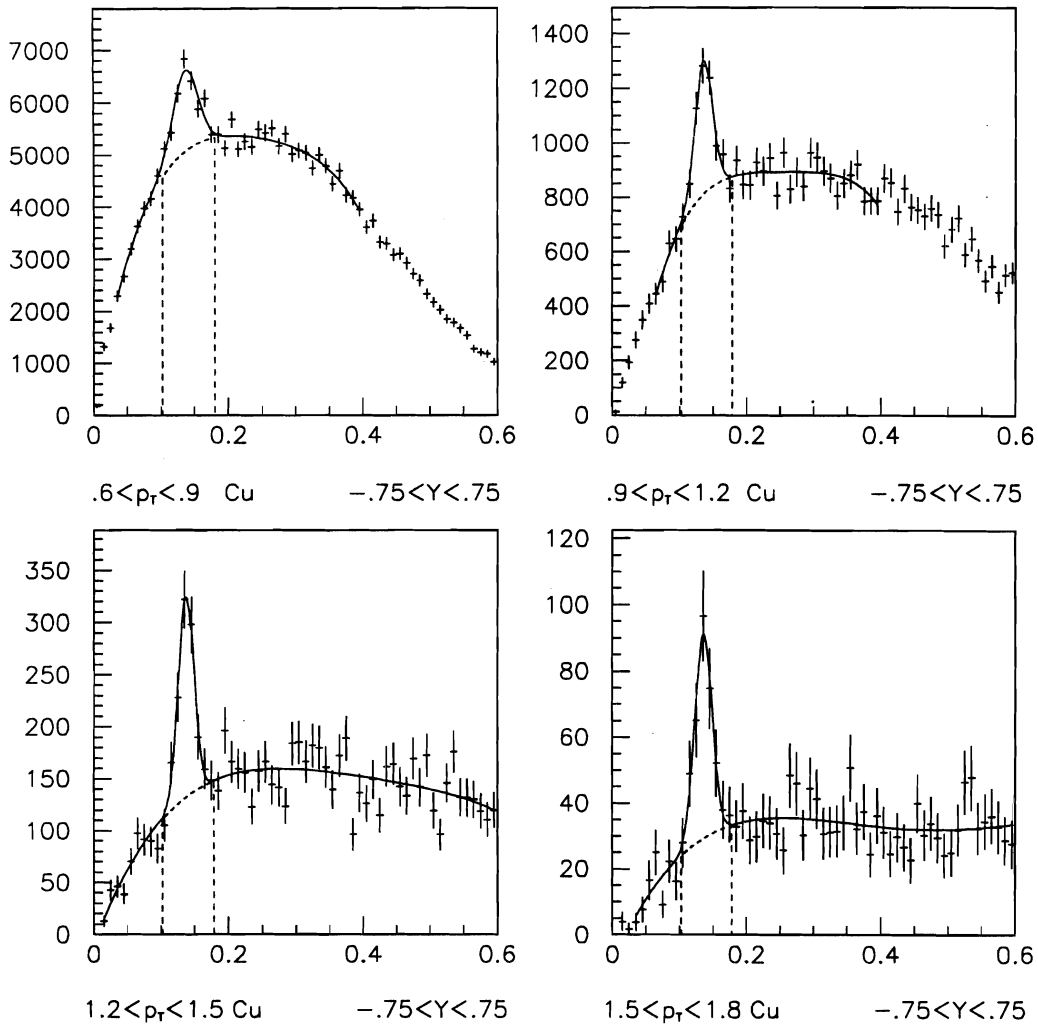

Figure 4.5: An invariant mass plot of all two gamma pairs in all events for the interaction trigger broken into p_t bins for the copper target.

distribution has a non-Gaussian tail (see the low p_t bins in figure 4.2) and the peaks are not fit well by a Gaussian, so instead what is done is to use the background fit under the signal peak region, and subtract the total counts in the peak from the background fit to arrive at the number of excess counts. The range which this count was taken over was $.1 GeV/c^2 \leq mass_{\gamma\gamma} \leq 3.3 \times \sigma\ GeV/c^2$. The σ is determined by the Gaussian fit on the mass peak in each p_t bin. By using this method the number of π^0s,$N(p_t)_{\pi^0}$, in each p_t bin can be determined, and thus used to calculate the π^0 production cross section as a function of p_t.

The acceptance of the LAC was found to be such that in rapidity (Y) in the center of mass frame (Y_{cm}) the coverage is $-.75 \leq Y_{cm} \leq .75$ [19], so the mass plots shown are over this Y_{cm} range. Y_{cm} is defined as

$$Y_{cm} = \frac{1}{2}\log\frac{E+p_z}{E-p_z} - \frac{1}{2}\log\frac{1-\frac{v}{c}}{1+\frac{v}{c}} \tag{4.10}$$

$$Y_{cm} = Y_{lab} - \frac{1}{2}\log\frac{1-\frac{v}{c}}{1+\frac{v}{c}} \tag{4.11}$$

The first term is the definition of Y, and it is labeled Y_{lab} since E and p_z are measured in the lab frame. The second term transforms this quantity to the center of mass frame of the π^0.

The rapidity is a measure of how much of the π^0s momentum is in the z direction, and thus in the ultra relativistic limit defines a scattering angle with respect to the z axis. To see this consider the following. For a relativistic particle $E = |\vec{p}|$ for all practical purposes. With $\vec{p}$ making an angle θ with respect to the z axis then one can write the following:

$$Y = \frac{1}{2}\log\frac{E+p_z}{E-p_z} \tag{4.12}$$

$$Y = \frac{1}{2}\log\frac{E(1+\cos(\theta))}{E(1-\cos(\theta))} \tag{4.13}$$

$$Y = \frac{1}{2}\log\frac{(1+\cos(\theta))}{(1-\cos(\theta))} \tag{4.14}$$

$$Y \approx \log tan(\frac{\theta}{2}) = \eta \text{ pseudo rapidity} \tag{4.15}$$

The E and $\vec{p}$ are measured in the lab frame by the detector, and the factor with the $\frac{v}{c}$ (c=speed of light $0. \leq \frac{v}{c} \leq 1.$) in equation 4.11 transforms the first term from the lab frame into the center of mass frame (moving at speed v with respect to the lab) of the collision.

The acceptance in rapidity comes from the physical size of the LAC with its hole in the middle and its finite outer radius; thus, giving an acceptance of $1.3\,\text{deg} \leq \theta \leq 9\,\text{deg}$. The reason for using rapidity rather than the angle θ is the that Y transforms trivially from one frame to another by a mere addition of a constant to any other frame; thus, making it easy to form relativistically invariant cross sections since ΔY will be the same in all frames.

The differential cross section calculated as a function of p_t expresses the probability of a π^0 being produced between p_t and $p_t + dp_t$ integrated over the phase space available to the experiment. To calculate the cross section, the yield of π^0s produced by the target must be measured, and then normalized by the number of beam particles incident on the target, and normalized by the phase available to each p_t bin that the calculation is performed in. Mathematically, the relativistically invariant differential cross section for the production of π^0s per nucleon in the target in term of pico barns/$(GeV/c)^2$ is expressed as

$$E\frac{d^3\sigma}{dp^3}\,(pb/GeV^2/c^2) = \frac{1}{2\pi p_t \Delta p_t \Delta Y_{cm}} \frac{1}{\rho l N_a} \frac{N_{\pi^0}^{corr}(p_t)}{N_{beam}^{corr}} \times ABS \times 10^{36} \qquad (4.16)$$

Experimentally, π^0's that were reconstructed from data are counted in bins of p_t whose width is .15 GeV/c (for Be, Δp_t = .3 for Cu), and the p_t data point is taken as the mean p_t in each bin. So this gives an average value for the cross section over the p_t bin. This quantity is just $N_{\pi^0}(p_t)$ observed. In the experiment, there are losses of π^0s due to inefficiencies in detecting photons that hit the LAC: acceptances, photon conversions, cuts and vertex finding inefficiencies. Therefore $N_{\pi^0}(pt)$ must be corrected to account for the losses of π^0's which is $N_{\pi^0}^{corr}(p_t)$. The factor $2\pi p_t \Delta p_t \Delta Y_{cm}$ is the element of Lorentz invariant phase space that the

detector was able to observe, so the factor $\frac{1}{2\pi p_t \Delta p_t \Delta Y_{cm}}$ normalizes the cross section in phase space. The factor 2π is for the integration of ϕ from 0. to 2π. ΔY is the range in rapidity scattering angle that the detector covers. Δp_t is the width of the p_t bin that the number of π^0s was counted in. The factor $\rho l N_a$ gives the number of scattering centers (nucleons) per unit area in the target. ρ is the density and l is the length of the target, and the N_a is Avogrado's number. The N_{beam}^{corr} is the corrected beam count, which is how many particles were incident on the target and available while a trigger was ready to be accepted. This normalizes the number of events in the cross section to the total number of possible interactions available. Each beam particle entering the experiment is an independent trial of what can happen when a beam particle interacts with a nucleus of target material so N_{beam}^{corr} normalizes the results to the number of trials performed. The correction superscript is due to the fact the total beam count had to be corrected for the fact that not all the beam counted was incident on the targets. The factor of 10^{36} is the conversion from cm^2 to pico barns. The cross section has units of area/energy^2 and this tells one what the effective scattering area per nucleon that the incident beam sees to produce π^0s. The unit of pico barns is used here because the high p_t cross sections are small, and thus calculated in *pb*. To compare with the high p_t cross section *pb* was chosen in this study also. The ABS is the correction to the cross section for beam absorption due to the fact that the targets are not infinitesimally thin.

The equivalence of both sides of equation 4.16 can be shown from the fact that $E\frac{d^3\sigma}{dp^3}$ can be rewritten using the fact that

$$\frac{1}{E} = \frac{dy}{dp_z} \tag{4.17}$$

which can be derived from the definition of rapidity evaluated in the center of mass frame (i.e.$p_z \rightarrow 0.$). Transforming to polar coordinates so that

$$dp_x dp_y \rightarrow p_t dp_t d\phi \tag{4.18}$$

$$p_t = \sqrt{p_x^2 + p_y^2}$$
$$\phi = \tan(\frac{p_y}{p_x})$$

Thus,

$$E\frac{d^3\sigma}{dp^3} = \frac{d^3\sigma}{d\phi dy p_t dp_t} \tag{4.19}$$

integrating over ϕ

$$E\frac{d^3\sigma}{dp^3} = \frac{d^3\sigma}{2\pi dy p_t dp_t} \tag{4.20}$$

The cross section ,$d^3\sigma$, per nucleon is experimentally measured as the quantity $\frac{N_{\pi^0}^{corr}(p_t)}{N_{beam}^{corr}\rho l N_a}$. dy is taken as ΔY, dp_t is the bin width Δp_t, and p_t is the measured p_t of the 2 γ mass pair.

It is easy to see that the left hand side is an invariant quantity since ΔY is invariant. p_t is unchanged in any frame since the boost is along the z direction. And the product ρl is invariant since for a Lorentz contraction the length goes as $l' = l\sqrt{1-\frac{v^2}{c^2}}$ for an observer in the $'$ frame, and the density goes as $\rho' = \frac{\rho}{\sqrt{1-\frac{v^2}{c^2}}}$. Thus, in the product the Lorentz contraction cancels out leaving the quantity invariant. Of course, all the other scalars, like numbers of particles observed and N_a, are the same in all frames.

4.2 Corrections

The number of π^0s observed in a given p_t bin must be corrected for losses caused by detector inefficiencies and cuts. This is done by weighting the counts of two photon pairs observed when filling the invariant mass histogram for a given p_t bin by correction weights calculated from probabilities of losses. So

$$N_{\pi^0}^{corr} = \sum_{i=1}^{N_{\pi^0}} W_i(p_t) \tag{4.21}$$

$$W_i = C\, W_{conv}(x,y,z,\theta,\phi)\, W_{vtrx}\, W_{recon}(pt) \tag{4.22}$$

The C is correction for hard cuts made on the data: target fiducial cuts, and the vertex not being found in an event cut. $W_{conv}(x,y,z,\theta,\phi)$ is the correction for

lost photons due to conversion to e^+/e^- pairs. W_{vtrx} is the vertex reconstruction efficiency. $W_{recon}(p_t)$ is the efficiency for the LAC to reconstruct photons within the rapidity range that we are calculating the count of π^0s.

4.2.1 Conversion Correction

Photons produced in the interaction travel through material that makes up the spectrometer. Ideally, one would like to have detectors and infinitesimally thin targets that will not interfere with the pure physics happening during a collision, and yet still measure everything interesting. This is impossible, but in the design one tries to minimize the amount of material, and still have good detection characteristics to get quality measurements. Extremely thin targets would give an impractically low event rate. When a photon is produced by an interaction in the target, it must travel through the material in the rest of the target, the SSDs, the scintillator counters, the magnet, and through the multiwire proportional chambers before it strikes the LAC where it may be detected. While passing through all this material it may have interactions with the atoms that make up the material of the spectrometer. A photon that has a near collision with a nucleus may just scatter off of it or it may convert to a electron-positron pair. The probability of this conversion is

$$P_{conv} = 1 - e^{(-7/9\,\frac{\Delta X}{X_0})} = 1 - P_{noconv} \tag{4.23}$$

where X_0 is the radiation length of the material in which a particle looses $1/e$ of its initial energy. ΔX is the total distance traveled by the particle through the material. P_{noconv} is the probability that the photon did not convert. To do this correction, a ray from the vertex position to where the photon hit the LAC was calculated. Then the materials in the spectrometer from the vertex (v_x, v_y, v_z) position were looped over adding up the $\sum \frac{\Delta X_i}{X_{0i}}$ for each i^{th} material intersected by the ray. This was done from the vertex to just past the magnet. After the magnet if a pair was produced the two electrons generated would travel parallel

to each other separated by a very small distance (since after the magnet they could not be separated by the magnetic field), and would just deposit the energy of the initial photon into the LAC. In EMREC, the pair would have landed close enough together that it would just look like a single photon in the data, thus be reconstructed as a single shower. To determine if a photon candidate came from one of these pairs, the charge tracking system could be used to see if a track points to the photon candidate or not. This was not done in the low p_t analysis, because the signal to background ratio did not change using this cut.

To do the conversion correction, the weight to each 2 photon mass pair i j would be

$$W_{conv} = \frac{1}{P_{noconv\ i} P_{noconv\ j}} \tag{4.24}$$

The probability of conversions is dependent on $v_x, v_y, v_z, \theta, \phi$, because the amount and type of material seen by particle depends on track length, and direction. A plot of the probability of non-conversion is shown in figure 4.6.

4.2.2 Reconstruction Efficiency

What is meant by reconstruction efficiency is the efficiency that the calorimeter, coupled with the reconstruction and analysis code, reconstructed π^0s from the data. Then losses in the data may corrected for. To study efficiency a very careful and detailed Monte Carlo code was written [7, 24]. The code was based on the GEANT [20] simulation packaged that was developed at CERN. Physics collisions were simulated with another Monte Carlo code called HERWIG [21] which generated events, and passed the four vectors of the particles, and particle types generated in the collision on to GEANT. GEANT propagates the particles through the simulated detector, and the simulation generates Monte Carlo data tapes that correspond to raw unpacked data from the detector. The Monte Carlo data is then reconstructed using the same reconstruction code, MAGIC(see chapter 3), as was used on the data collected from the experiment (see figure 3.1), and the results

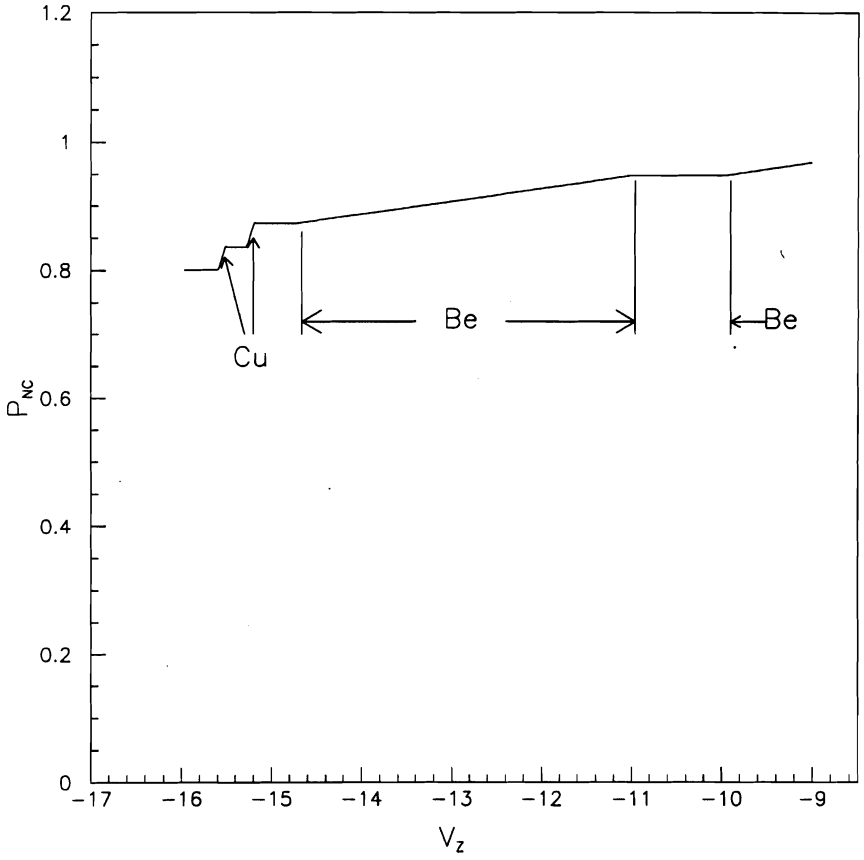

Figure 4.6: The probability of non-conversion of photon through the targets as a function of v_z. The angles $\theta = 5\,\text{deg}$ and $\phi = 0\,\text{deg}$, and vx and vy are centered in the target.

analyzed similar to that of the data. In the Monte Carlo, it is known precisely what physics was generated in the interaction; thus, one can measure how well the detector and reconstruction code do at giving the correct measurements of the physics. In this way one can determine detector efficiencies, and correct the real data for them.

Event Generator

The first step in doing an accurate simulation is to have a Monte Carlo that successfully generates the correct physics events based on quantum chromodynamics models (QCD). QCD as described in chapter 1 is a model to explain the interactions of quarks and the gluons that mediate the strong force to hold the quarks together to form bound states of hadrons: mesons (2 quark systems such as the π^-, π^0, and others), and baryons (3 quarks systems: protons, neutrons and others). The incident beam is a beam of π^- mesons, thus implies that the valence quarks are the bound state of $d\overline{u}$. d=down quark with -1/3 e charge (e is the charge of the electron) and the $\overline{u}$ is the anti matter up quark with -2/3 e charge. This meson then will then interact with a nucleus of target material which is composed of protons and neutrons and their valence quarks of $p = (u, u, d)$, and neutrons $n = (d, d, u)$ (u=+2/3 e and d=-1/3 e). The quarks and gluons from the meson will interact with the quarks and gluons of a target nucleon and interesting physics from their interaction will result. From the introduction chapter an example of Feynman diagrams for two processes that can occur are shown, and it is these diagrams, among many other possible diagrams, that the event generator must simulate. Doing calculations in QCD are not trivial. The calculations must be done perturbatively, and usually only the first and sometimes the second order can be evaluated. Once the point cross section is evaluated, then the outgoing partons must be hadronized through fragmentation functions that are not calculable, but rather measured from experiment. Nonetheless, people have written simu-

lations based on simplified phenomenological models, and fits with experimental data that simulate the physics well enough to be used for detector studies. Thus, theory, Monte Carlo, and experiment provide feedback to each other improving knowledge of hadronic interactions.

It is important that the simulation resemble the event complexity reasonably well so that inefficiencies due to the number of charged tracks confusing the tracking system, and number of photons confusing the EMREC reconstructor are modeled. The Monte Carlo used to do the event simulation was FORTRAN code called HERWIG (Hadron Emission Reactions With Interfering Gluons) written by B.R. Weber and collaborators [21]. HERWIG contains the parton distribution functions for gluons, quarks that make up hadrons mesons, and generates to a good approximation the interactions of the type that are shown in the schematic figure 1.3. In doing the analysis it was found that HERWIG did the most reasonable simulation of event complexity of the available event generators such as ISAJET [22] or LUND Monte Carlo Pythia [23]. HERWIG had several switches for different biases in generating events. For the simulation of the minimum bias data sample HERWIG process 8000 (which is HERWIG's minimum bias) was selected. For simulation of high p_t events, HERWIG process 1500, which is the QCD 2-2 hard scatter, was selected.

To see how well HERWIG did at simulating the physics events that were observed in data see figure 4.7 for number of tracks, and figure 4.8 number of photons comparisons between Monte Carlo and data. Comparisons of the reconstructed Monte Carlo mass distributions with the data are shown in figures 4.10, 4.11, 4.12. Figure 4.13 shows that the background subtracted signal shapes compare well.

Beam Simulation

In generating Monte Carlo data, the incident beam must be simulated. This was done by sending π^- mesons with 530. GeV/c momentum (this was the nominal

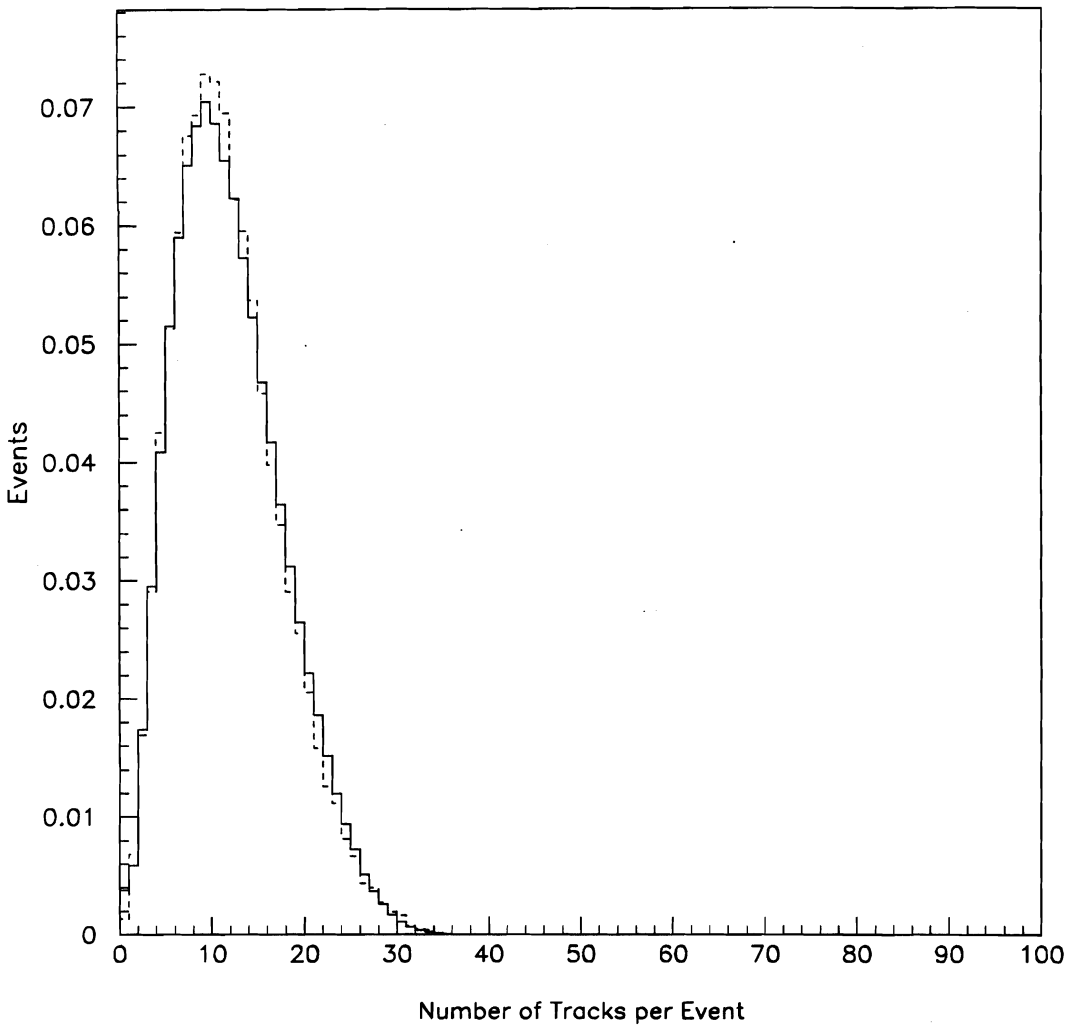

Figure 4.7: Comparison of the number reconstructed tracks in Data (solid) and Monte Carlo(dashed) histogrammed for each event. The simulated event complexity must be the same in order to measure inefficiencies in the tracking system and tracking reconstruction software PLREC. The data and Monte Carlo data distributions are area normalized to each other.

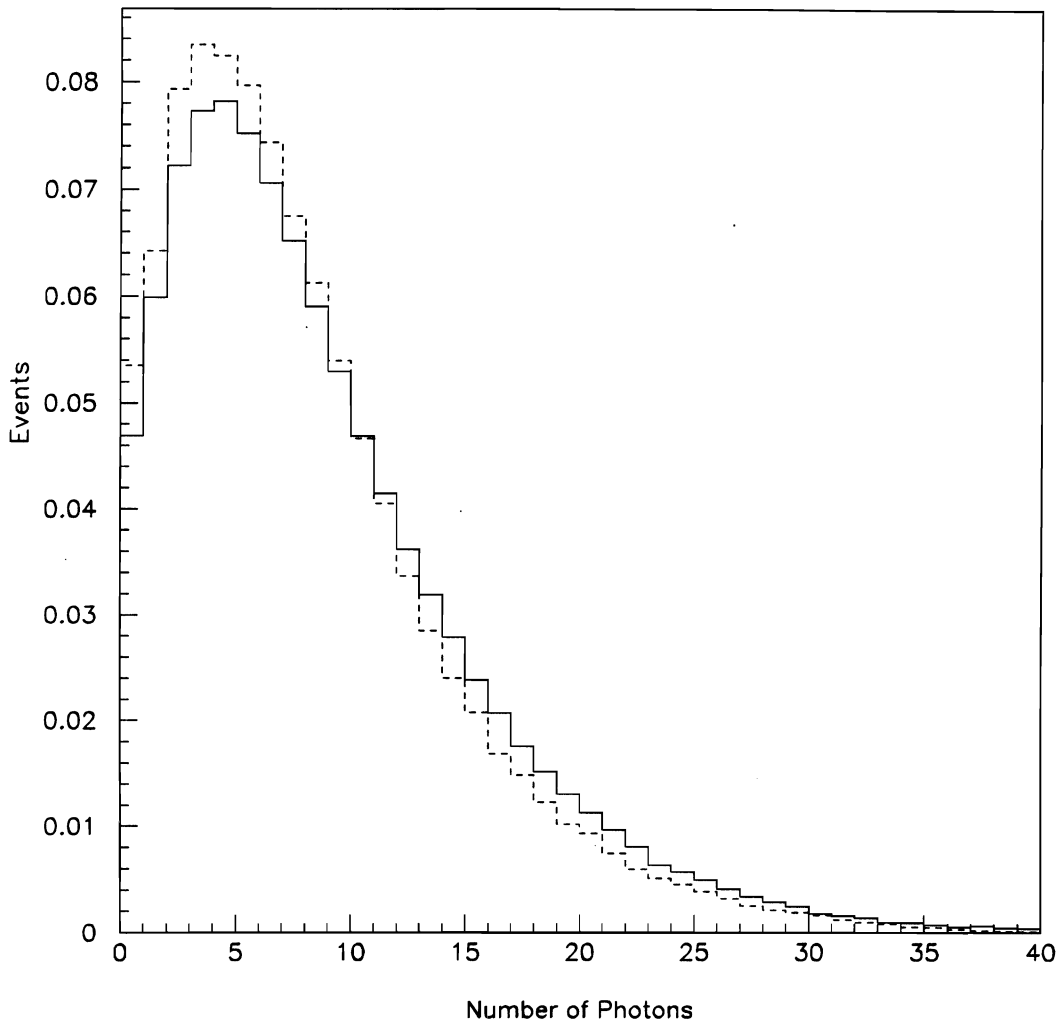

Figure 4.8: Comparison of the number reconstructed photons per event in Data (solid) and Monte Carlo(dashed). The simulated event complexity must be the same in order to measure inefficiencies in the LAC and the reconstruction software EMREC. The superimposed distributions are area normalized to each other

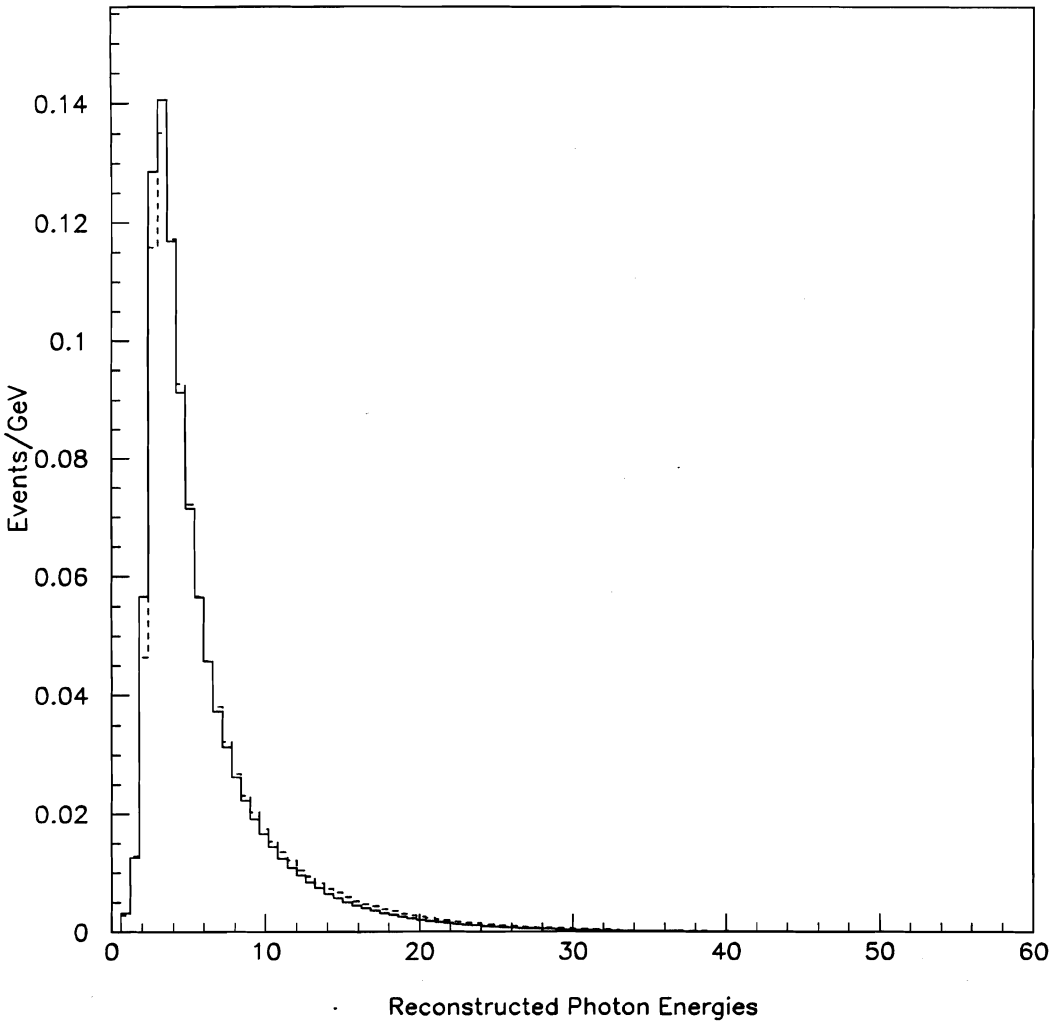

Figure 4.9: Comparison of the reconstructed energies between data and Monte Carlo. The two distributions are area normalized to each other.

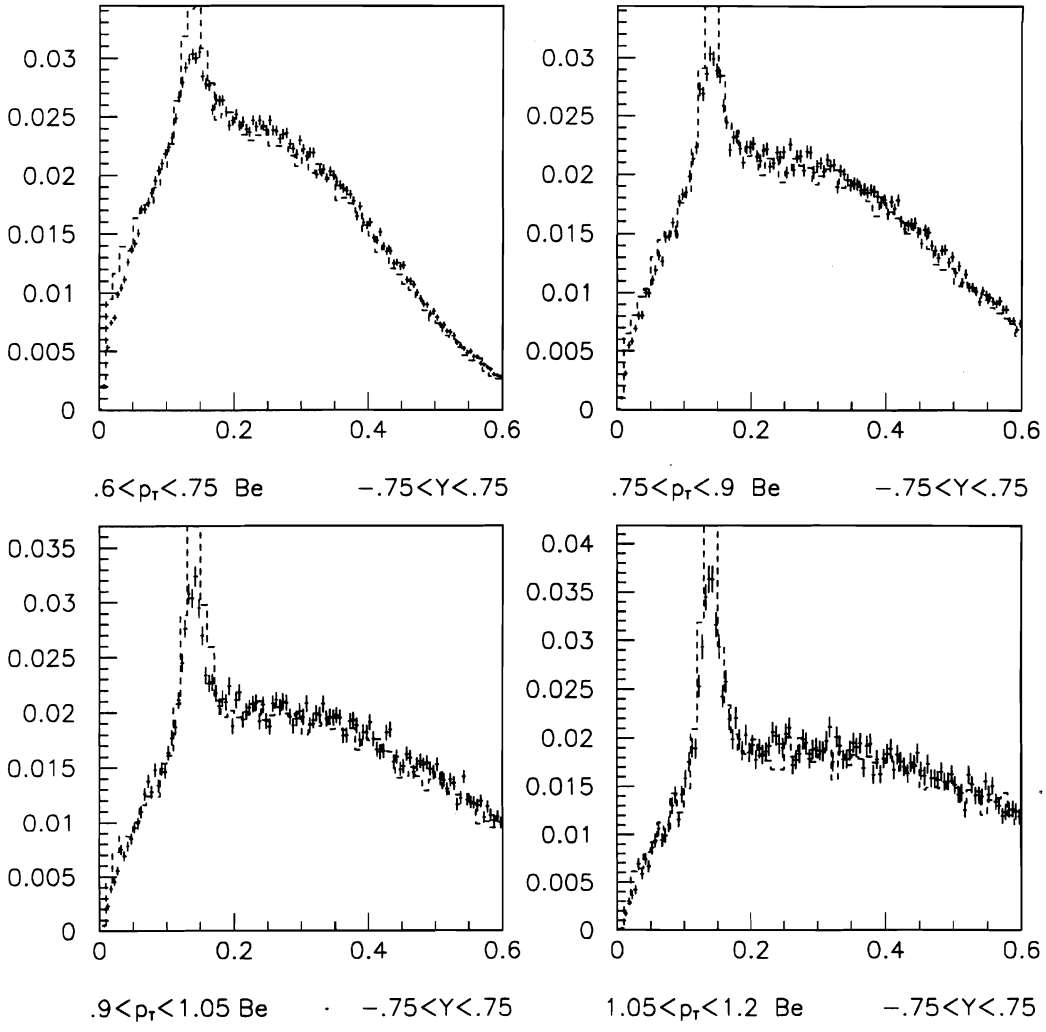

Figure 4.10: Comparison of the 2 γ mass distribution in data and Monte Carlo area normalized.

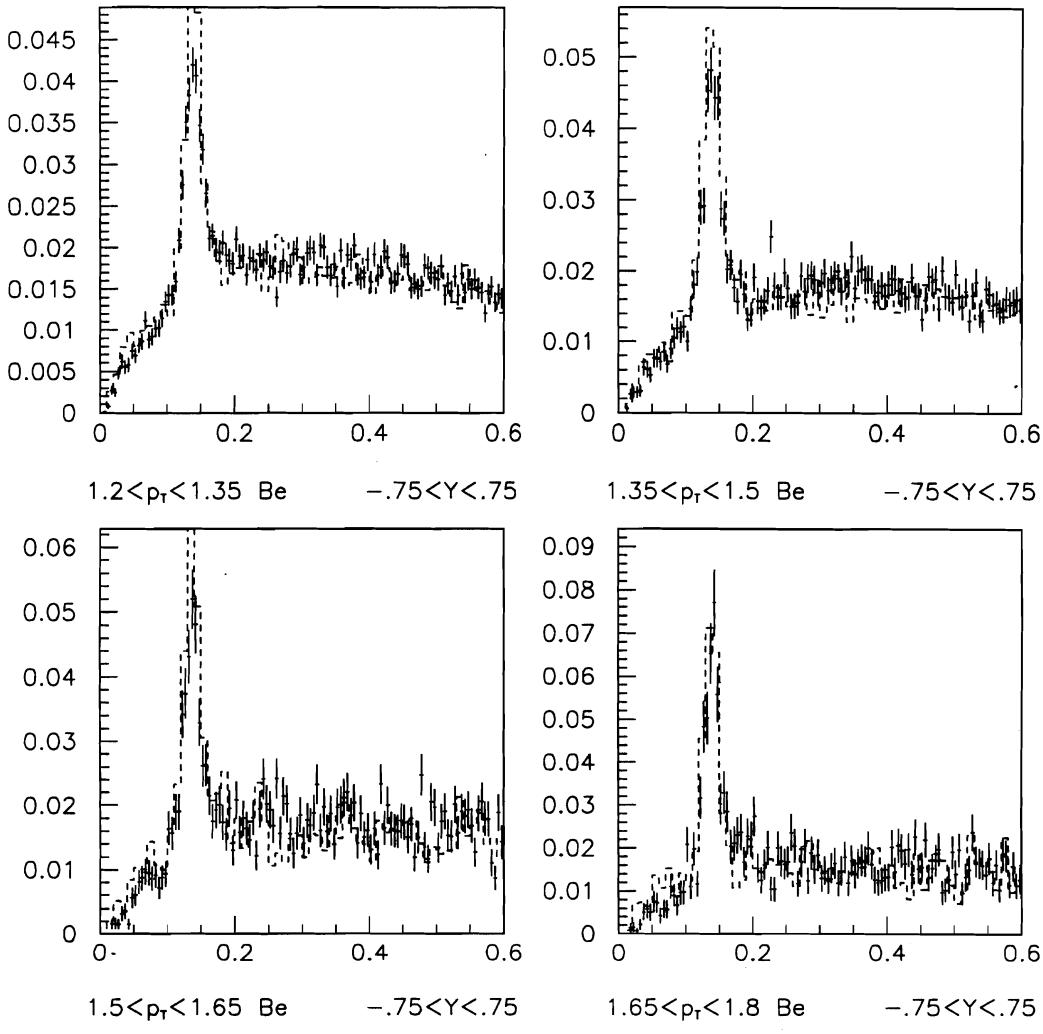

Figure 4.11: Comparison of the 2 γ mass distribution in data and Monte Carlo

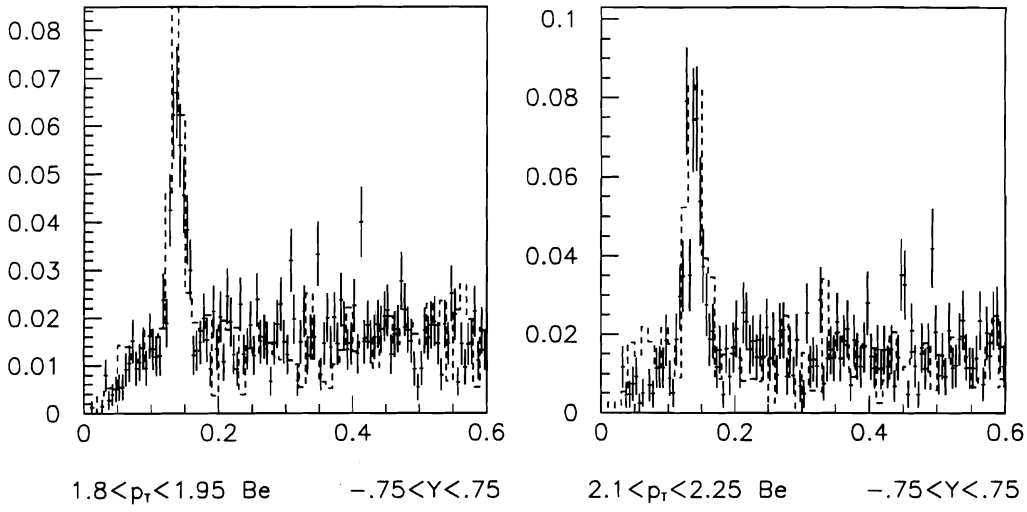

Figure 4.12: Comparison of the 2 γ mass distribution in data and Monte Carlo

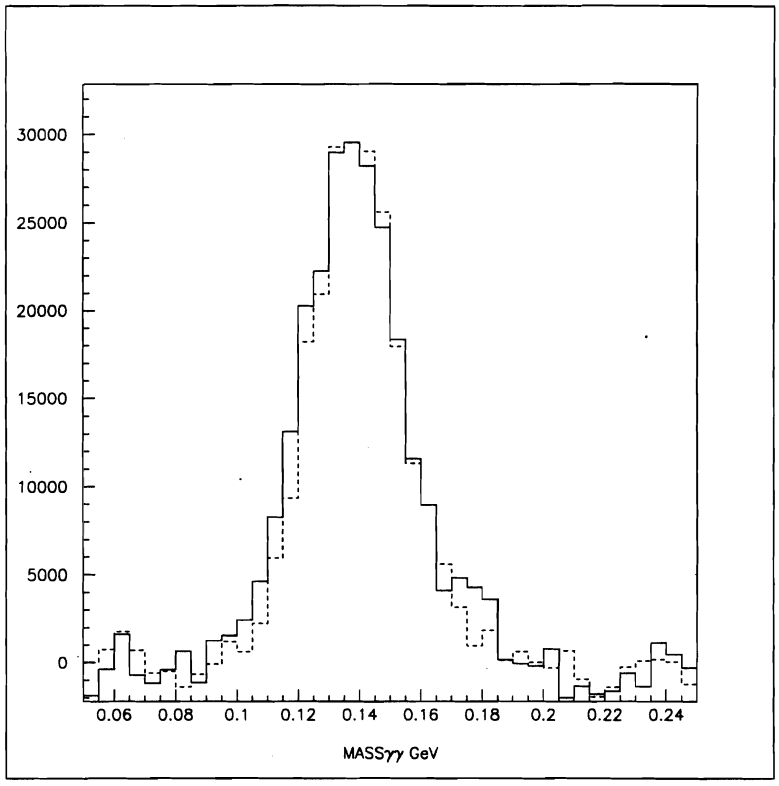

Figure 4.13: Comparison of the 2 γ mass distribution background subtracted in data and Monte Carlo. The Monte Carlo data is scaled to the peak value of the data.

beam momentum) in the z direction into the software modeled spectrometer. The spatial directions of the beam in x and y are smeared out by a Gaussian centered on the middle of the target to simulate the real beam profile. To find a vertex position in the material of the spectrometer the materials of the spectrometer are looped over in thin slices dz. In each slice dz the distance to where the next interaction would take place is calculated. If it interacts in the slice dz, then the vertex position is placed there, if not then the next slice is considered. See figure 4.14 for the how well this works in generating the vertex distribution. Now once a vertex position is found, the HERWIG generator is called, and a memory bank is filled with the generated four vectors of particles produced in the simulated collision. The Monte Carlo GEANT will then propagate the particles placed in the memory banks through the spectrometer. It is these generated particles which are then later compared to what was reconstructed to get efficiencies.

Detector Simulation

Once the collision is simulated, the four vectors of the generated particles are propagated through the GEANT simulation Monte Carlo which has been developed over a period of many years by the CERN computing group.

In GEANT, the user writes code that describes the physical shapes of detector elements and the materials these elements are made from using a tool kit that GEANT provides. The entire geometry, and material types of the E706 spectrometer were programmed in using the GEANT convention.

In simulating particle tracks that traverse through material that makes up the spectrometer, GEANT has programmed in it many of the cross sections for scattering, pair production, energy loss and other processes for materials that affect particles passing through material. If a material's properties are not pre-programmed in GEANT, then GEANT calculates them based on models that give cross sections in terms of atomic number A, density, and element type of

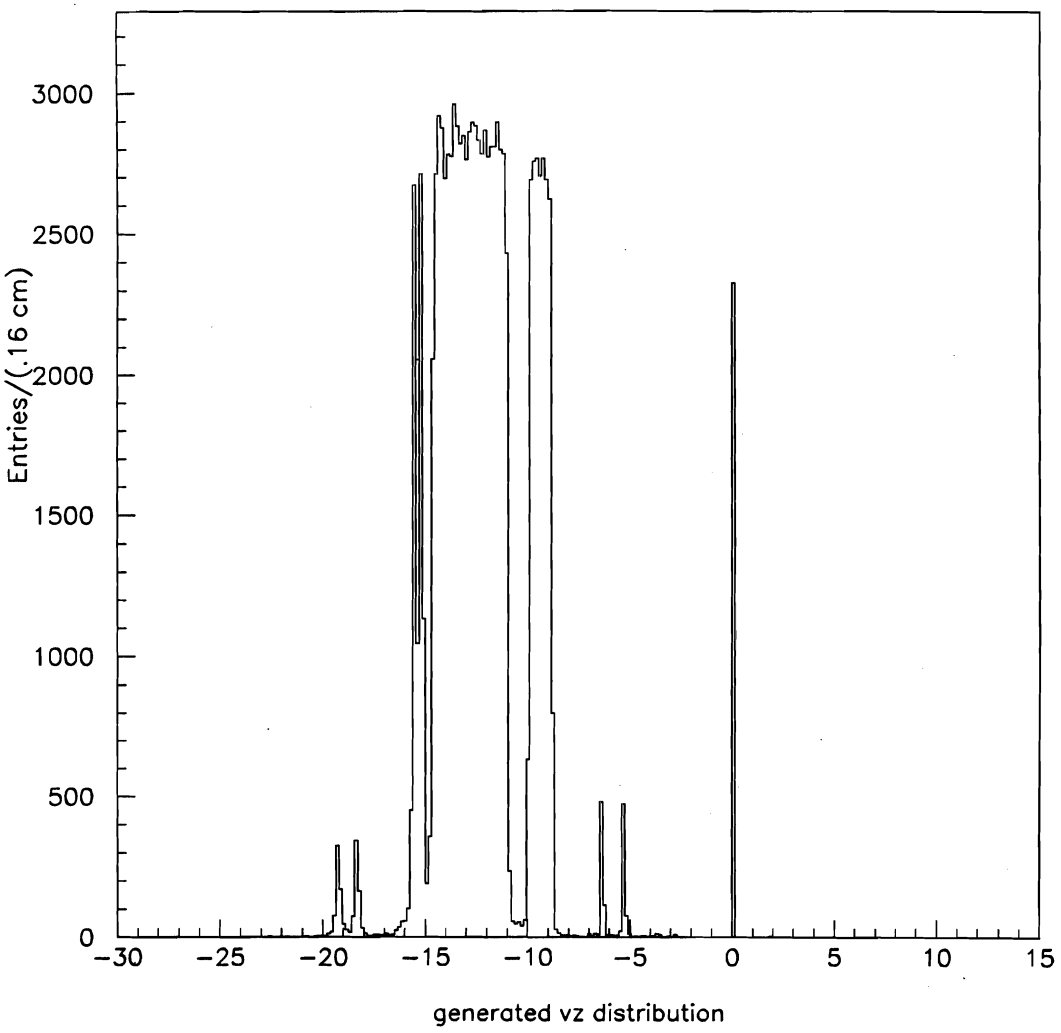

Figure 4.14: The reconstructed vertex distribution from Monte Carlo data. The entries at zero are events where the reconstructor failed to find the generated vertex.

compounds that make up the material provided by the user. So all the tracking chambers, the LAC, and any other material which will effect the particles passing through the spectrometer are programmed in.

For a given particle trajectory GEANT samples the cross section distribution of all available competing physical processes. From this sampling, distances that the particle will travel when a given process will occur are returned. GEANT will then select the process that will happen within the shortest distance. The GEANT then scatters the particle through an angle ϕ, θ according to a scattering distribution, gives the particle some energy loss for distance traveled and propagates the particle to that point, and then executes the process at that point. For example it could be a π^0 decaying into two photons, or photon pair converting. If no process happens within a given volume, then the particle is moved up to the boundary of that volume, and interactions in the next volume are then calculated and executed. If the particle does not decay, GEANT then propagates the particle again, and again until it decays or its energy falls to the point the track is stopped (usually 10KeV). If an interaction such as a decay occurs then daughter products are tracked through the detector, and if any daughters are decayed then their daughters are tracked through the detector. If a charged particle bremssthralungs a photon, then that photon will be tracked. So for a π^0 produced, GEANT tracks the π^0 till it decays, and suppose it decays into two photons then these photons are propagated through the spectrometer. If these photons make it to the LAC with out converting then they are showered in LAC with the energy that is being lost in the liquid argon sampling layers being added up in the LAC channels to be used as data for the reconstructor.

The user programs in the physical size, material contents of the detector, and declares certain elements as sensitive. These sensitive elements when hit by a particle will have their data recorded just like their real lab counterparts that they are modeling. For example, the straw tubes themselves would be declared sensitive,

but not the aluminum frame supporting the tubes. Hits by charged particles on tracking chambers are recorded as data to be used by the reconstructor. A hit on the frame would just result in energy losses and interactions for the particle passing through the frame. Energy deposited by particles in the liquid argon layers of the LAC are added together as LAC channels in the same was at the layers in the LAC are wire "OR'ed" as LAC channels. At the end of a simulated event a data event is then written out. A Monte Carlo data event contains two parts: first, the generated data from the primary collision; secondly, the digitized data from hit elements that resembles their real lab counter parts as readout of the spectrometer.

The Monte Carlo detector is a perfect, ideal detector. The simulation of noise and inefficiencies of various detector elements were put in through a Monte Carlo pre-processor. The Monte Carlo data tape contained data from the ideal modeled detector, so before passing the data event through to the reconstructors for processing, the data event was run through the pre-processor. The Monte Carlo had clean hits on tracking elements, and clean showers in the LAC. The pre-processor added noises to LAC channels, and put in noise hits on tracking chambers as well as remove hits occasionally to the tracking chambers to simulate hit efficiencies. The pre-processor also added noise to LAC channels.

The philosophy behind the idea of handling noises and inefficiencies through the pre-processor rather than the Monte Carlo itself was as follows. It takes a long time to generate a Monte Carlo event, and if noises were not originally right in the simulation, then the simulation would have to be done all over again and months of computation compromised. By using the pre-processor certain detector characteristics can be studied in matter of hours rather than days, and changes made easily to the Monte Carlo data sample without having to regenerate the Monte Carlo data sample. Only reconstructed Monte Carlo data would have to be regenerated, and not the entire simulation from scratch.

A very important facet of the pre-processor was to speed up the LAC simulation

[24]. To track every particle generated from bremsstrahlung, and pair production of the electromagnetic showering of an electron or photon in the LAC would take a lot of time. Typically, a particle is tracked until its energy falls below 10 KeV, thus the Monte Carlo would be tracking hundreds of shower particles for a very long time. To help speed up the MC simulation time a 10 MeV cut off was imposed on shower particles in LAC showers at the Monte Carlo level. Later, the pre-processor then used a shower shape parameterization to correct the energy in the LAC channels for this 10 MeV cut off, before passing the event on to EMREC for reconstruction as was shown in 3.1

Efficiency

After the MC data is generated, it is then processed by the pre-processor, then reconstructed by MAGIC, and analyzed by the DST data analysis code. The π^0s are then found in the generated events, and compared to what was reconstructed for those events to get an efficiency for each p_t bin. In the LAC there are several sources of inefficiencies:

- Acceptance. The LAC was not active on quadrant boundaries. This is where the G-10 boards that make up a quadrant are supported, and connector strings that readout the R boards are run out of the LAC. Photons that land in quadrant boundaries go undetected. Photons that land near quadrant boundaries are lost since part of their shower will escape into the uninstrumented quadrant boundary, and thus their energies will not be fully reconstructable. These photons are rejected in the analysis code by a EM-LAC fiducial cut. Further, each quadrant was split into two regions that were electrically separated to form octants in the LAC. Photons that land on an octant boundary are cut out since it was found that EMREC was not fully efficient at reconstructing these photons [25]. The finite size of the LAC does not give complete 4π coverage in the center of mass frame, and photons

that land on the inner and outer boundaries of the LAC will be lost since part of their shower will escape the active areas of the LAC. A LAC fiducial cut was imposed across the face of the LAC to cut out photons that land in these regions as shown in figure 4.15. Finally, in this analysis $\pi^0 s$ were reconstructed from photons that landed in the same quadrant, thus $\pi^0 s$ whose photons landed in different quadrants are cut out by the analysis code. This was done because of energy scale difference between different quadrants.

- Asymmetry. Asymmetry is defined by equation 4.25. As the asymmetry of the π^0 decay in the lab frame approaches unity, this means that one of photons in the decay is of low energy in the lab frame. The LAC has a minimum threshold for reliable reconstruction of photons, and in the analysis a 3 GeV cut in energy was placed on reconstructed photons. Thus, low energy photons will be lost causing the efficiency to be low for high asymmetric π^0s.

- $\frac{E_{front}}{E_{total}}$ cut. The ratio of the energy collected in the front of the calorimeter, E_{front}, as compared to what was collected in total active volume, E_{total}, is a useful variable cut to cut out the hadron contamination. Refer to figure 3.5 for the ratio of energy in front to the total energy measured. The large peak is caused by the showers of photons while the small peak is caused by the hadrons that start to shower before they reach the hadron calorimeter. A cut of .2 was applied to this ratio, but at the expense of chopping off the tail of the photon distribution; hence these photons are lost.

- Rapidity. Rapidity is defined by equation 4.11. If in the center of mass frame the π^0 is produced with backwards rapidity (i.e. $Y < 0.$), it will produce low energy photons in the LAB frame which may be lost in the LAC. At low energies the efficiency of detection and reconstruction decreases with decreasing rapidity.

To account for these losses, efficiencies must be calculated, then these losses are corrected by weights which are the reciprocals of the efficiencies. To calculate the efficiency, Monte Carlo reconstructed data is read in by the analysis code, and analyzed in the same way that the real data is. All two photon mass combinations are calculated, and invariant mass plots of the same binning as used in data are filled. The photons are corrected for conversions, and they have the same cuts applied to them as the real data has. From the invariant mass plots π^0s are counted using the same procedure as in data for each p_t bin. Once the reconstructed π^0s are counted in each p_t bin, then the number of π^0s that were actually generated by HERWIG are counted in each p_t bin giving the efficiency, $\frac{\#\pi^0(p_{t\ reconstructed})}{\#\pi^0(p_{t\ generated})}$. See figure 4.20 for the efficiency as a function p_t. The data count of $N_{\pi^0}(pt)$ is then multiplied by the reciprocal of this curve to give $N_{\pi^0}^{corr}$.

The rapidity distribution between data and Monte Carlo agree reasonably well, so that the efficiency is modeled in this variable. Refer to figure 4.16, and back ground subtracted distribution shown in figure 4.17

Asymmetry is defined for π^0s as

$$asymmetry = \frac{|E_{\gamma 1} - E_{\gamma 2}|}{E_{\gamma 1} + E_{\gamma 2}} \tag{4.25}$$

The energies are those measured by the LAC in the lab frame. In the center of mass frame of the π^0 the two γs are emitted back to back from the π^0 isotropic in θ, and ϕ with each photon carrying off equal amounts of energy, and equal and opposite momenta as depicted in figure 4.18. This is because the π^0 is a spin 0 meson. If one transforms the energy and momenta to the lab frame via a Lorentz transformation, the energy and momenta get rearranged such that the invariant mass, $m^2 = E^2 - p^2$, stays unchanged. So if the decay happens such that both photons are emitted perpendicular to the boost axis then the asymmetry would be zero since both photon's four vectors would transform the same way leaving them to still carrying away equal amounts of energy and momenta of the original π^0 in the lab frame. However, consider the case where the photons in the center of mass

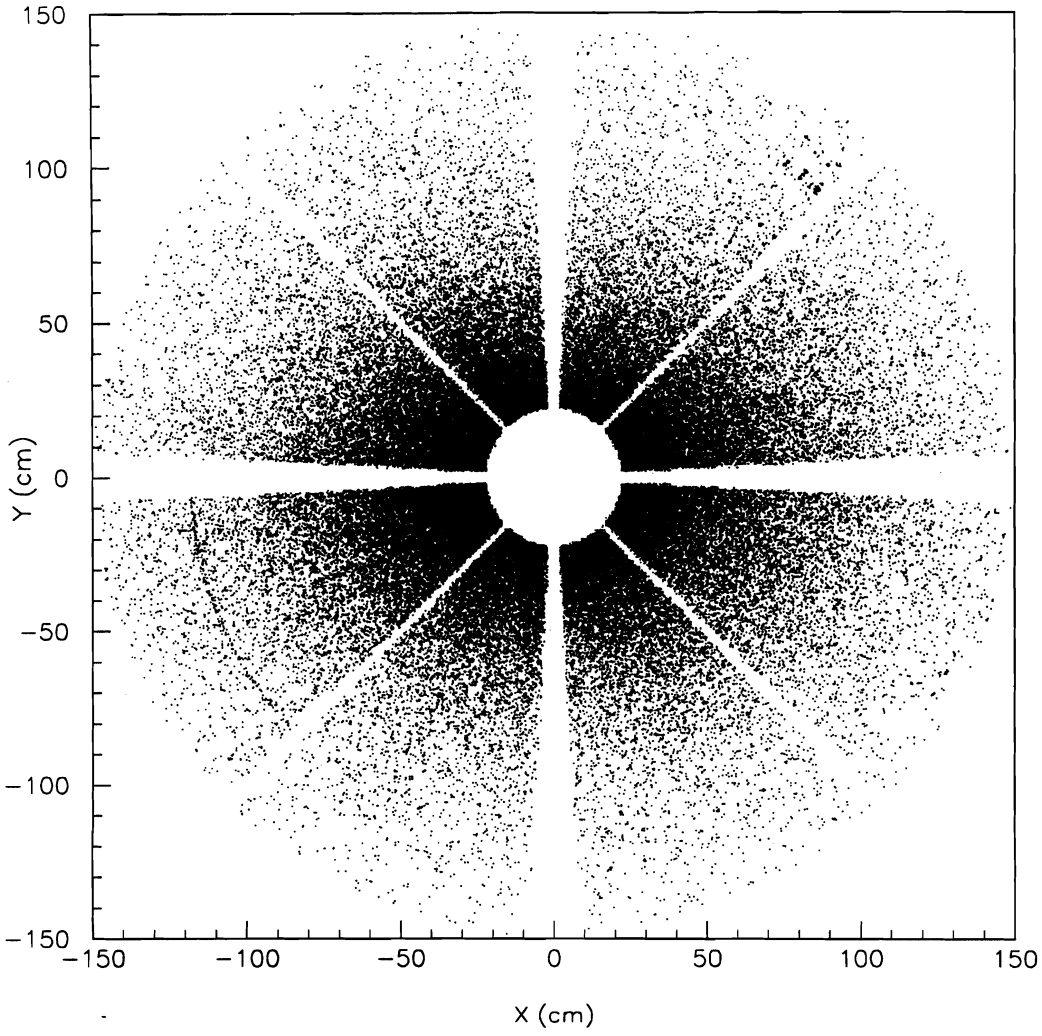

Figure 4.15: The photon x, y distribution across the face of the LAC with a fiducial cut applied on the octant boundaries. The quadrant boundaries are dead since this is where octants of the LAC are mechanically supported. Each quadrant is divided into octants, and the octants are read out at the quadrant boundaries.

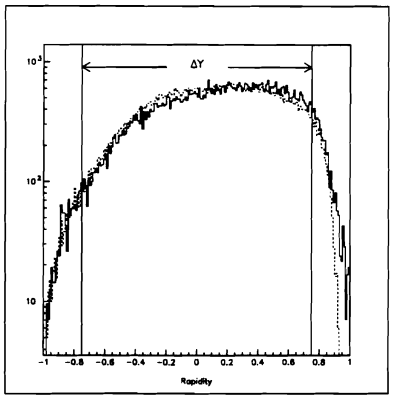

Figure 4.16: The reconstructed Rapidity of reconstructed two photon pairs. This plot is on mass pairs $.1 < m_{\gamma\gamma} < .2$ of both $\pi 0 s$ and background. Data (solid) and Monte Carlo (dashed)

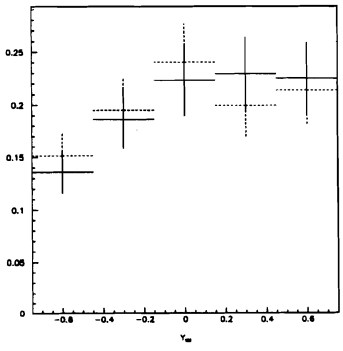

Figure 4.17: In this plot the area normalized reconstructed, background subtracted π^0 rapidity distributions between data (solid) and Monte Carlo (dashed) are shown.

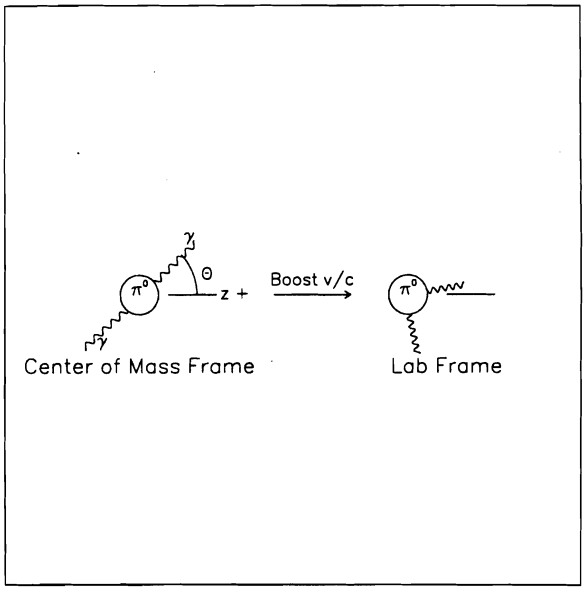

Figure 4.18: In the center of mass frame the two photons from a π^0 decay come of back to back with equal amounts of energy and momentum. In the lab frame the boost leads to an asymmetry in the energies of the two γs.

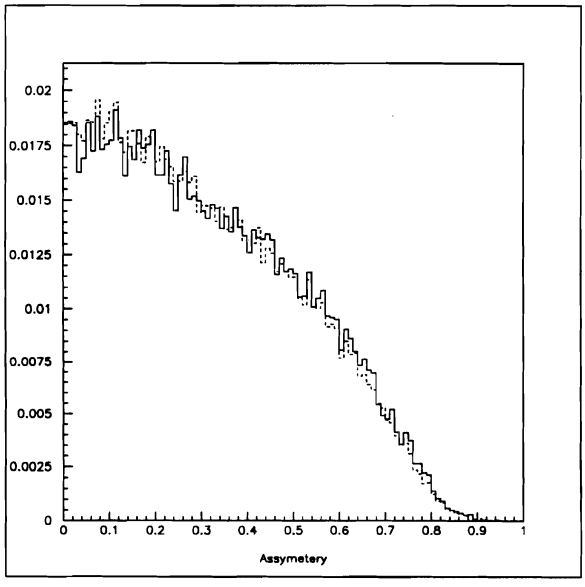

Figure 4.19: The reconstructed asymmetry of reconstructed two photon pairs. Data (solid) and Monte Carlo (dashed)

frame are emitted longitudinally with the original π^0 direction(say z): one with $+|p_{z\,cm}|$, and the other $-|p_{z\,cm}|$. Then, when the transformation to the lab frame is applied the photon emitted in the $+|p_{zcm}|$ will essentially have all the energy of the π^0, and the other photon will be very "soft" in the lab frame. Thus, the asymmetry for this case will approach unity. So for all other decay angles with respect to z the range on asymmetry is $0 \leq asymmetry \leq \frac{v}{c}$. as shown by equation 4.25. The LAC is insensitive to low energy photons and ones that are around 3 GeV or less cannot usually be resolved, or their energies reconstructed accurately so they are lost [25]. So the efficiency for highly asymmetric π^0 decays is low. If there were no losses a plot of asymmetry would look like a brick wall. However due to losses of low energy photons the asymmetry looks like fig. 4.19. The Monte Carlo reproduces this loss well, as shown superimposed on the data, thus one feels confident in integrating the efficiency over asymmetry.

4.2.3 Branching Fraction

In this thesis only the two γ mode of decay was examined. To correct for losses of $\pi^0 s$ caused by no detecting the other decay modes such $\pi^0 \rightarrow e^+e^-\gamma$, e^+e^-, etc., the yield of $\pi^0 s$ is multiplied by the reciprocal of the branching fraction of $\pi^0 \rightarrow \gamma\gamma$ of $\frac{1}{.98798} = 1.012166$.

4.2.4 Target Definition

To calculate the cross section for a given target, the yield of π^0s produced in the target is measured, and then normalized to number of beam particles incident on the target (corrected for beam adsorption). An interaction in the target is selected based upon the position of its vertex. The v_z, v_x, and v_y position determines in which target the interaction occurred. The cut on v_z is not tight around the physical positions of the target, because the resolution of the tracking system in $v_z(\approx .5mm)$. The longitudinal target definition is as shown in figure 4.21. Even

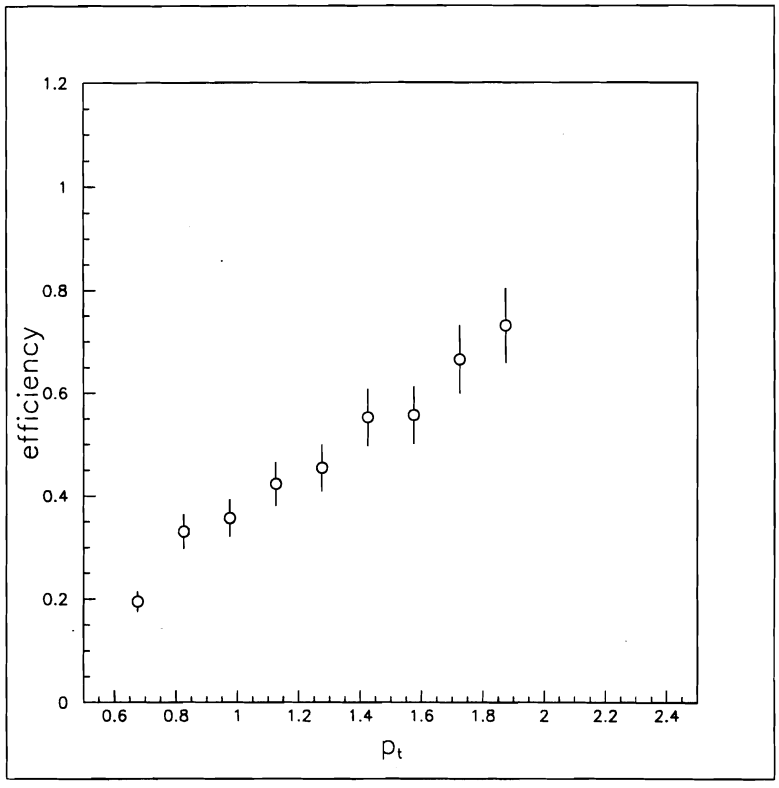

Figure 4.20: Efficiency calculated by running Monte Carlo through the analysis code. The correction to each data point is then the reciprocal of the efficiency.

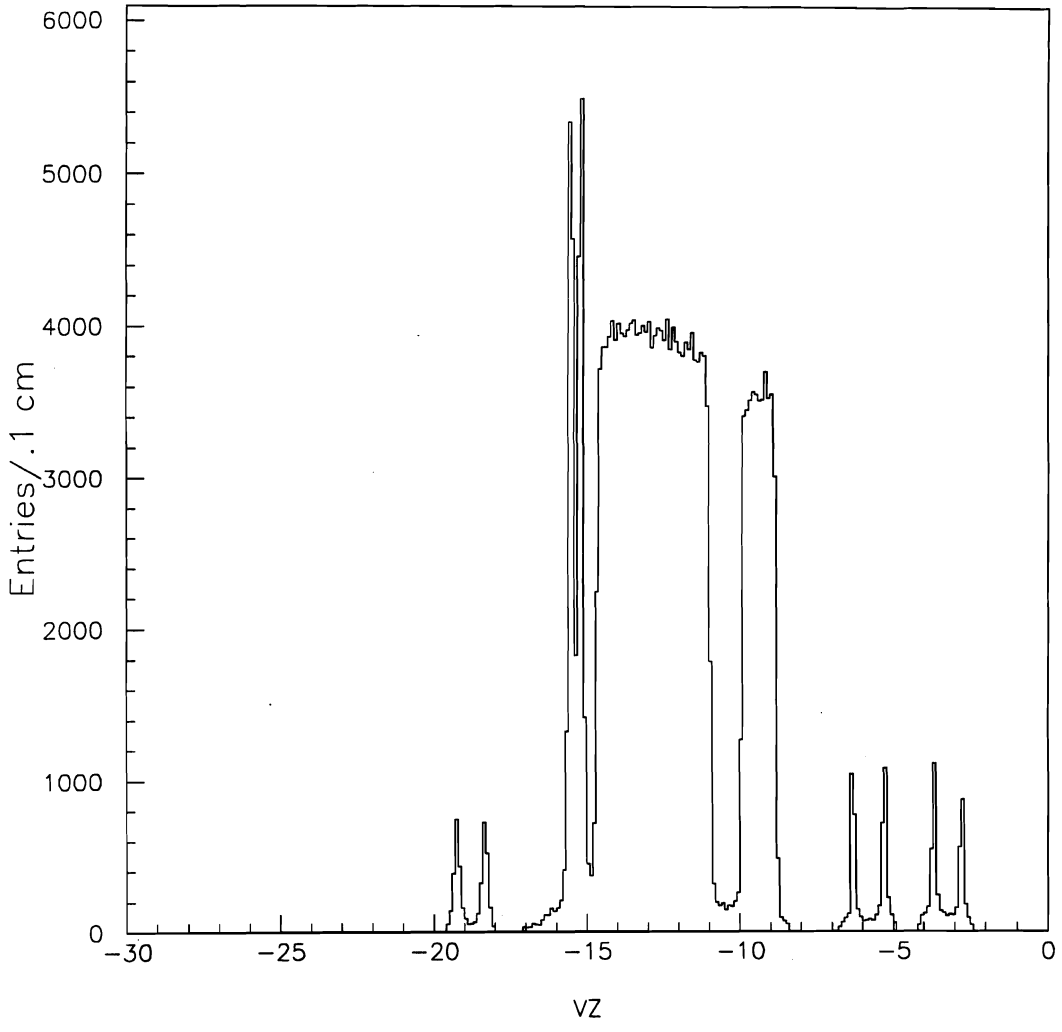

Figure 4.21: This is the vz distribution for Interaction data after the target longitudinal definitions have been applied in v_z.

with the loose definition of the target 2% of the vertices could still be lost due to the resolution in v_z of the reconstructor which could reconstruct a real target vertex outside of the target, and far enough away from the target to be cut out. The correction to data lost by the target cut is 1.02 [9].

4.2.5 Vertex Efficiency

Minimum bias events tend to have a small number of tracks produced in an interaction. Further more the tracks that are produced have a small opening angle; thus, the reconstructor can fail to find the vertex. If fewer than three tracks are produced then PLREC will not find a vertex by design (two lines can intersect somewhere, but that does not mean that this is the correct vertex position). If the opening angle is small, then the uncertainty in the vertex position is large in both x, and y views; thus, PLREC may not be able to link the two views together to establish a vertex position. Based upon the MC data it was found that 2% of generated vertices failed to reconstruct using HERWIG minimum bias events.

4.2.6 Beam Absorption Correction ABS

This is a correction on the normalization for beam absorption due to the thick targets. Ideally, one would like to have an infinitesimally thin target, but this would cause the data taking rate to be too low since there would be few scatters present. So the targets are made thick enough to give a good rate, but not so thick that they introduce numerous secondary interactions of the particles that are created in the primary collision. If one thinks of the thick target in terms of many thin targets of infinitesimal width dz, then it is clear that a given slice at the rear of the target will see less beam because of absorption of the beam due all the material in front of that slice. To do the correction, the absorption probability is calculated from the absorption cross section as

$$\textbf{BEAM ADSORPTION} = e^{\frac{-\Delta x}{\lambda}} \tag{4.26}$$

ΔX is the distance the beam particle traverses through a given material (targets, beam hodoscopes, etc). λ is the interaction length of the material. The correction for beam adsorption is the reciprocal of this quantity which is defined here as ABS given by

$$\mathbf{ABS} = e^{\frac{\Delta X}{\lambda}} \tag{4.27}$$

So in practice the ABS for each material between the beam hodoscope counting the beam and interaction point is calculated, the total ABS is the product of the ABS for each material as seen in equation 4.28

$$ABS = \prod_i e^{\frac{\Delta X_i}{\lambda_i}} \tag{4.28}$$

ΔX_i is the beam track length through the i^{th} material and λ_i is its corresponding interaction length. So for each two photon mass pair we weight its count with the above product which is typically around 1.05 for the Be target and 1.07 for Cu.

4.2.7 Corrected Beam Count

The way the beam trigger was installed into E706 it is possible to arrive at an absolute normalization for the beam triggers [15]. Beam triggers are taken every 15^6 trigger, and all that is required for beam triggers is that there be a BEAM signal from the beam hodoscope; thus, unbiased. In the beam triggers there are interactions $\approx$ 10% of the time. So one can extract π^0s from the beam that interacted, and then normalize that count to the total number of beam triggers; hence, calculate a cross section. There are corrections to this beam count.

Not all the beam that fires the beam trigger will be incident on the targets since the beam counting hodoscopes cover a larger area than do the targets. Also, the targets are not aligned with beam axis, therefore much of beam going into the spectrometer will miss the targets (see chapter 2 figure 2.3). Therefore, transverse fiducial cut on x, y was applied to define the targets in the x, y plane [8], and so this cut must also define the beam that is actually incident and available to interact

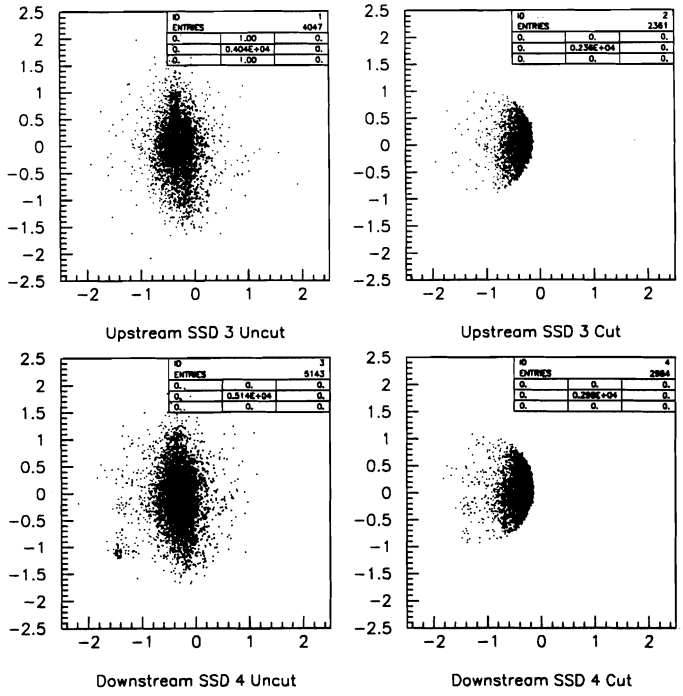

Figure 4.22: The reconstructed x, y hit distribution of interactions in the silicon micorstrip detectors. The upper two scatter plots are the SSD before the targets, and the lower two are for the SSD after the target. On the right hand side plots the target fiducial cut is applied to these hit distributions to get the ratio of beam incident on the targets to total incident beam. This ratio is 58% so the correction to the beam count is .58.

on the targets. To arrive at the transverse fiducial correction, interactions in the silicon microstrip detectors were studied, and the vertex distributions in x and y were studied these planes [15]. The SSDs were used because their large active area completely shadowed the beam profile and the targets. By looking at the number of interactions in the Si planes just before and after the targets, then applying the transverse target x, y fiducial cut to these distributions one gets the ratio of beam that is incident on the targets to the total beam. See figure 4.22 for the Si x, y scatter plots of Si before and after target fiducial cuts. This correction for the target fiducial cut in x, y is 58% or $.58 = \frac{1}{1.72}$ for the beam trigger.

Another correction to the beam count is multiple occupancy of beam particles

in a beam bucket. Two particles in the same bucket will fire one beam trigger, and be counted as one beam particle when in fact there are actually two particles that could interact. The beam hodoscopes were made of scintillating fingers so that multiple hits could be distinguished. By examining the ratio of single hits to multiple hits a figure of 10% multiple occupancy is arrived at; thus, the correction to the beam trigger count is 1.1 .

To avoid the multiple occupancy correction, one can look at only class the of events labeled BEAM1. These are events which contained only single beam particles in the triggering event. Recall that the beam hodoscopes had scintillating fingers arranged in an x,y view so that if there were no multiple cluster in the fingers then it could be assumed only one beam particle was present in a given RF bucket. The normalization of this class of events is simply the number of singly occupied BEAM1 events recorded by the experiment.

The absolute normalization for beam trigger data arrived at is

$$N_{beam}^{corr} = (number\ of\ beam\ triggers) \times \frac{1.1}{1.72} \tag{4.29}$$

or for BEAM1 data

$$N_{beam}^{corr} = (number\ of\ BEAM1\ triggers) \times \frac{1.0}{1.72} \tag{4.30}$$

To verify that the 10% double occupancy is indeed present in the beam structure, the cross section calculated from .NOT.BEAM1 (or $\overline{BEAM1}$) events was compared to the cross section calculated from the class of $BEAM1$ events. The cross section from the $\overline{BEAM1}$ was calculated and normalized to the number of $\overline{BEAM1}$ events. The $\overline{BEAM1}$ should all have at least two or more particles in the beam bucket that triggered the BEAM trigger. The correction to the normalization here should be two, but it is not applied to the normalization. The BEAM1 events should all be singly occupied by definition, and the normalization for this is the number of BEAM1 events. Thus the ratio of these cross sections should be at least a factor of two or larger. This ratio is shown in figure 4.23 and it indeed at

Cuts	Correction
target vz cut	1.02
Branching fraction	1.012166
Photon Conversions	function vz, vx, vy, θ, ϕ
Vertex Reconstruction	1.02
$\frac{efront}{etotal} > .2$ on each photon	MC Efficiency
LAC fiducial cut	MC Efficiency
Two γ Quadrant cut	MC Efficiency
$E_\gamma > 3.GeV$ on each photon	MC Efficiency
$0 \leq asymmetry \leq 1.$	MC Effieciency

Table 4.1: Cuts and corrections on two gamma $\pi^0 s$.

Correction Type	Correction
Target Fiducial Region	.58
Beam Absorption	1.054 (Be)
	1.007 (Cu)
Double Occupancy	1.1 (all data) or
Double Occupancy	1.0 (Class BEAM1 Events)

Table 4.2: Normalization correction applied to beam trigger count.

least two. Thus in calculating the cross sections then we use BEAM1 events for the beam trigger cross section, and INT1 events (INT1 is an interaction trigger which requires BEAM1) for the interaction trigger data so that a systematic introduced by a multiple occupancy correction is not introduced.

4.3 Results

4.3.1 Cross Sections

From DSTs, two photon mass histograms are made for each p_t bin, and corrections applied to the count of π^0s in each p_t bin as listed in table 4.1. Then the cross section is normalized by the corrected beam count as calculated in 4.2.

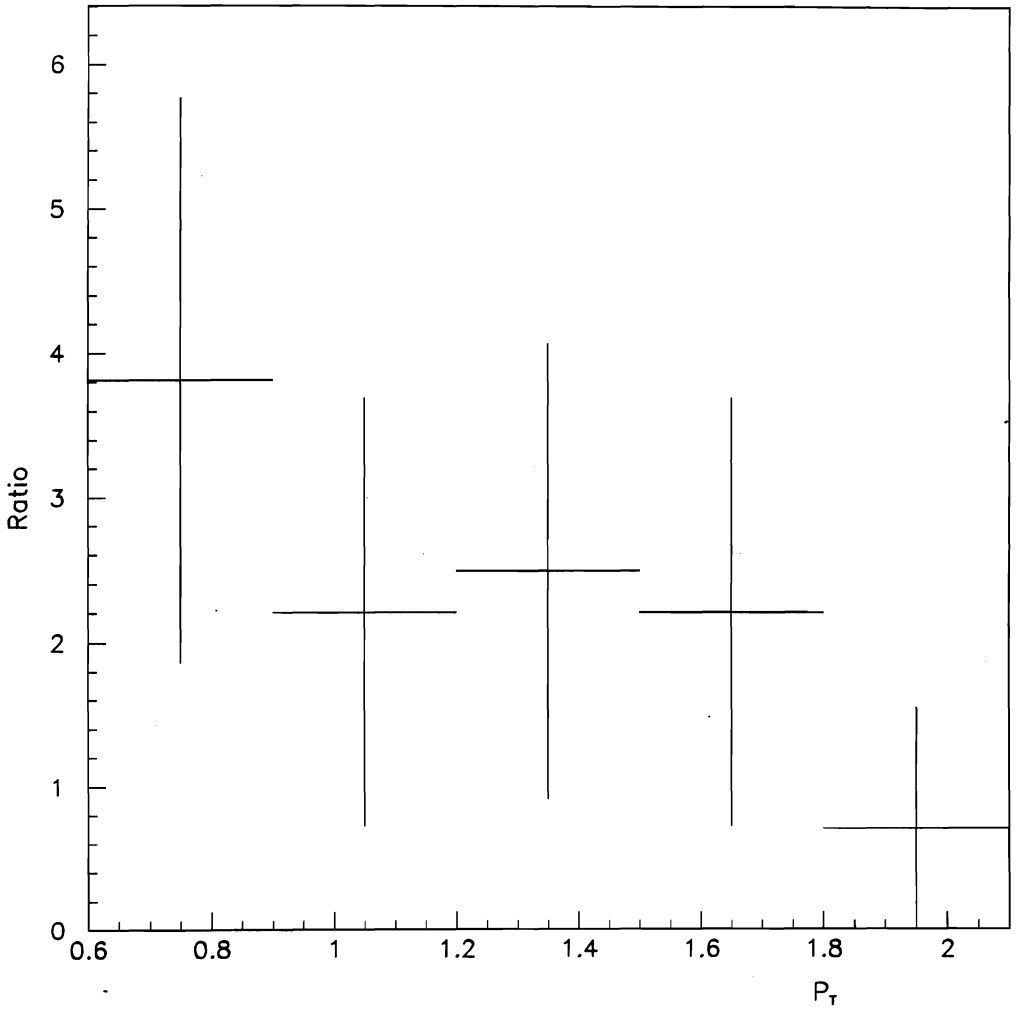

Figure 4.23: The ratio of the cross section calculated form the class of $\overline{BEAM1}$ events whose beam occupancy is > 1 particle to the class of BEAM1 events whose beam occupancy is one particle.

Since the data from the beam triggers is absolutely normalizable it is presented first. The limitation to this sample is statistics. The normalization is simply the events that satisfy the BEAM1 requirement corrected as in equation 4.30. figure 4.24 shows the cross-section and table A.1 in the appendix gives the values.

Next, the calculation is repeated for the interaction trigger data. Since the interaction trigger, by definition, requires an interaction it will be rich with π^0s. This is to be compared to the beam data sample where only $\approx$ 10% of the sample contained interactions.

In the case of the cross-section for the calculation of interactions on Be, events of the class INT1 trigger were used. These were singly occupied events. To normalize the interaction data the interaction fraction in the beam data was looked at. From the beam data, the ratio of BEAM1 to INT1 triggers in the targets was calculated and used to normalize the interaction trigger INT1 events. This was then corrected for the efficiency of a INT1 being fired if a BEAM1 type interaction occurred from the beam data. Other corrections to the normlization are applied as in 4.30. Corrections to π^0 counts for reconstruction efficiencies and photon conversions are then also applied as in the beam data case.

The figure 4.25 shows the cross sections for π^0 production of Be calculated for the BEAM1 and INT1 data compared, and figure 4.26 shows the ratio of the two cross sections. The ratio indicates that INT1 data is absolutely normalized with the BEAM1 data. Since the interaction sample is larger the cross section may be calculated in smaller p_t bins, and is show in figure 4.27 and tabulated in the appendix in table A.2. Comparing the minimum bias data to the high p_t triggered data of E706 is shown in figure 4.28. The normalization of the high p_t data is calculated in a different fashion than the low p_t data, thus the agreement between the two sets of data indicates that the cross sections are consistent.

The cross-section in the forward direction for $0. < Y_{cm} < .75$ was calculated and is shown in figure 4.29, and the results tabularized in A.3. The two cross-

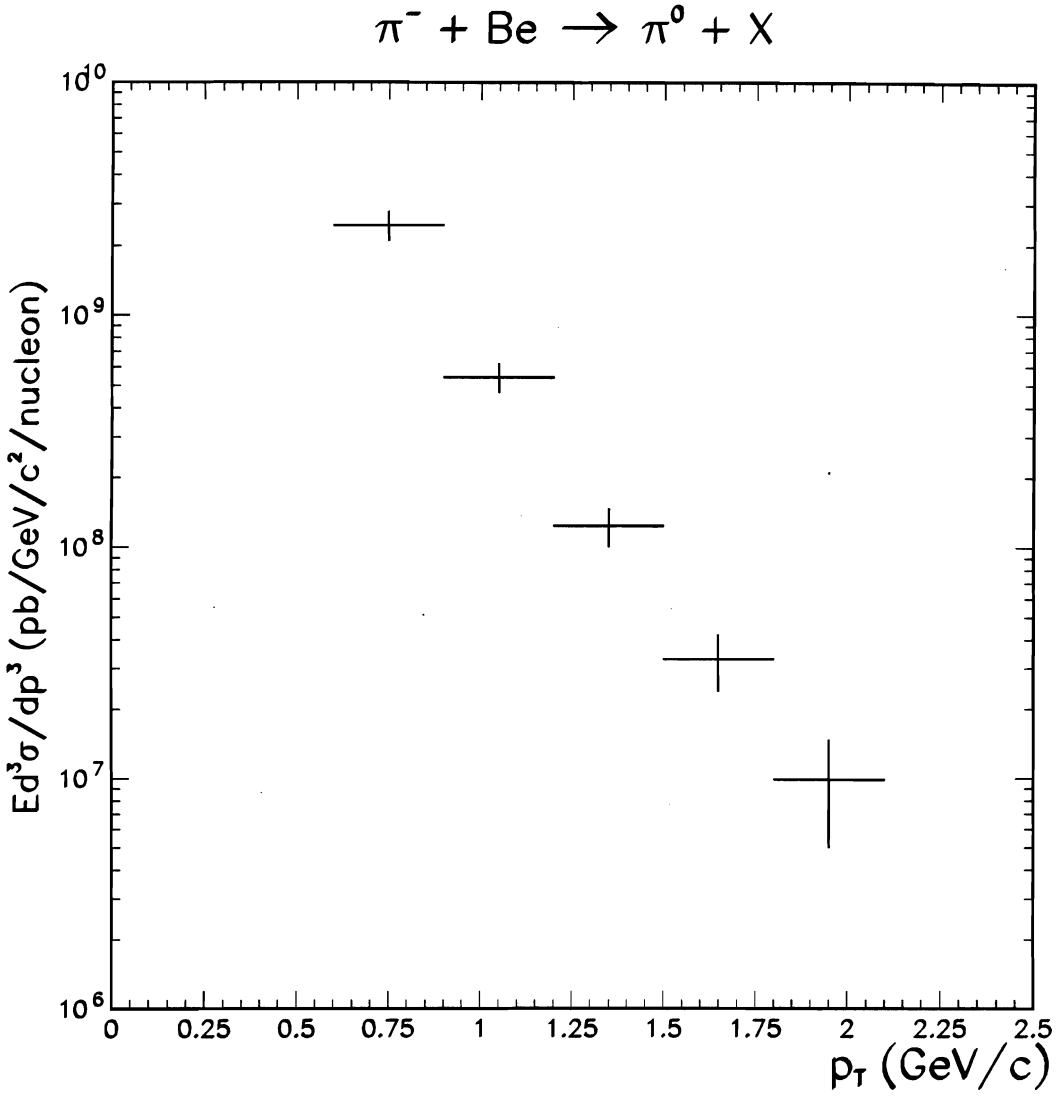

Figure 4.24: The invariant cross section from $-.75 < Y < .75$ for BEAM1 triggers normalized to the number of BEAM1 triggers. Uncertainties are statistical only.

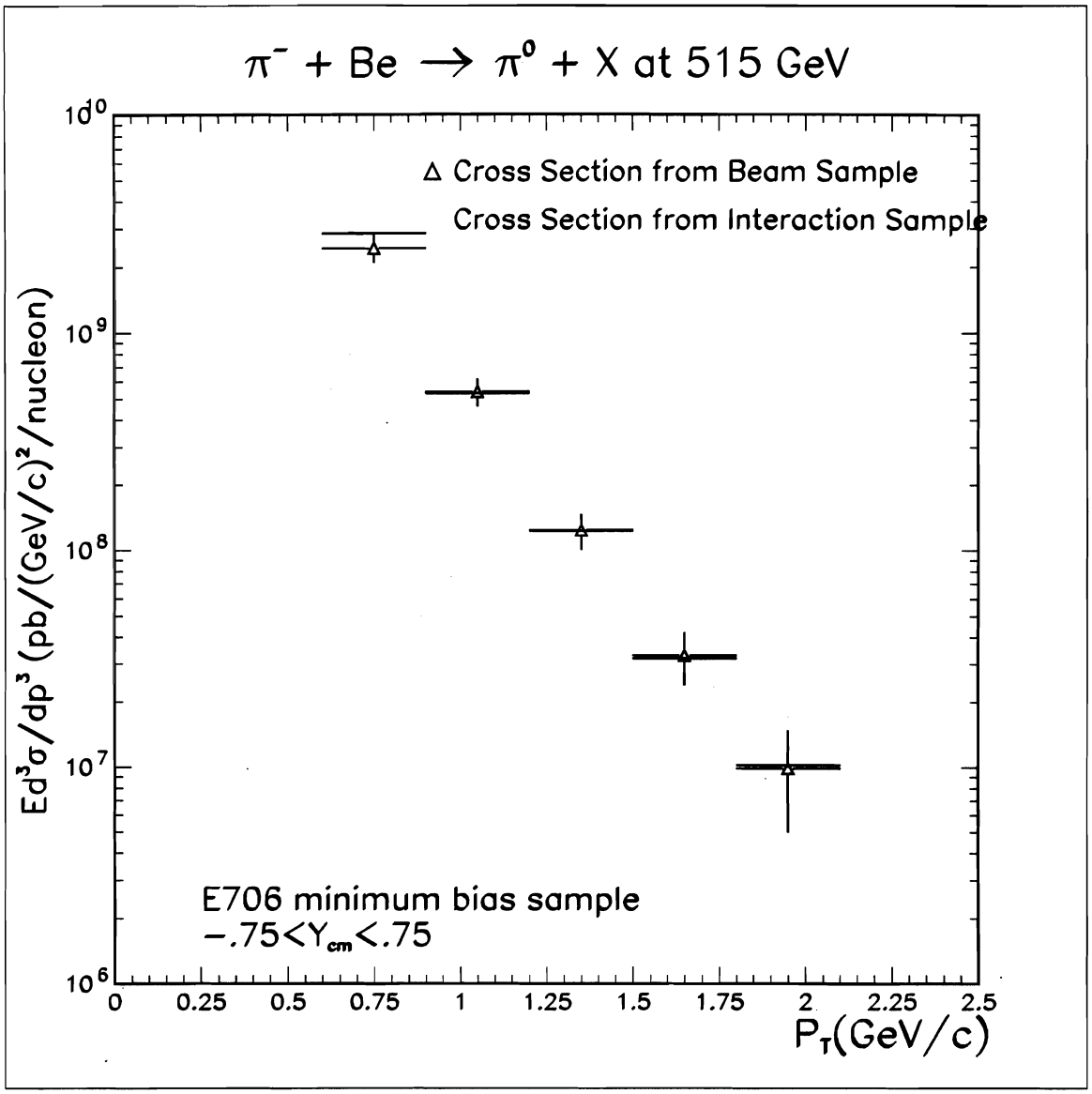

Figure 4.25: The cross section of determined from BEAM1 triggers compared to the cross section obtained from INTERACTION (INT1) triggers

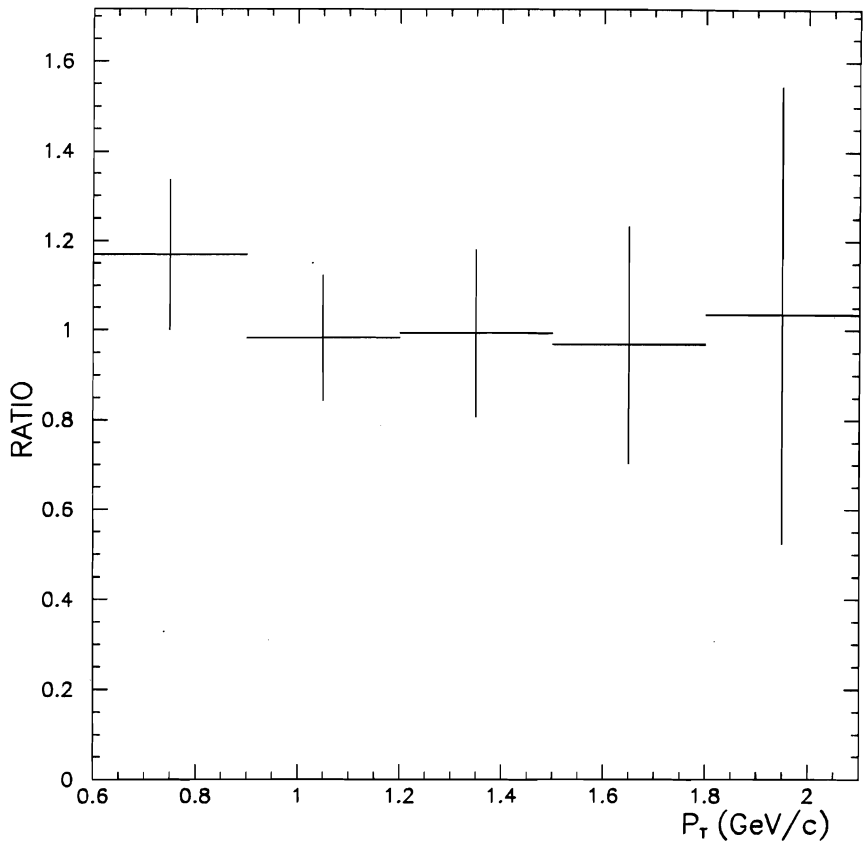

Figure 4.26: Ratio of the cross section calculated using the beam triggers to that calculated using the interaction triggers

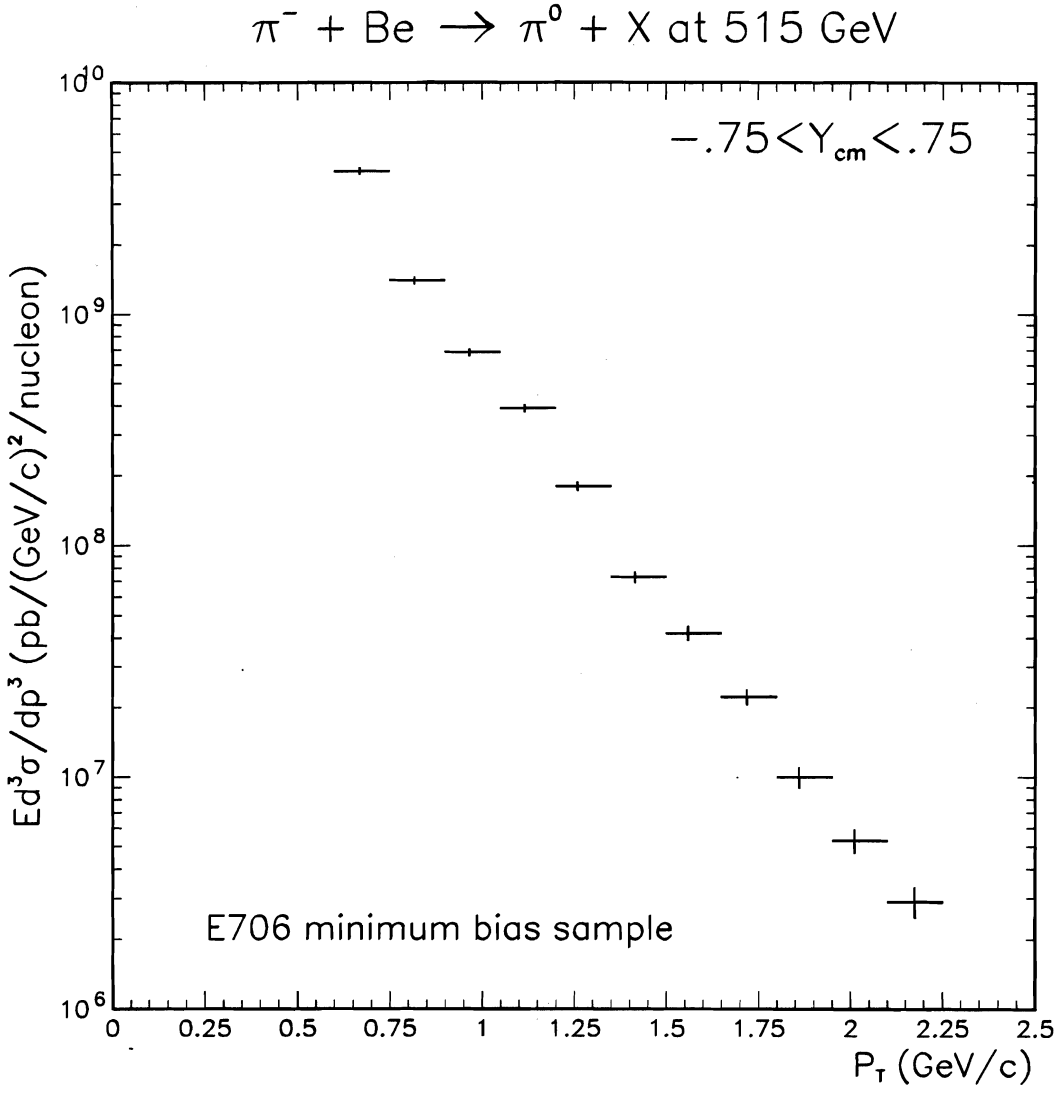

Figure 4.27: The invariant cross section from $-.75 < Y < .75$. Errors are statistical only.

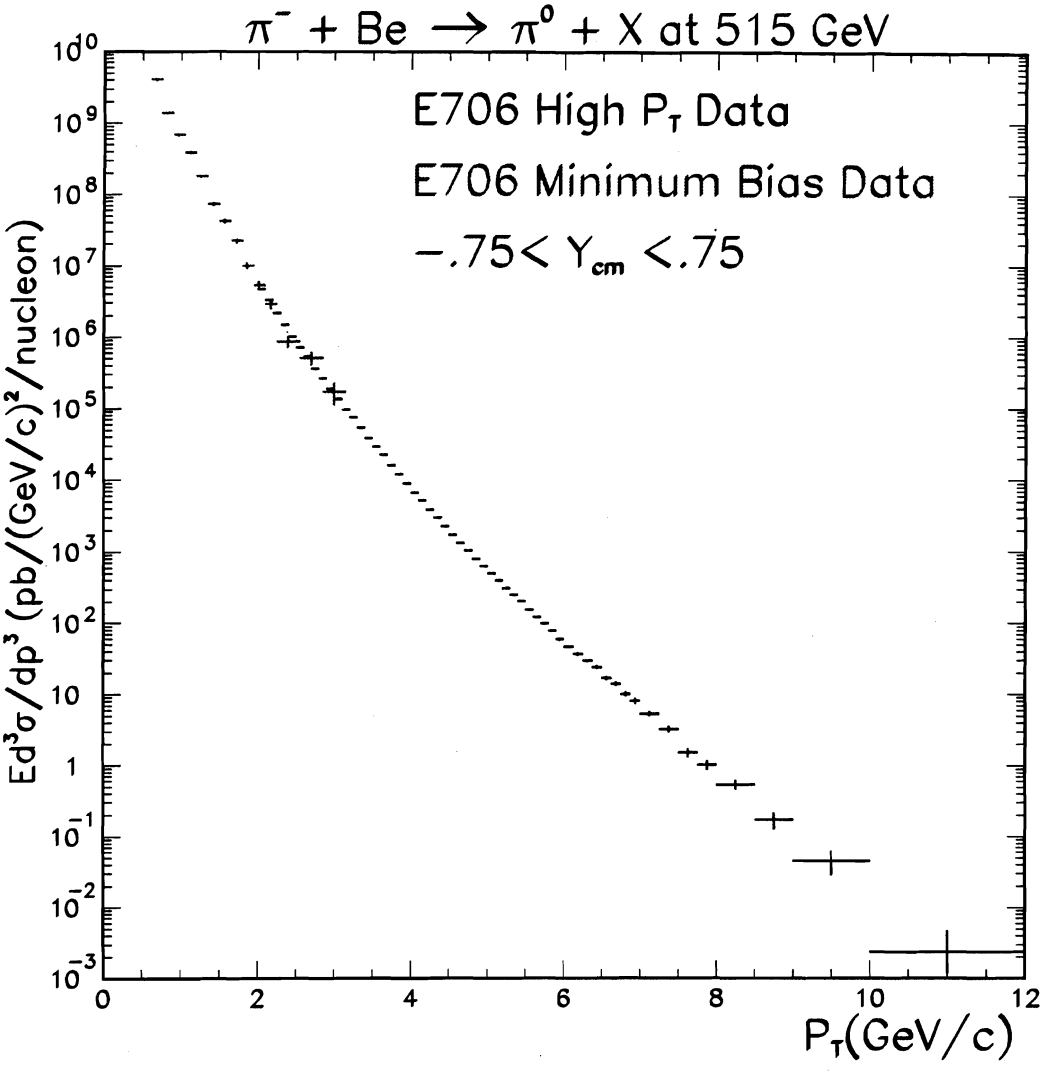

Figure 4.28: The invariant cross section compared to the rest of the triggers over $-.75 < Y < .75$. Uncertainties are statistical only.

sections are consistent within statistical, and systematic uncertainties.

The cross section for different rapidity bins, and fixed p_t bins was also calculated using equation 4.16 holding p_t fixed and varying Y_{cm}. Corrections for photon conversions, beam adsorption, and normalization are applied just as in the calculation as a function of p_t. The reconstruction efficiency as a function of rapidity in one of the p_t bins shown in figure4.30. The cross-section calculation is shown over different p_t intervals in terms of the rapidity Y is shown in figure

Following the same procedure as in the Be case the cross section or π^0 off of Cu is calculated and shown in 4.32. Values for the Cu cross section are tabulated in A.4. This cross section is to be compared with the Be cross section which is slightly higher even though both cross sections are calculated per nucleon. This due to the nuclear A dependence discussed section 4.5.

4.3.2 Uncertainties

In the measurement of the cross section there are statistical errors due to the finite sample size in each p_t bin, and systematic errors due to uncertainties in the corrections applied and in the normalization.

Statistical errors are taken as the $\sqrt{Signal\ +\ Background}$ counts of the unweighted spectrum. The percent error is $\frac{\sqrt{Signal\ +\ Background}}{Signal}$.

There are systematic uncertainties introduced by the fitting procedure. These are introduced by fluctuations in the background causing uncertainties in the fit, and by systematics in the background not described well by the fit. To estimate these errors the end points of the fits in each p_t bin was varied and the change in the cross-section was calculated. For the range $.6 < p_t < .9$ the error was $\approx 10\%$ in the cross section. For $p_t > .9$ the fit systematics were $\approx 1\%$. The large uncertainty at the low p_t end was caused by large background with a large curvature under the signal peak.

There is a systematic caused by an uncertainty in the energy scale. The un-

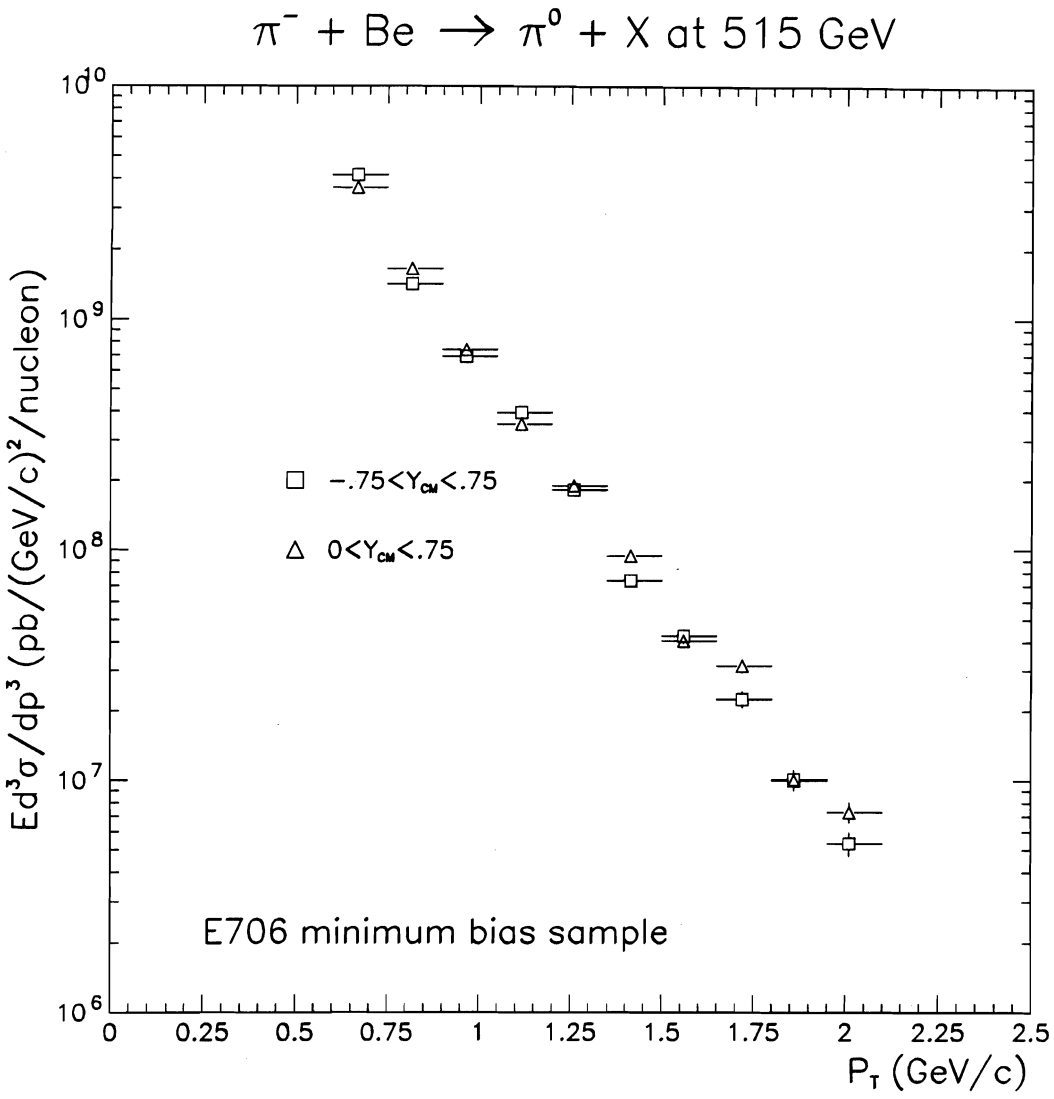

Figure 4.29: The invariant cross section in the forward direction from $0. < Y_{cm} < .75$ compared to the cross section over $-0.75 < Y_{cm} < .75$. Errors are statistical only.

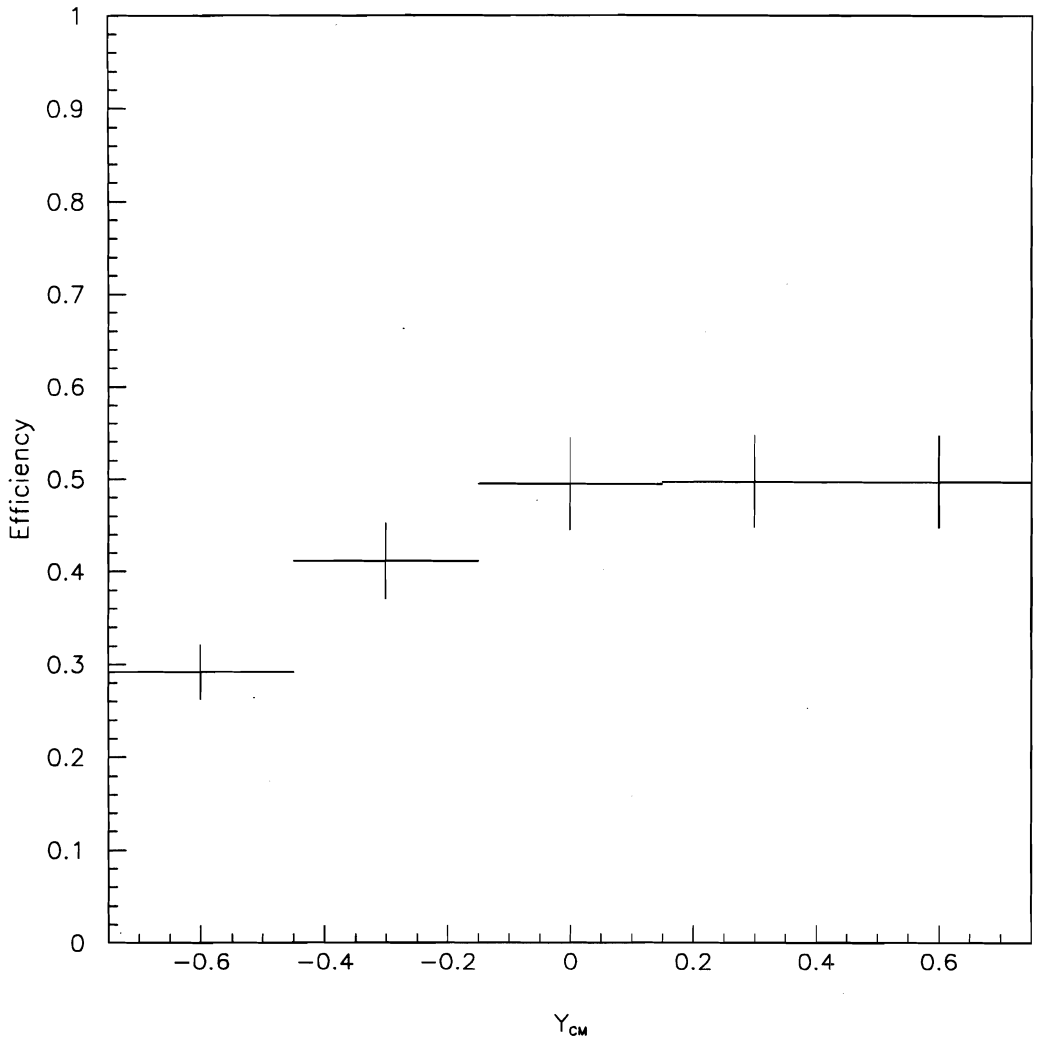

Figure 4.30: An efficiency curve for fixed $.9 < p_t < 1.5$ as a function of Y.

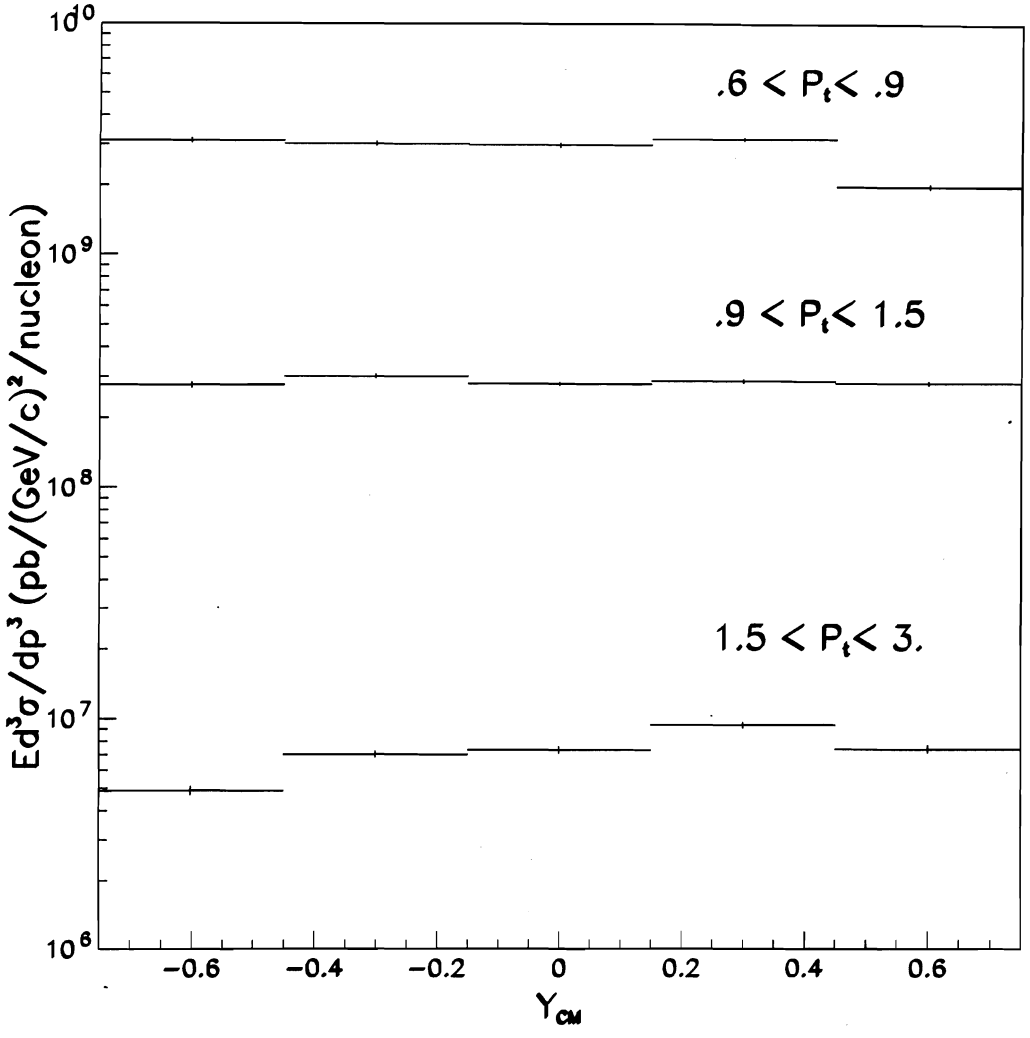

Figure 4.31: The invariant cross section calculated in fixed p_t bins over the rapidity Y. Errors are statistical only.

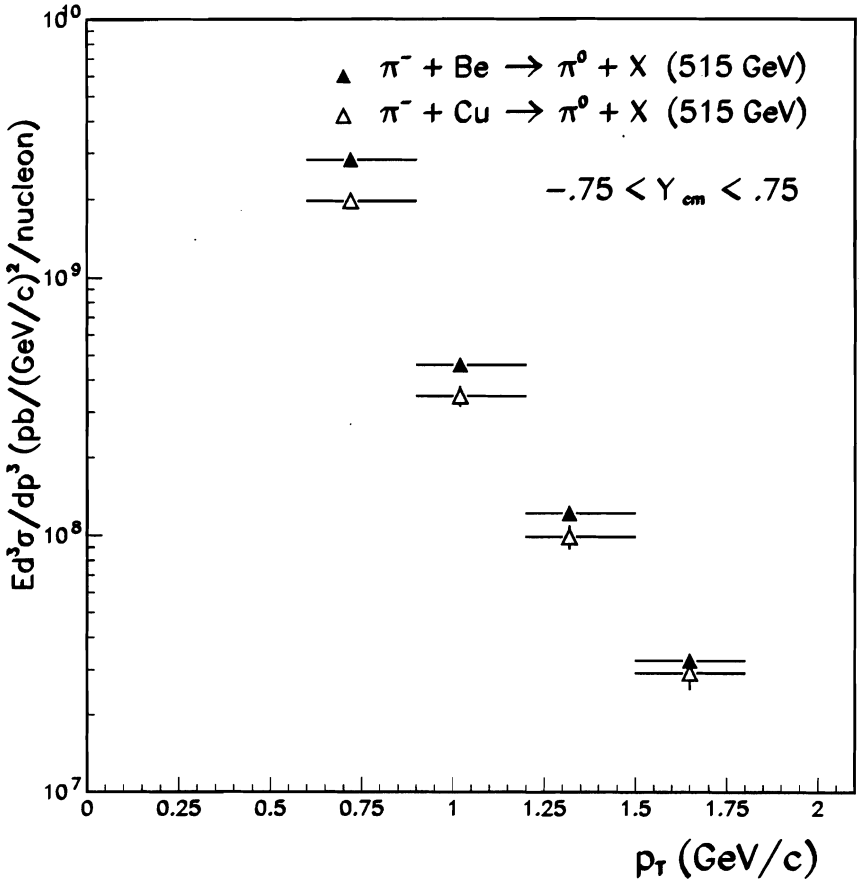

Figure 4.32: The invariant cross section from $-.75 < Y < .75$ of Be and Cu. The difference between these cross sections is related to the nuclear dependence $A^{\alpha-1}$. Errors statistical only.

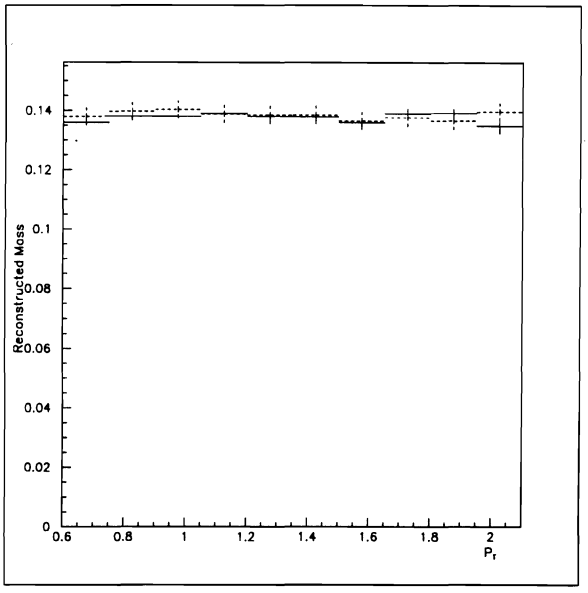

Figure 4.33: The Reconstructed mass of the π^0 measured in each p_t bin. The dash curved is the reconstructed Monte Carlo data.

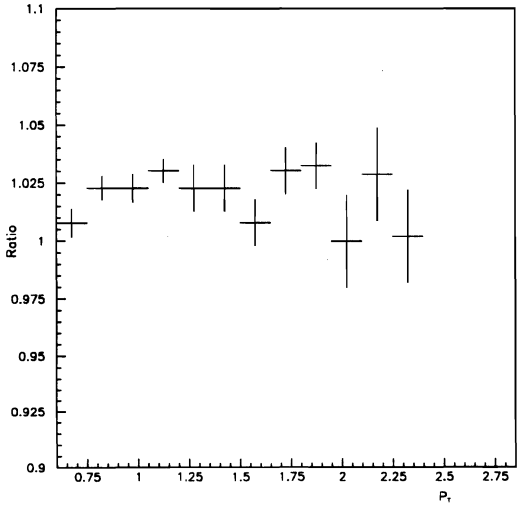

Figure 4.34: The ratio of the π^0 mass measured in each p_t bin compared the Particle Data Group's 0.13495 GeV/c^2 value.

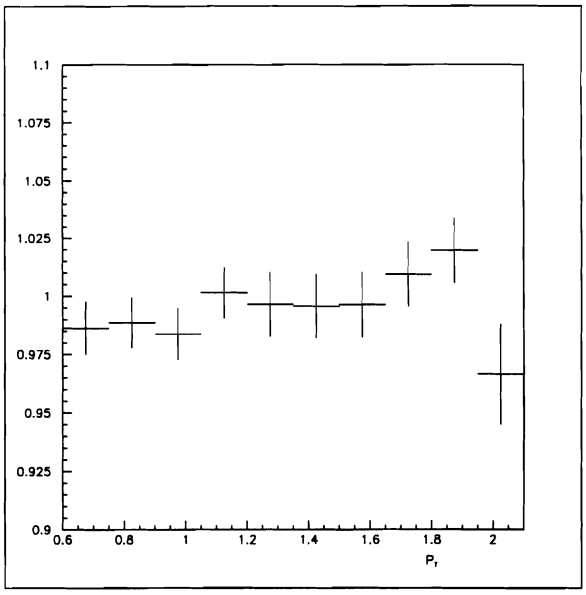

Figure 4.35: The ratio of the π^0 mass measured in each p_t bin compared the reconstructed Monte Carlo Data.

certainty in energy scale leads to an uncertainty in the determination of p_t, thus an uncertainty in the cross section. To investigate uncertainty introduced by the energy scale, consider the mass of the π^0 written in terms of the energies of the two photons from the decay, and their angle of separation in the laboratory frame.

$$m^2 = 2E_iE_j(1 - cos(\theta_{ij})) \tag{4.31}$$

varying m in terms of E_i and E_j and adding there variations in quadrature yields

$$\frac{\delta m}{m} = \frac{1}{2}\sqrt{(\frac{\delta E_i}{E_i})^2 + (\frac{\delta E_j}{E_j})^2} \tag{4.32}$$

Then $\frac{\delta E_i}{E_i} \approx \frac{\delta E_j}{E_j} \sim \frac{\delta E}{E}$

$$\frac{\delta m}{m} = \frac{\delta E}{\sqrt{2}E} \sim \frac{\delta p_t}{\sqrt{2}p_t} \tag{4.33}$$

since $p_t = E\sin(\theta)$ where here θ is the angle the π^0 makes with the z axis. Thus measuring deviations in the reconstructed mass gives deviation in the reconstructed p_t. To estimate this uncertainty, differences in the means of the reconstructed π^0 mass between Monte Carlo and data were calculated giving $\frac{\Delta p_t}{p_t} \approx 1\%$. To estimate

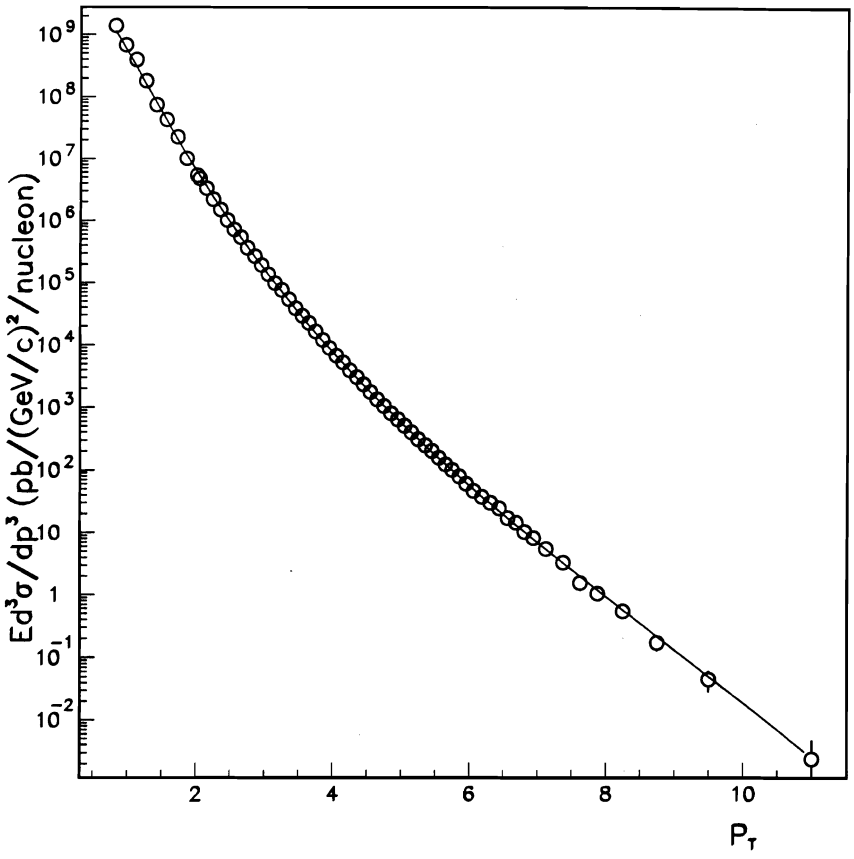

Figure 4.36: The cross section fit over the entire E706 range to the phenomenological form $(1-x_t)^m/(p_t^2+\delta^2)^n$

.

the uncertainty the cross section was fit with the phenomenological form of

$$E\frac{d\sigma}{dp^3} = C\,\frac{(1-x_t)^m}{(p_t^2+\delta^2)^n} \tag{4.34}$$

as shown in figure 4.36

The term $\frac{2p_t}{\sqrt{s}}$ is the transverse parton momentum fraction defined as x_t. The fit χ^2/DOF is 1.6 and the fit parameters are $C = 7.39E+10$, $m = 5.51$, $\delta = 1.21$, and $n = 5.05$. Then the percent uncertainty due to the energy scale is estimated as

error	percent
stat	calculated per bin
recon. eff.	10%
γ conversions	5%
beam normalization	1.5%

Table 4.3: Uncertainties in the cross sections

$$\frac{\delta E \frac{d\sigma}{dp^3}}{E \frac{d\sigma}{dp^3}} = \left(\frac{2m}{\sqrt{s}(1-\frac{2p_t}{\sqrt{s}})} + \frac{2np_t}{(p_t^2+\delta^2)}\right) \times \delta p_t \tag{4.35}$$

The uncertainty in the beam normalization due to the transverse correction is based on the SSD planes where the plane upstream, and closest to the targets. In the interaction triggered data, there were ≈ 4000 interactions used to determine the beam transverse fiducial cut, thus this gives 1.5% uncertainty on the normalization correction factor $\frac{1}{1.72}$

For the uncertainty in reconstruction efficiencies, 10% on each point was assigned due to Monte Carlo statistics and systematic uncertainties. This figure was estimated by calculating the cross-section in different Y and p_t cuts. From the Monte Carlo data new reconstruction efficiencies were calculated for the new cuts, then applied to the data. Then this cross section was then compared to the one previously obtained for differences related to reconstruction efficiencies. For photon conversions the estimated systematic is 5% due to uncertainties in material, and in the vertex position resolution.

Adding these errors in quadrature and taking the square root yields the total systematic error shown in last column of the table A.2 for the systematic uncertainties. The total error will be the statistical error and the systematic error added in quadrature for each bin.

4.4 Comparison with other Experiments

The results of E706 are of interest because they are of the highest $\sqrt{s} = 31.1\ GeV$ for nuclear targets. Higher $\sqrt{s}$ measurements have been made in colliders for pp collisions [27], but in these collisions the physics is different because of differences in the quark content of the colliding hadrons. The π^- has a valence anti-quark while the for pp collisions the anti-quarks must come from the sea quark distribution, thus the amplitude of the contribution from the annihilation diagram to the cross-section will be different. Comparison to previous fixed target experiments at a lower $\sqrt{s}$ is shown in figure 4.37 and on a larger scale in figure 4.38. Experiment NA27 [28] used a π^- beam incident on proton target which was a rapid cycling liquid hydrogen bubble chamber. The center of mass energy $\sqrt{s} = 26.0\ GeV$. The graph points used here came off of their fit form of $\frac{C}{p_t^2+\delta^2}$ on their data. NA24 [29] used a π^- beam incident on a hydrogen target. The acceptance they used in their measurement was $-.65 < Y_{cm} < .52$. Jim Cronin [2] used a variety of beams on variety of nuclear targets. Their result for their A dependence corrected per nucleon cross section calculation at 400 GeV was used in the comparison. Donaldson [30] used a 200 GeV p beam incident on a proton target and measured an invariant differential inclusive π^0 cross section. Frisch's data is from π^- collisions with a Be target and they measure the inclusive π^+ and π^- cross section with which the average of the two cross sections is plotted to compare with the π^0 cross section. The cross sections for other experiments have been scaled by our measured A dependence (except for Frisch which is reported for Be). The cross sections of the other experiments are observed to be lower than the measurement presented here. This is due to the lower $\sqrt{s}$ of the previous experiments. At lower $p_t \sim 0$ the cross sections as different center of mass energies may coalesce (although I do not claim that the data here demonstrates this), but as p_t increases the cross section increases dramatically as a function of $\sqrt{s}$.

In figure 4.39 the π^0 cross section for pp collisions at $\sqrt{s} = 30$ GeV is shown, scaled for the A dependence observed in E706, compared to E706 high p_t data. These two cross sections agree remarkably well.

The measurement in this thesis is compared to what was measured for the 1988 [31] data run of $\pi^- + \mathbf{Be} \rightarrow \pi^0 + \mathbf{X}$ and is shown in figure 4.40. The 1988 measurement is systematically low compared to the measurement presented here. In this thesis no attempt has been made to understand this.

In order to compare the cross sections at different $\sqrt{s}$, the cross sections can be recalculated using the scaling variable $x_t = 2\ p_t/\sqrt{s}$, which is the transverse momentum fraction. From equation 4.16 the p_t dependence comes in through the factor $\frac{N^{corr}_{pi^0}(p_t)}{p_t \Delta p_t}$. What we want to do is convert to $\frac{N^{corr}_{pi^0}(x_t)}{x_t \Delta x_t}$. Rebinning the counts observed in a p_t bin into a x_t bin follows from

$$N^{corr}_{pi^0}(xt)\Delta x_t = N^{corr}_{pi^0}(p_t)\Delta p_t \tag{4.36}$$

thus rewriting the cross section from x_t to p_t

$$\begin{aligned} \frac{N^{corr}_{pi^0}(x_t)}{x_t \Delta x_t} &= \frac{N^{corr}_{pi^0}(p_t)\frac{\Delta p_t}{\Delta x_t}}{x_t \Delta x_t} \\ &= \frac{N^{corr}_{pi^0}(p_t)\Delta p_t}{x_t (\Delta x_t)^2} \\ &= \frac{N^{corr}_{pi^0}(p_t)\Delta p_t}{(\frac{2}{\sqrt{s}})^3 p_t (\Delta p_t)^2} \\ &= (\frac{\sqrt{s}}{2})^3 \frac{N^{corr}_{pi^0}(p_t)}{p_t \Delta p_t} \end{aligned} \tag{4.37}$$

Thus the cross sections are plotted as a function of x_t and then scaled by the factor $(\frac{\sqrt{s}}{2})^3$ to convert the cross sections from the p_t dependence to the x_t dependence. The results are plotted in figure 4.41. Plotted in this fashion the results of our measurement compared with other peoples measurements appears to be agreement, with still the exception at the lower $\sqrt{s}$ values. Deviations from scaling could be dependent on Q^2 effects related to different $\sqrt{s}$ collisions.

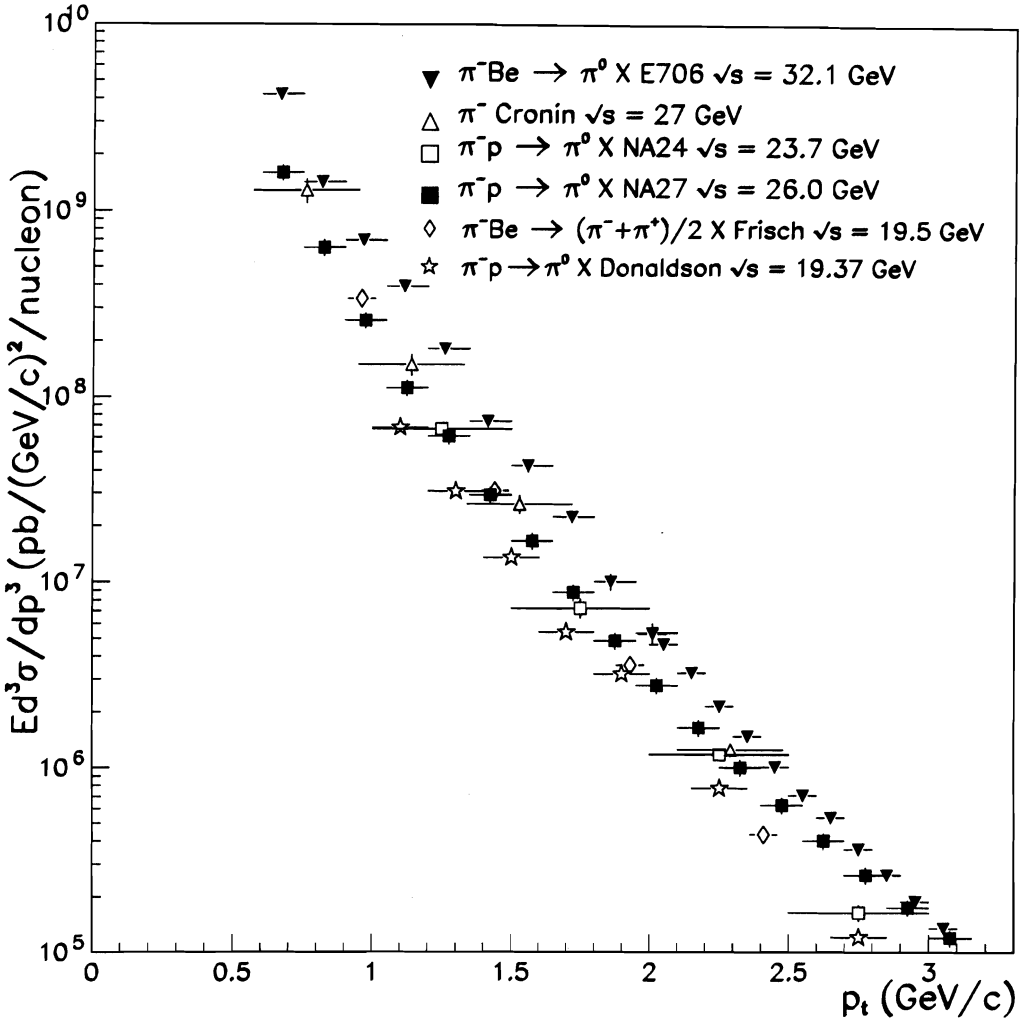

Figure 4.37: The E706 minimum bias data compared to other fixed target experiments. The other experiments have been scaled by the observed A^α dependence. The Cronin result is their quoted result per nucleon corrected for their observed **A** dependence, then scaled to the E706 **A** dependence for **Be**

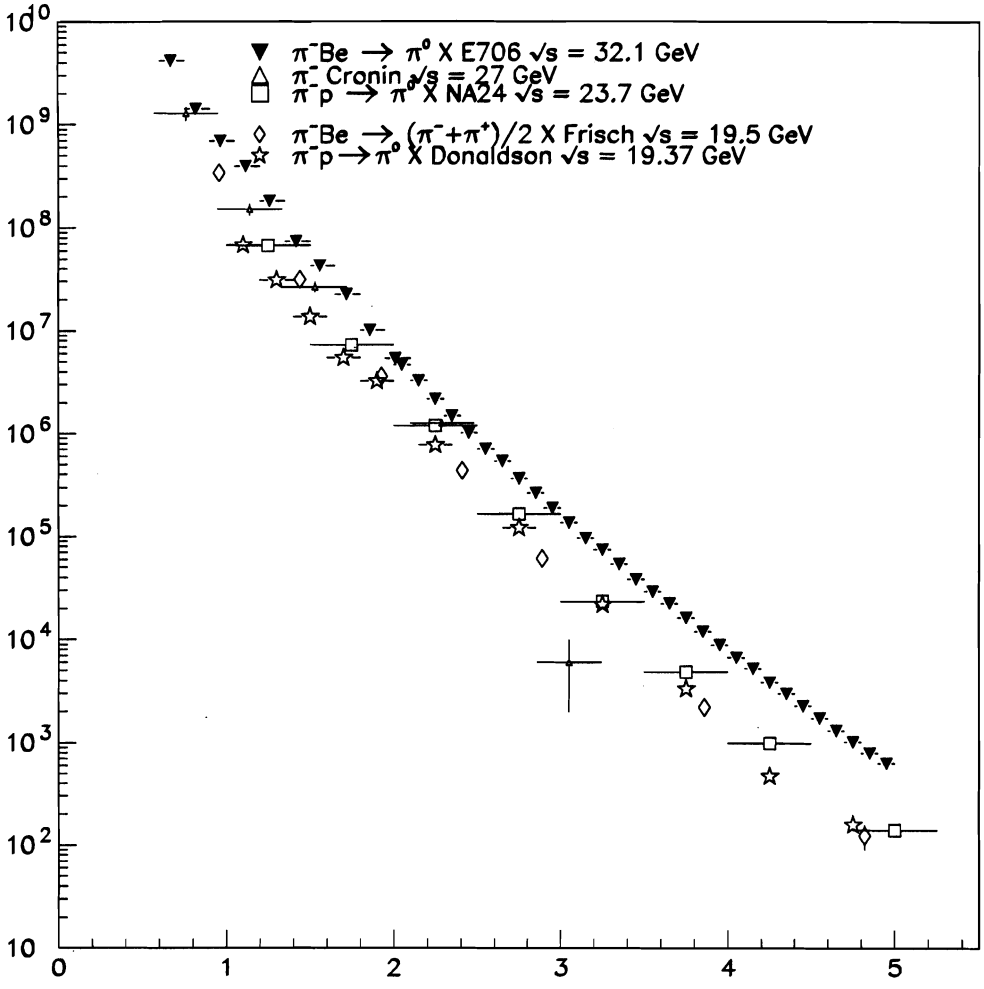

Figure 4.38: This is the same at the previous plot except that a larger scale in p_t is shown.

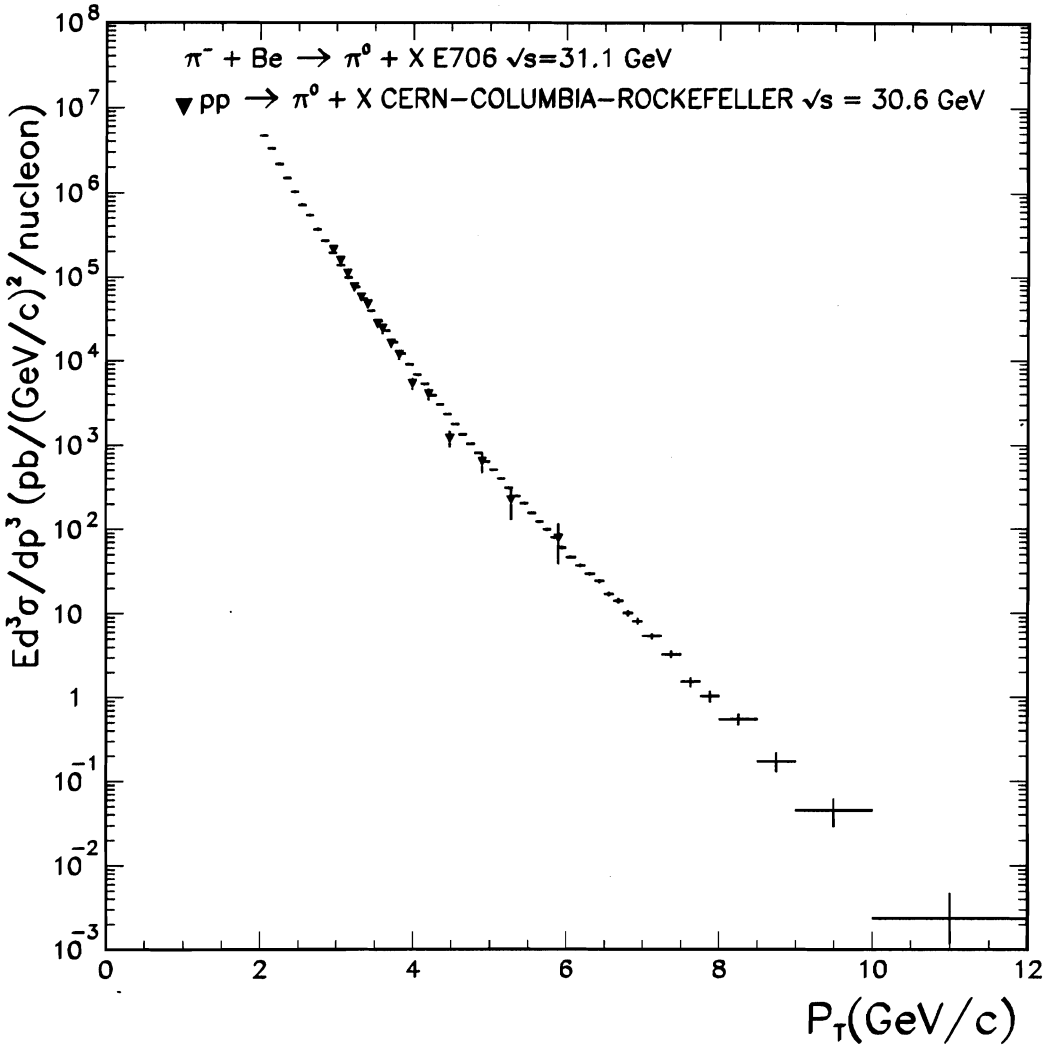

Figure 4.39: The E706 high $p_t$data compared to other fixed target experiments. The pp results have been scaled by the observed A^α dependence.

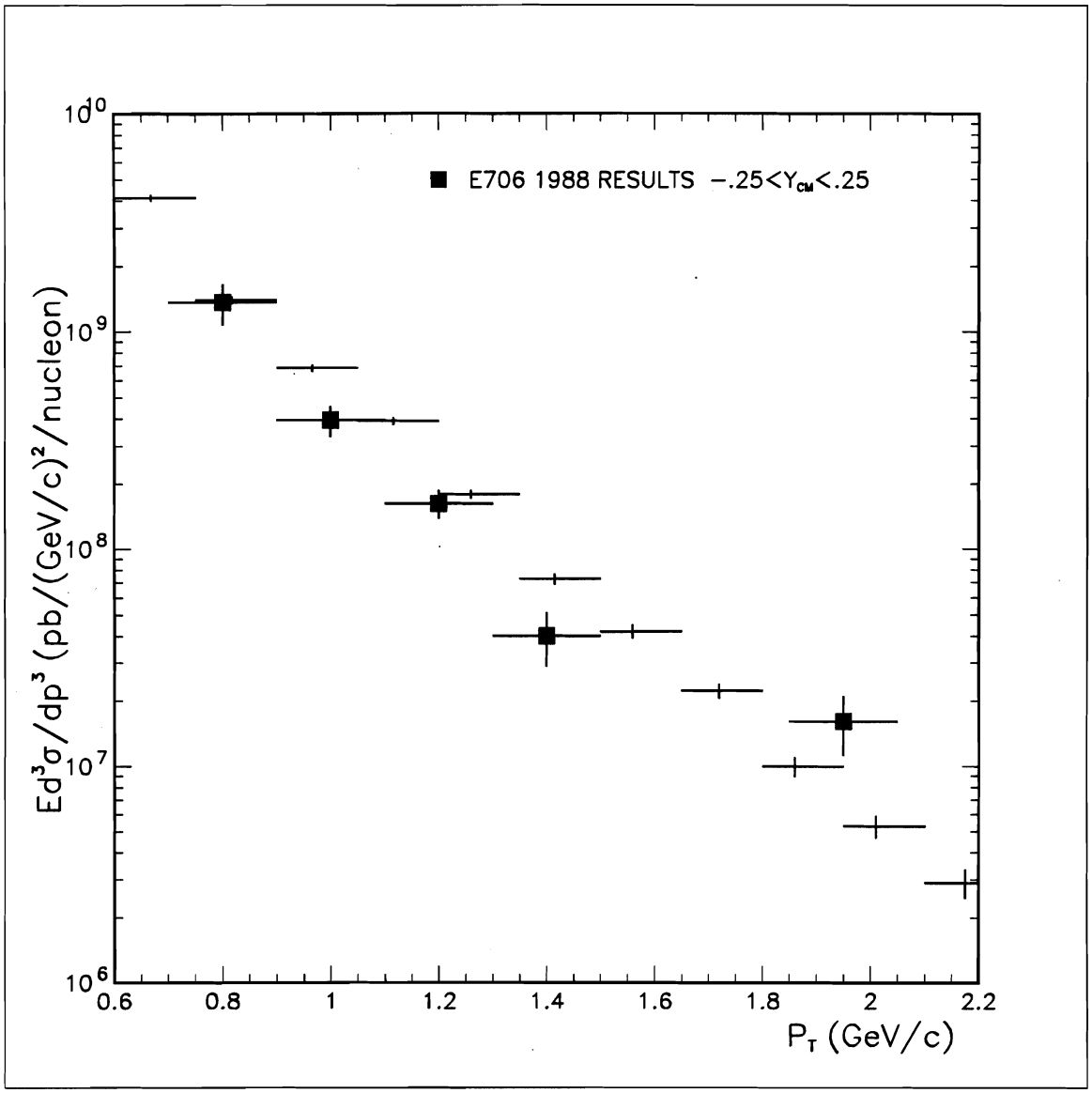

Figure 4.40: The cross section of this thesis compared to what was calculated for the 1988 run.

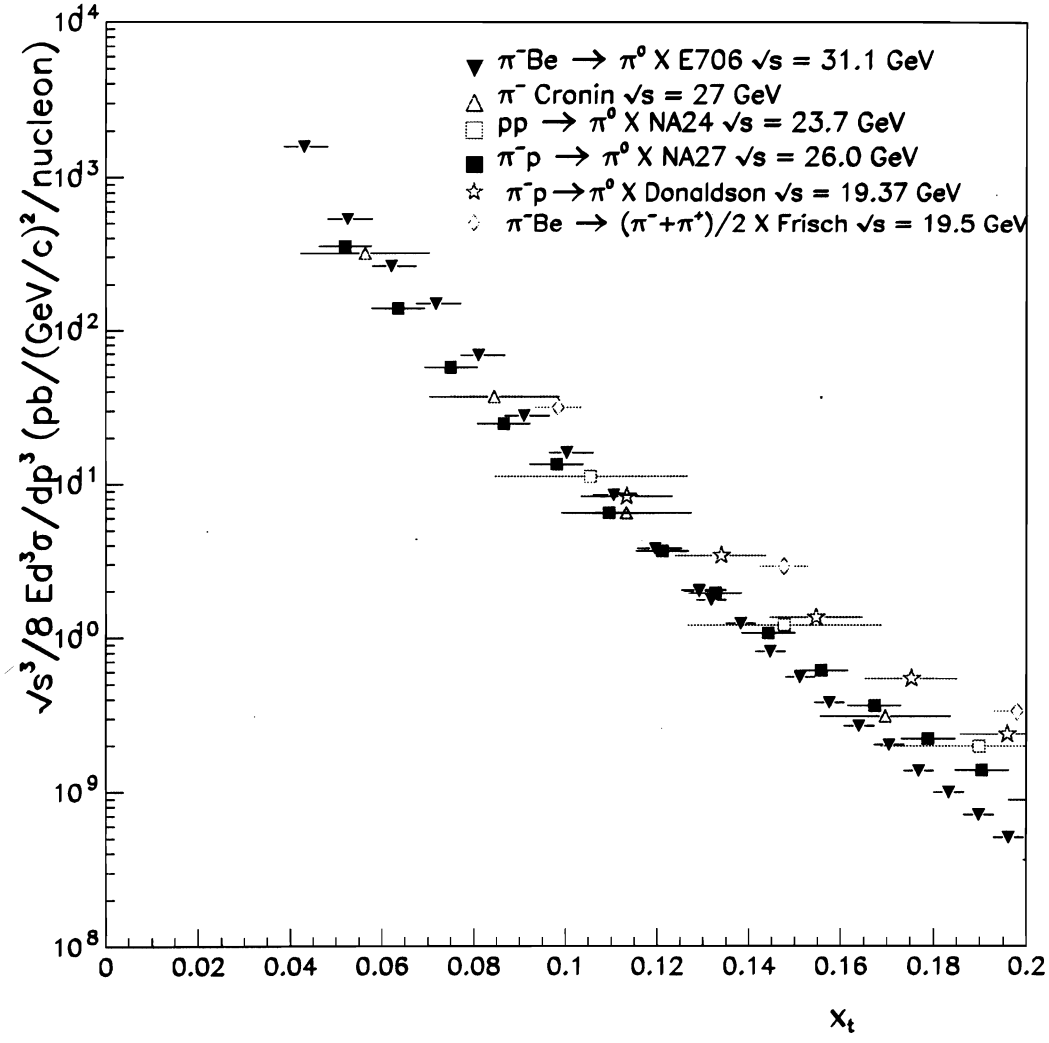

Figure 4.41: The compared cross sections in terms of the scaling variable x_t.

4.5 Nuclear Dependence

The QCD hard scattering of the π^- meson takes place off of the nucleons in the nucleus, but since these nucleons are not free the nucleus does effect the scattering process. The cross section of pion production off of nuclear targets may be parameterized as

$$\sigma_{A/nucleon} = \sigma_0 A^{\alpha-1} \tag{4.38}$$

By taking the ratios of cross sections measured on Be, and Cu one can remove the σ_0, and determine α [19].

$$\alpha = 1 + \frac{ln(\frac{\sigma_{Cu}}{\sigma_{Be}})}{ln(\frac{A_{Cu}}{A_{Be}})} \tag{4.39}$$

The result of this calculation is shown in figure 4.42 Comparing to the high p_t calculation it is seen that the A dependence behaves as one would naively expect. Namely at low p_t ($p_t \sim 0$) α should be $\approx 2/3$ where the scattering scales as if it is taking place off a flat nuclear disk ("nuclear shadowing"). As p_t increases the scattering is getting harder taking place off the nucleons themselves. At high p_t α is expected to exceed unity due to rescattering within the nucleus smearing out the p_t spectrum of the resulting hadrons. This measurement is compared against previous measurements as shown in fig 4.43 .

Performing the error propagation on α yields

$$\delta\alpha^2 = \frac{1}{ln(\frac{A_{Cu}}{A_{Be}})}((\frac{\delta\sigma_{cu}}{\sigma_{cu}})^2 + (\frac{\delta\sigma_{be}}{\sigma_{be}})^2) \tag{4.40}$$

The largest source of uncertainty comes from the copper cross section. Only the statistical errors of the cross-sections were used for the uncertainties in the cross sections, since the systematics are assumed to cancel out in the ratio for α.

4.6 Conclusion

In this thesis the cross section and α dependence are measured at the low p_t end of E706's capabilities for π^- collisions on the nuclear targets of beryllium and

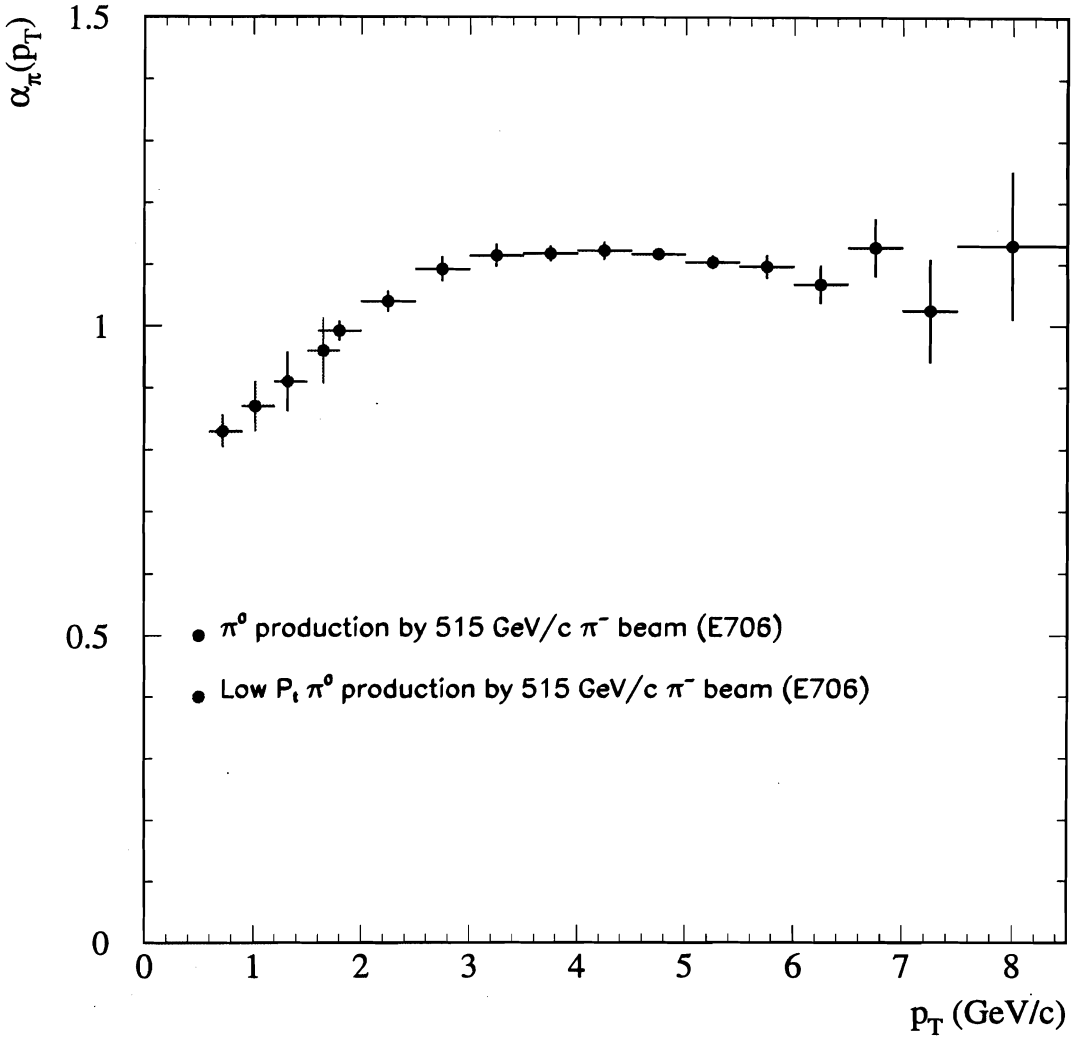

Figure 4.42: The nuclear dependence parameter α for π^0 production off of nuclear targets.

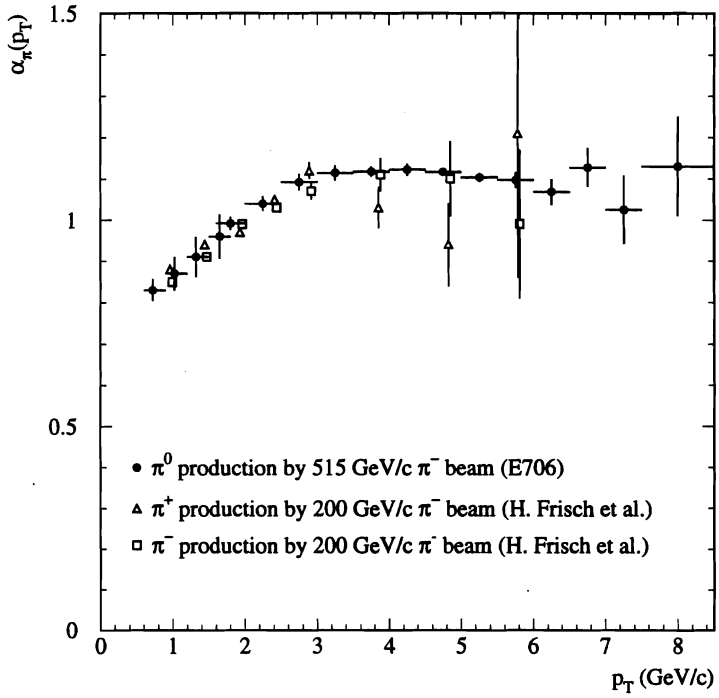

Figure 4.43: The nuclear dependence parameter α compared to other measurements.

copper, thus increasing the coverage of E706. This measurement provides data at a higher $\sqrt{s}$ for nuclear collisions than previously measured. The cross section measurement is consistent with the high p_t measurement thus demonstrating that the high p_t cross section is absolutely normalized. This was a crucial cross check against strange biases that could have been introduced by the high p_t triggers needed to make the large p_t direct photon measurement.

The measurement compares well with other experiments corrected for the nuclear A^α dependence. The cross section is seen to increase as function of $\sqrt{s}$. At larger p_t the production of $\pi^0 s$ is even more copious than for measurements made at smaller $\sqrt{s}$ suggesting that for the phenomenological dependence of $\frac{1}{p_t^n}$, n scales in $\sqrt{s}$.

The α dependence measurement extends the high p_t measurement down into the low p_t region where the dependence is a strong function of p_t. This measurement is consistent with previous measurements of α. No attempt will be made to interpret the α dependence other than to say that at low p_t the nucleus acts in a collective fashion leading to cross sections scaling in A as if they are scattering off of a black nuclear disk. At high p_t the scattering is indeed taking place off of the nucleons, but due to rescattering inside the nucleus smearing the p_t spectrum, there is an enhancement in the cross section. Other exotic theories such as "color transparency" exist, but at this point in time those models are speculative.

Appendix A

Tables of Cross Sections

$p_t(GeV)$	XS ($\frac{pb}{(GeV/c)^2}$)
0.750	1.956e+09 ± 2.834e+08
1.050	4.332e+08 ± 6.179e+07
1.350	9.915e+07 ± 1.868e+07
1.650	2.636e+07 ± 7.208e+06
1.950	7.923e+06 ± 3.907e+06

Table A.1: The invariant cross section from $-.75 \leq Y \leq .75$ for **BEAM1** triggers. Uncertainties are statistical only.

$p_t(GeV)$	XS ($\frac{pb}{(GeV/c)^2}$)	fit syst.	energy scale syst.	total systematics
$0.668^{+0.068}_{-0.082}$	4.178e+09 ± 1.4e+08	7.8 %	3.7 %	14.2 %
$0.817^{+0.067}_{-0.083}$	1.416e+09 ± 5.2e+07	9.9 %	4.9 %	15.8 %
$0.966^{+0.066}_{-0.084}$	6.916e+08 ± 2.8e+07	8.1 %	4.3 %	14.5 %
$1.116^{+0.066}_{-0.084}$	3.936e+08 ± 1.4e+07	5. %	5.1 %	13.4 %
$1.260^{+0.060}_{-0.090}$	1.817e+08 ± 8.2e+06	2.8 %	6.6 %	13.4 %
$1.415^{+0.065}_{-0.085}$	7.369e+07 ± 4.1e+06	1. %	7.3 %	13.5 %
$1.560^{+0.060}_{-0.090}$	4.235e+07 ± 3.0e+06	1. %	7.9 %	13.8 %
$1.720^{+0.070}_{-0.080}$	2.248e+07 ± 1.7e+06	1. %	8.4 %	14.1 %
$1.860^{+0.060}_{-0.090}$	1.008e+07 ± 1.0e+06	1. %	8.9 %	14.4%
$2.010^{+0.060}_{-0.090}$	5.355e+06 ± 6.4e+05	1. %	9.3 %	14.6 %
$2.175^{+0.075}_{-0.075}$	2.925e+06 ± 4.4e+05	1. %	9.7 %	14.9%
$2.400^{+0.150}_{-0.150}$	8.734e+05 ± 1.6e+05	1. %	10.2 %	15.3%
$2.700^{+0.150}_{-0.150}$	5.171e+05 ± 1.0e+05	1. %	10.8 %	15.6 %
$3.000^{+0.150}_{-0.150}$	1.739e+05 ± 6.10e+04	1. %	11.3 %	16.0 %

Table A.2: The cross section for π^- + **Be** $\rightarrow$ π^0 + **X.** The first column is the mean p_t in each bin. The second column is the cross section with statistical errors. The third columun is the systematic error in the fit for each bin. The fourth column is the systematic caused by the uncertainty in the energy scale. The last column is the overall systematics added in quadrature including the 10% for the Monte Carlo, 5% for the conversion probabilities, and 1.5% for the normalization transverse fiducial cut correction.

$p_t(GeV)$	XS ($\frac{pb}{(GeV/c)^2}$)	fit syst.	energy scale syst.	total systematics
$0.668^{+0.068}_{-0.082}$	3.681e+09 ± 1.1e+08	7.802 %	4.3 %	14 %
$0.817^{+0.067}_{-0.083}$	1.648e+09 ± 5.4e+07	9.925 %	5.5 %	16 %
$0.966^{+0.066}_{-0.084}$	7.402e+08 ± 2.5e+07	8.010 %	4.6 %	14 %
$1.116^{+0.066}_{-0.084}$	3.506e+08 ± 1.2e+07	5.000 %	5.4 %	13 %
$1.260^{+0.060}_{-0.090}$	1.898e+08 ± 7.600e+06	2.810 %	6.9 %	13 %
$1.415^{+0.065}_{-0.085}$	9.408e+07 ± 4.6e+06	1.000 %	7.5 %	14%
$1.560^{+0.060}_{-0.090}$	4.032e+07 ± 2.6e+06	1.000 %	8.2 %	14 %
$1.720^{+0.070}_{-0.080}$	3.143e+07 ± 2.1e+06	1.000 %	8.7 %	15 %
$1.860^{+0.060}_{-0.090}$	9.987e+06 ± 9.6e+05	1.000 %	9.1 %	14. %
$2.010^{+0.060}_{-0.090}$	7.303e+06 ± 7.2e+05	1.000 %	9.5 %	15 %
$2.175^{+0.075}_{-0.075}$	2.228e+06 ± 4.0e+05	1.000 %	9.8 %	15 %
$2.400^{+0.150}_{-0.150}$	1.122e+06 ± 1.7e+05	1.000 %	10.2 %	15%
$2.700^{+0.150}_{-0.150}$	4.698e+05 ± 1.1e+05	1.000 %	10.8 %	15 %
$3.000^{+0.150}_{-0.150}$	4.996e+04 ± 4.4e+04	1.000 %	11.280 %	15 %

Table A.3: The cross section for $\pi^- + \mathbf{Be} \rightarrow \pi^0 + \mathbf{X}$ **for** $0. \leq Y_{cm} \leq .75$. The first column is the mean p_t in each bin. The second column is the cross section with statistical errors. The third columun is the systematic error in the fit for each bin. The fourth column is the systematic caused by the uncertainty in the energy scale. The last column is the overall systematics added in quadrature including the 10% for the Monte Carlo, 5% for the conversion probabilities, and 1.5% for the normalization transverse fiducial cut correction.

$p_t(GeV)$	XS ($\frac{pb}{(GeV/c)^2}$)	fit syst.	E scale syst.	total syst.
$0.720^{+.18}_{-.12}$	$1.947 \pm .12e{+}9$	15%	7%	20%
$1.020^{+.18}_{-.12}$	$3.450 \pm .31e{+}8$	15%	10%	20%
$1.320^{+.18}_{-.12}$	$9.870 \pm 1.03e{+}7$	5%	10%	15%
$1.650^{+.15}_{-.15}$	$2.909 \pm .406e{+}7$	5%	10%	15%

Table A.4: The cross section for $\pi^- + \mathbf{Cu} \longrightarrow \pi^0 + \mathbf{X}$.

$p_t(GeV)$	α
$0.720^{+.18}_{-.12}$	$.83 \pm .026$
$1.020^{+.18}_{-.12}$	$.87 \pm .039$
$1.320^{+.18}_{-.12}$	$.91 \pm .047$
$1.620^{+.18}_{-.12}$	$.96 \pm .052$

Table A.5: The A dependence parameter α of π^0 production

Bibliography

[1] T. Ferbel, W.R. Molzon, *Rev. Mod. Phys.* 56 (1984), 181.

[2] J.W. Cronin et al., *Phys. Rev.* D11 (1975), 3105.

[3] D. Griffiths, *Introduction to Elementary Particles*, (1987).

[4] A. Bodek et al., *Phys. Rev.* Experimental Studies of the Nuetron and Proton Electromagnetic Structure Funcitons V20 N7 (1979), pp.1471-1539.

[5] L. H. Ryder, *Quantum Field Theory* Cambridge University Press 1985

[6] D. Striley, private communication.

[7] L. Apanasevich, private communication.

[8] W.D. Dlugosz, *The Production of High* p_T π^0 *Mesons in 515 GeV/c* π^- *– Nucleus Collisions*, Ph. D. Dissertation,

[9] S. Blusk, private communication.

[10] E. Engels et al., *Nucl. Instr. Meth.* A279 (1989), 272.

[11] K. Hartman, *Hadronic Production of* π^0 *Pairs and Associated Event Structure*, Ph. D. Dissertation, Pennsylvania State University (1990).

[12] C. Lirakis, *A Study of High Transverse Momentum* η *Production in 530 GeV/c Hadronic Interactions*, Ph. D. Dissertation, Northeastern University (1990).

[13] N. Varelas, π^0 *Production at High Transverse Momenta from* π^- *Collisions at 520 GeV/c on Be and Cu Targets*, Ph.D Dissertation, University of Rochester (1994).

[14] VAXONLINE System, FNAL Computer Department PN-252.

[15] G. Ginther, private communication.

[16] H.J. Klein, J. Zoll, PATCHY Reference Manual, CERN (1983).

[17] R. Brun et al., ZEBRA User's Guide, CERN DD/EE/85-6.

[18] J. P. Mansour ,*High Transverse Momentum* π^0 *Production from* π^- *and p Beams at 530 GeV/c on Be and Cu*, Ph. D. Dissertation, University of Rochester (1989).

[19] M. Zieliński, private communication.

[20] R. Brun et al., GEANT3 User's Guide, CERN DD/EE/84-1.

[21] G. Marchesini et al., HERWIG V5.6, CERN (1993).

[22] F. Paige and Serban D. Protopopescu, A Monte Carlo P-P and $\overline{P}$-P REACTIONS, Brookhaven National Laboratory, Upton N.Y. 11973

[23] H.U. Bengtsson, T. Sjostrand, *Comp. Phys. Comm* 46 (1987),43.

[24] R.M. Roser, *Eta Production at High Transverse Momentum by Negative 520 GeV/c Pions Incident on Beryllium and Copper Targets*, Ph. D. Dissertation, University of Rochester (1994).

[25] W.D. Dlugosz, private communication.

[26] P. R. Bevington, *Data Reduction and Error Analsysis for the Physical Sciences*, pp. 253-254 (1969).

[27] L. Lederman et al., *Phys. Lett.* V46B (1973), 471.

[28] M. Aguilar-Benitez et al., *Z. Phys.* C34 (1987), 419.

[29] C. De Marzo et al., *Phys. Rev.* D36 (1987), 16.

[30] G. Donaldson et al., *Phys. Rev. Lett* 36 (1976), 1110.

[31] G. Ballocchi, *A Measurement of* π^0 *A Low Tranverse Momentum*, Ph. D. Dissertation, University of Rochester (1989).

[32] W.M. Geist et al., *Phys. Rep.* 197 (1990), 263.

[33] G. Alverson et al., *Phys. Rev. Lett.* 68 (1992), 2584.

[34] G. Alverson et al., *Phys. Rev.* D45 (1992), 3899.

[35] G. Alverson et al., *Phys. Rev.* D48 (1993), 5.

[36] G. Alverson et al., *Phys. Rev.* D49 (1993), 3106.

[37] H. Fritzsch et al., *Phys. Lett.* B47 (1973), 365.

[38] R. D. Field, *Applications of Perturbative QCD*, (1989).

[39] Review of Particle Properties, *Phys. Lett.* B239 (1992).

[40] D. Perkins, *Introduction to High Energy Physics* Ch.5, (1987).

[41] D.J. Gross, F. Wilczek, *Phys. Rev. Lett.* 30 (1973), 1343.

[42] H.D. Politzer, *Phys. Rev. Lett.* 30 (1973), 1346.

[43] S. Bethke, J.E. Pilcher, *Ann. Rev Nucl. Part. Sci.* 42 (1992), 251.

[44] A.S. Kronfeld, P.B. Mackenzie, *Ann. Rev. Nucl. Part. Sci.* 43 (1993), 793.

[45] J.F. Owens, *Rev. Mod. Phys.* 59 (1987), 465.

[46] W.K. Tung, J.F. Owens, *Ann. Rev. Nucl. Part. Sci* 42 (1992), 291.

[47] K. Charchula at al., preprint DESY 90-019, (1990).

[48] R. Barlow , *Rep. Prog. Phys.* 56 (1993), N9.

[49] F. Aversa et al., *Nucl. Phys.* B327 (1989), 105.

[50] W. Giele et al., preprint FERMILAB - CONF - 91/243-T (1991).

[51] P. Aurenche et al., *Phys. Lett.* B233 (1989), 517.

[52] P. Aurenche et al., *Phys. Rev.* D39 (1989), 3275.

[53] P. Chiappetta et al., *Nucl. Phys.* B412 (1994), 3.

[54] G. Altarelli, G. Parisi, *Nucl. Phys.* B126 (1977), 298.

[55] H.J. Frisch et al., *Phys. Rev.* D27 (1983), 1001.

[56] L.R. Fortney, *Proceedings DPF Meeting, Vancouver 1991*, 669.

[57] I.V. Ajinenko et al., *Z. Phys.* C35 (1987), 7.

[58] J. Badier et al., *Z. Phys.* C30 (1986), 45.

[59] C. De Marzo et al., *Phys. Rev.* D36 (1987), 16.

[60] M. Bonesini et al., *Z. Phys.* C37 (1987), 39.

[61] I. Kourbanis, *The A Dependence of Leading Particle Production by 800 GeV/c Protons*, Ph. D. Dissertation, Northeastern University (1989).

[62] C. Bromberg et al., *Nucl. Instr. Meth* A307 (1991), 292.

[63] F. Lobkowicz et al., *Nucl. Instr. Meth.* A235 (1985), 332.

[64] W. E. DeSoi, *Construction and Performance of a Liquid Argon Calorimeter for Use in Experiment E-706 at the Fermi National Accelerator Laboratory*, Ph. D. Dissertation, University of Rochester (1990).

[65] R. Benson, *Characteristics of Forward Energy Production in Proton - Nucleus and Pion - Nucleus Collisions at* $\sqrt{s} = 31.5$ *GeV*, Ph. D. Dissertation, University of Minnesota (1990).

[66] IEEE Standard FASTBUS, (1985), ISBN 471-84472-1.

[67] D.D. Skow, *A Study of High Transverse Momentum Eta Meson Production*, Ph. D. Dissertation, University of Rochester (1990).

[68] G. Drake, *Nucl. Instr. Meth.* A269 (1988), 68.

[69] 1990 Research Instrumentation Catalog, LeCroy Corp.

[70] GPM Manual, STR500, Dr. B. Struck.

[71] C. Lirakis, *Proceedings of the First Annual Conference on Electronics for Future Colliders*, LeCroy Corp. (1991), 37.

[72] DSP56000/DSP56001 Digital Signal Processor User's Manual, Motorola.

[73] C. Yosef, *Production of High Transverse Momentum* π^0 *Mesons in Interactions of 530 GeV/c Proton and* π^- *Beams on Beryllium and Copper Targets*, Ph. D. Dissertation, Northeastern University (1990).

[74] L. Sorrell, private communication.

[75] G.O. Alverson, E.L. Pothier, E706 Internal Note 139 (1985).

[76] A. Sinanidis, *Particles Produced in Association with High Transverse Momentum Single Photon and* π^0 *in Hadronic Collisions*, Ph. D. Dissertation, Northeastern University (1989).

[77] G. Osborne, private communication.

[78] A. Carroll et al., *Phys. Lett.* B80 (1979), 319.

[79] J. Ftacnik, private communication.

[80] V. Zutshi, private communication.

[81] P. Chang, private communication.

[82] R.J. Miller, E706 Internal Note (1994).

[83] G. Osborne, E706 Internal Note 197.